Single- and Dual-Polarized Slot and Patch Antennas with Wide Tuning Ranges

by

Carson R. White

A dissertation submitted in partial fulfillment
of the requirements for the degree of
Doctor of Philosophy
(Electrical Engineering)
in The University of Michigan
2008

Doctoral Committee:
  Professor Kamal Sarabandi, Co-Chair
  Professor Gabriel M. Rebeiz, Co-Chair, University of California, San Diego
  Professor Amir Mortazawi
  Professor Kim A. Winick

© Carson R. White

All Rights Reserved

2008

To my family

Acknowledgements

This work was only possible due to the guidance and support of many people. First, I would like to acknowledge my advisor and co-chair of my dissertation committee, Prof. Gabriel Rebeiz. He has taught me many things about antennas, microwaves, research, presentation, and being professional. His high standards have been a blessing, and I have greatly appreciated his hospitality. I would also like to especially acknowledge Prof. Kamal Sarabandi, also a co-chair of my dissertation committee. He has taught me a great deal about electromagnetics (especially through his random scattering course), and it was by his suggestion that the dual-polarized tunable patch antenna was developed. Also, I would like to thank my committee members: Professors Amir Mortazawi, Wayne E. Stark, and Kim A. Winick for their insight, valuable suggestions, and time.

I must acknowledge all of the professors whom I have taken classes from, both at the University of Michigan and the University of Washington: Professors Anthony England, Michael Flynn, Brian Gilchrist, Yasuo Kuga, Mahta Moghaddam, Jamie Phillips, Peter Smereka, Berit Stensones, and many others. Also, research staff members Dr. Adib Nashashibi and Dr. Leland Pierce. The wealth of understanding of electromagnetics in the Radlab is something that I have missed as I have been away.

Working, playing, living, and arguing with my fellow students in the Radlab and at UCSD has been both enriching and enjoyable. Dr. Bernhard Schoenlinner and Dr. Abbas Abbaspour-Tamijani taught me a great deal about antenna measurements and equivalent circuit modelling, respectively, which have been essential to this work. Dr. Sang-June Park has never accepted any assertion that I have made without some sort of proof, forcing me to think deeply about both my work and my worldview. I am grateful to have such a friend and colleague. He is an amazing filter designer, and I have learned a lot about resonators from him. Dr. Karl Brakora has also challenged my thinking in many ways, and has shown me true hospitality. Many others have made my time in graduate school enjoyable: Dr. Denis Mercier, Dr. Christopher Galbraith, Dr. Byung-Wook Min, Michael Chang, Dr. Timothy Hancock, Dr. Kamran Entesari, Dr. Bryan Hung, Dr. Jose Cabanillas, Dr. Jad Rizk, Isak Reines, Tiku Yu, Jason May, Mohammed El-Tanani, Alex Grichener, Asle Festo, Dr. Amelia Buerkle, Wonbin Hong, Jacquelyn Vitaz, Dr. Hakan Bagci, Preston Partridge, Berke Cetinoneri, Yusuf Atesal, Kwang-Jin Koh, Ramadan Alhalabi, Sang-Young Kim, Jennifer Edwards, Hojr Pisheh, Yu-Chin Ou, DongWoo Kang, Mehmet Uzunkol, Dr. Jung-Mu Kim, Dr. Jeong Geun Kim, and many others.

The EECS, Radlab, and UCSD staff have all been very helpful and a pleasure to work with: Karla Johnson, Michelle Chapman, Beth Stalnacker, Richard Carnes, Mary Eyler, Karen Kirchner, Nicoele Watson, Travis Spackman.

The research presented in this dissertation was greatly aided by many companies. I would like to thank Takata, and especially Jim Ebling, for supporting the lens project; Skyworks Inc. and M/A Com both provided varactor diode samples; and the Rogers Corporation provided some of the substrate material. I would especially like to thank Qualcomm for their time and the use of their antenna measurement system.

Before starting graduate school, I was fortunate to be an intern at Boeing Phantom Works. I would like to thank Mark Davis for giving me this opportunity, and Dr. Julio Navarro and the rest of the technical staff for teaching me so much. I learned a great deal about both measurements and real-world systems from this experience.

My parents, Geoff and Nancy White, are amazing. They have been as supportive and loving as I could ever hope for, and I have learned a great deal from their wisdom. My father began teaching me about advanced physics before I knew algebra, and I finally began understanding when I went to college. I would also like to thank my sister, Ramona, and my extended family for their support.

Most of all, I would like to thank God for everything—especially His love and grace.

Carson White
Ann Arbor, MI
May 22, 2008

Table of Contents

List of Tables

List of Figures

Figure

List of Appendices

Appendix

Chapter 1

Introduction

Wireless communication has become ubiquitous over the last half-century, even taken for granted. As the technology has become affordable, more people are taking advantage of it. In fact, it is more common to have access to a mobile telephone than to a land-line in many parts of the world [3]. Wireless communication is the transfer of information through an un-bounded medium (i.e. not through a cable), and physically requires the transfer of energy. The role of the antennas is to radiate into and to collect energy from an un-bounded medium. In order to transmit and receive this energy effectively, the antenna must be impedance matched to the characteristic impedance of the radio transceiver at the frequency of interest, and its polarization must be aligned with the polarization of the waves of interest. There is a constant push toward higher data-rates for communication channels, and although the exact achievable data-rates depend on the modulation scheme, it is generally true for a constant frequency-bandwidth that a larger signal-to-noise ratio at the receiver enables a higher data-rate [4]. Noise is generated inside of the receiver, as well as received by the antenna from external sources, and therefore, it is imperative to maximize the received signal power in order to maximize the data-rate. As is well known, impedance and polarization mismatch both reduce the received power, and therefore, should be minimized.

1.1 Frequency-Tunable Antennas

As technology progresses, there is always a push for smaller devices with more functionality. For wireless devices, this often means that they must communicate with many existing systems using different frequencies. The efficiency and instantaneous bandwidth (BW) of small antennas are limited, however by the following relation [5]:

$$BW_{3dB} \leq \frac{1}{\eta_r} \frac{(kr)^3[1+(kr)^2]}{1+2(kr)^2}, \tag{1.1}$$

where BW_{3dB} is the 3-dB fractional impedance bandwidth, η_r is the radiation efficiency, k is the free-space propagation constant, and r is the radius of the smallest sphere that the antenna will fit inside of. If $kr \ll 1$, (1.1) reduces to

$$BW_{3dB} \leq \frac{(kr)^3}{\eta_r}. \tag{1.2}$$

Bandwidth and efficiency can be traded off, but one cannot, for example, have an antenna that is 0.1 wavelengths long with 50% fractional bandwidth and 100% efficiency. Multi-band antennas, which have two or more resonance frequencies, are a solution if 2 or 3 well-defined frequency-bands are required. For example, many mobile telephones operate at both 800 MHz and 1.8 GHz, and antennas covering these two bands are readily available. If there are too many frequency bands, however, or the frequency bands are not known at the time of manufacture, a frequency-tunable antenna can be a good solution.

A frequency-tunable antenna (hereafter referred to simply as a “tunable antenna”) is a resonant antenna whose resonance frequency is adjusted in the field. In this work, a DC bias voltage is applied to the RF port of the antenna; as the DC voltage is increased, the resonance frequency is increased. Table 1.1 compares the general characteristics of tunable resonant antennas to the characteristics of both wide-band and resonant antennas. Tunable antennas are a good choice for systems that require

Table 1.1: Comparison between tunable-resonant, resonant, and wide-band antennas when the resonant antennas are in their first resonance.

	Wide-band	Resonant	Tunable Resonant
Size	large	small	small
Operating BW	$> 2{:}1$	1–15%	$\leq 2{:}1$
Instantaneous BW	$> 2{:}1$	1–15%	1–10%
Power Handling	high	moderate	low
Control Circuitry	no	no	yes

small efficient antennas that cover a large frequency range (operating BW), but do not require large instantaneous bandwidth or large signal power. For example, an antenna may be required to receive signals with 1-MHz bandwidths from three different transmitters whose center frequencies are 1.1, 1.4, and 1.5 GHz, respectively.

Resonant slot antennas are good candidates for frequency tuning because their resonance frequency can be changed easily using varactors or switches. Peroulis et al. demonstrated a slot antenna that can be switched to four different frequency bands over a 1.7:1 bandwidth using PIN diodes [6]. Behdad et al. demonstrated a single-polarized dual-band slot antenna where both of the bands can be tuned independently over a large tuning range while maintaining a nearly constant radiation pattern [7, 8]. Slot antennas on low dielectric-constant substrates radiate equally to the top and bottom of the ground plane, and therefore, are unsuitable for conformal mounting. Single-polarized microstrip patch antennas have been tuned over frequency ranges of 1.35:1 [1] and 1.6:1 [9, 10], and 1.85:1 [11] (although the impedance match was not presented). With the exception of the patch antenna, there is not a wealth of literature reporting efficient antennas with wide tuning ranges and single-sided radiation. Demonstrating such an antenna was one of the goals of this research. Another goal was to gain a deeper understanding of how tunable antennas can be impedance matched over wide tuning ranges.

1.2 Benefits of Dual-Polarization

The polarization efficiency of a communication system is a function of the alignment of the receive antenna to the incident wave. Specifically, it is calculated as

$$\eta_p = \hat{p_{inc}} \cdot \hat{p_{rec}}, \tag{1.3}$$

where $\hat{p_{inc}}$ and $\hat{p_{rec}}$ are the unit vectors parallel to the incident wave and antenna polarizations, respectively [12]. It is clear that if $\hat{p_{inc}}$ is perpendicular to $\hat{p_{ant}}$, no power is received. Dual-polarized antennas have two orthogonal polarizations, each connected to its own port, and therefore, the two orthogonal components of the incoming wave are received and separated. This property can be exploited to improve the data rate in different ways for line-of-sight and multi-path environments.

1.2.1 Line-of-Sight

In a line-of-sight environment, there is no multipath, and therefore, the polarization is unperturbed. If the transmit and receive antennas are both dual-polarized and perfectly aligned, there are two independent channels over which to send data, doubling the data throughput without increasing the size of the antenna. Furthermore, a radio can communicate simultaneously with two different radios provided they are on orthogonal polarizations. The performance of such systems is limited by the cross-polarized radiation and port-to-port coupling, both of which are often on the order of -20 dB.

1.2.2 Multi-Path Environments

Mobile communication devices are most commonly used in multi-path environments, where waves scatter several times off buildings, vehicles, trees, etc., before reaching the receiver. The scattered waves do not, in general, have the same polarization as the transmitted waves, and therefore, it is very difficult to accurately predict the polarization at the receive antenna. Polarization diversity can be used to increase the received signal power [4]. Multiple Input Multiple Output (MIMO) systems take advantage of multiple uncorrelated channels to increase the data throughput, and are the analog of a phased array in a multipath environment [13]. They do not synthesize a beam like a phased array, but rely on the independence of the propagation channels to send more information. When the transmit and receive antennas are dual polarized, the system is 2-input 2-output. The independence of the channels is determined by the multipath environment and the cross-polarization level of the antennas.

1.3 Tunable Dual-Polarized Antennas

Combining both frequency tuning and dual-polarized operation allows even greater reconfigurability. In fact, such an antenna is a requirement for a true Software Defined Radio, in which the frequency, modulation scheme, and polarization characteristics can be arbitrarily chosen. For example, the radio may at one moment operate at frequency f_1 using horizontal polarization and, at another, operate at f_2 with right-hand circular polarization. This type of radio can replace several non-reconfigurable radios, can be updated by software, and is very attractive for military applications. Cognitive Radios are currently being investigated in which the radios themselves sense the available spectrum and decide on the communications scheme to use [14]. These types of systems require antennas that are both frequency and polarization reconfigurable. True polarization reconfigurability is achieved by feeding both ports of a dual-polarized antenna with the correct magnitude and phase, and therefore, a high level of reconfigurability is achieved when both of the polarizations of a dual-polarized antenna are tuned independently. Perhaps the best candidates for dual-polarized tuning are the slot-ring (also known as the "annular slot") and microstrip patch antennas. Dual-polarized operation [15, 16] and frequency agility [17–20] have been demonstrated, but no dual-polarized antennas were found in a literature for which the resonance frequencies of the orthogonal polarizations are tuned independently over a wide frequency range. Achieving this level of reconfigurability was a major goal of this work.

1.4 Thesis Overview

There is a need for both highly tunable conformal antennas and dual-polarized antennas with independent tuning over a wide range, but there is not a wealth of literature reporting antennas with these properties. The goal of this research was to demonstrate and gain understand of operation of single- and dual-polarized antennas with wide tuning ranges.

The slot-ring antenna was chosen to demonstrate independent tuning of the dual-polarized antenna. The tuning of a single mode is studied in detail in Chapter 2. The theory of the tuning of a single mode is presented, and tuning of the slot-ring antenna is demonstrated from 2 to 5 GHz using fixed capacitors [21]. A second design is tuned from 0.95 to 1.8 GHz using varactor diodes; impedance matching is discussed, and measured results including power handling are presented. The dual-polarized slot-ring antenna is studied in Chapter 3. First, the independent tuning of the modes is discussed using symmetry and the transverse resonance method; next, independent tuning of a preliminary design is demonstrated from 1.92 to 4.4 GHz using fixed capacitors [22]; also, a second design of the dual-polarized slot-ring antenna is presented with independent tuning from 0.93 to 1.6 GHz and better than 20 dB port-to-port isolation over most of the tuning range.

Many antennas must be conformally mounted in practice, and therefore, the insight gained in developing and analyzing the tunable slot-ring antennas was applied to a shallow cavity-backed slot antenna. In Chapter 4, methods to achieve single-sided radiation are discussed, analysis of the cavity backed slot is reviewed, and a shallow cavity-backed slot antenna that is compatible with printed circuit board fabrication techniques is tuned from 1.0 to 1.9 GHz using a single varactor diode. Small antennas are usually desirable for mobile communications. With this in mind, the tuning of miniaturized cavity-backed slot antennas is briefly studied; the calculation of the bandwidth and efficiency of small varactor tuned antennas is outlined, and the performance over tuning of three different miniaturized cavity-backed slot antennas is compared.

The knowledge gained in developing the tunable dual-polarized slot-ring and cavity-backed slot antennas is then applied to the cavity-backed patch antenna—which is nearly identical to the microstrip patch antenna from an impedance and radiation pattern perspective—in Chapter 5. Differential feeds are employed to achieve >25 dB cross-polarization and port-to-port isolation over the 0.6–1 GHz frequency range. The differential-mode transmission-line model is used to quickly determine the location of the feeds and the matching network. Next, the design is described, and measured results are presented. The measured results of a 0.5:1 scale model (which tunes from 1.2–2.1 GHz) are also presented, and can be directly compared with the results of the other antennas in this frequency range.

Finally, in Chapter 6, the important points of this work are summarized and possible future work on the topic is discussed. Appendix A presents a printed planar lens at 24 GHz that scans to ±60° in both the E- and H-planes. It was an important part of my research, but is not directly related to tunable slot antennas. Appendix B reiterates the calculation of key parameters for the microstrip patch antenna transmission line model, and Appendix C presents the method that was used in this work to calculate the S-parameters of the loaded antenna based on a full-wave simulations in which ports were inserted in place of lumped elements.

Chapter 2

The Single-Polarized Tunable Slot-Ring Antenna

The slot-ring antenna is a resonant slot loop cut in a conducting plane, and in free-space, is the dual of a resonant wire loop. The shape of the loop considered in this work is square, but the circular slot-ring antenna (also known as the "Annular Slot Antenna") is also common. Slot-ring antennas that are tunable or reconfigurable over a small frequency range have been presented using either capacitive loading [17],[18, 19] or reconfigurable matching networks [20]. However, no slot-ring antenna with tunability approaching an octave was found in the literature.

The first section of this chapter presents methods to analyze the resonance frequencies and voltage distributions of both the unloaded and loaded slot-ring antennas. After understanding of the antenna is gained, two single-polarized tunable slot-ring antennas with wide tuning ranges are presented.

2.1 Slot-Ring Antenna Analysis

2.1.1 The Unloaded Slot-Ring Antenna

If the slot width, w, is much smaller than the wavelength, λ, the slot can be considered as a slot-line transmission line. The characteristic impedance, Z_s, propagation constant, β, and transverse electric field distribution, e_s, can be calculated by methods described in [23]. Using the transmission-line assumption, the voltage

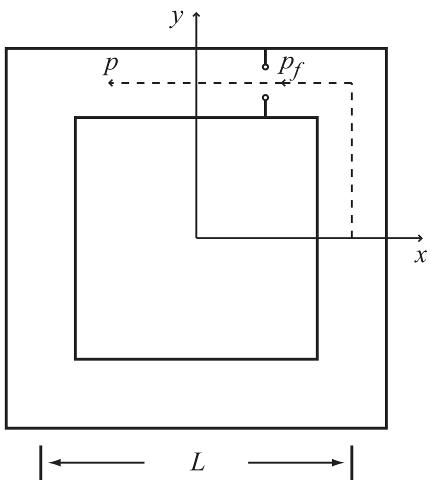

Figure 2.1: Square slot-ring antenna geometry.

distribution, V_s, on the slot is found by solving the wave equation,

$$\frac{d^2V_s}{dp} + \beta^2 V_s = 0, \tag{2.1}$$

with periodic boundary conditions ($V_s(p+4L) = V_s(p)$), where p is the path distance along the slot and L is the length of one side of the loop (Fig. 2.1). There are two orthogonal solutions for the case where $\beta > 0$,

$$\begin{aligned} \psi_x &= \frac{2}{4L} cos(\beta p) \\ \psi_y &= \frac{2}{4L} sin(\beta p), \end{aligned} \tag{2.2}$$

that exist when

$$\beta = \beta_n = \frac{2\pi(n+1)}{4L}, \qquad n = 0, 1, 2, \ldots \tag{2.3}$$

The fundamental resonance occurs at the frequency, f_0, where the circumference of the ring is one guided wavelength.

The voltage across the slot is a linear combination of the two modes:

$$V_s = a_x\psi_x + a_y\psi_y, \tag{2.4}$$

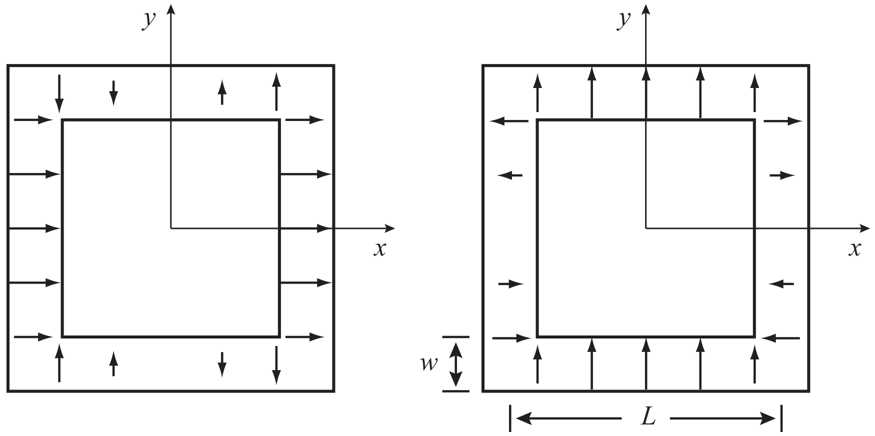

Figure 2.2: Electric field distributions of the two orthogonal voltage modes, $\mathbf{\Psi_x}$ (left) and $\mathbf{\Psi_y}$ (right) assuming $w \ll \lambda$. The voltage is defined from the inside to the outside of the slot-ring.

where the complex magnitudes a_x and a_y depend on the excitation. Let

$$\begin{aligned} \Psi_x = \psi_x(\beta = \beta_0) = \frac{2}{4L} cos(\frac{2\pi}{4L}p) \\ \Psi_y = \psi_y(\beta = \beta_0) = \frac{2}{4L} sin(\frac{2\pi}{4L}p) \end{aligned} \tag{2.5}$$

be the modes at fundamental resonance. Inspection of the field distributions of each mode (Fig. 2.2) reveals that the radiation patterns of Ψ_x and Ψ_y are $\hat{x}$- and $\hat{y}$-polarized, respectively.

Assuming a delta-gap source at the point p_f ($V_f(p) = V_0\delta(p_f)$), a_x and a_y can be found:

$$a_x =< V_f, \Psi_x >= V_0 \frac{2}{4L} cos(\frac{2\pi}{4L}p_f) \tag{2.6a}$$

$$a_y =< V_f, \Psi_y >= V_0 \frac{2}{4L} sin(\frac{2\pi}{4L}p_f), \tag{2.6b}$$

where

$$< f_1(p), f_2(p) >= \int_0^{4L} f_1(p) f_2^*(p) dp \tag{2.7}$$

is the inner product of the functions f_1 and f_2. It is clear—both from (2.6) and the

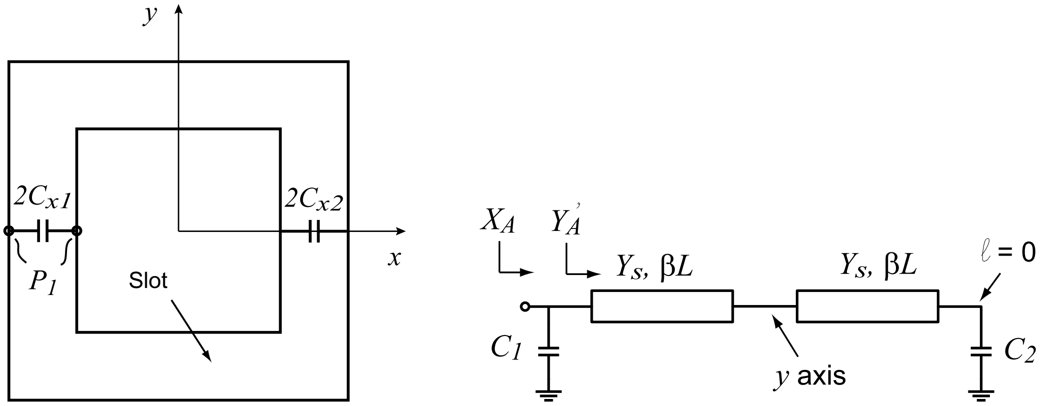

(a) (b)

Figure 2.3: (a) Slot-ring antenna with loading capacitors along the x-axis. (b) The even-mode equivalent circuit.

locations of the short-circuit points of Ψ_x and Ψ_y—that if the antenna is fed by a voltage source on the x axis, only Ψ_x is excited, and likewise, if the feed is on the y axis, only Ψ_y is excited.

2.1.2 The Capacitively-Loaded Slot-Ring Antenna

In the previous section, the resonance frequency and voltage distribution of the unloaded slot-ring antenna were analyzed by solving for the eigenmodes. Although the loaded slot-ring antenna can also be analyzed in this way, it is valuable to know the input reactance both above and below resonance. This can be solved using even-mode analysis if the feed point is in one of the symmetry planes of the antenna.

Consider the slot-ring antenna with shunt capacitances, C_{x1} and C_{x2}, and the feed point placed along the x axis (Fig. 2.3(a)). The even-mode equivalent circuit is shown in Fig 2.3(b). The voltage and current on the transmission line are expressed as the sum of forward and backward waves:

$$i(\ell) = I_0^+(e^{-j\beta\ell} - \Gamma e^{j\beta\ell}) \tag{2.8a}$$

$$v(\ell) = \frac{I_0^+}{Y_s}(e^{-j\beta\ell} + \Gamma e^{j\beta\ell}), \tag{2.8b}$$

where $\ell = -p$,

$$\Gamma = \frac{Y_s - Y_2}{Y_s + Y_2} \tag{2.9}$$

is the reflection coefficient at C_2, $Y_2 = j\omega C_2$, and Y_s is the characteristic admittance of the transmission line. Y_2 is imaginary, and therefore, $|\Gamma| = 1$. Γ can be expressed as:

$$\Gamma = e^{j2\phi}, \qquad 2\phi = \tan^{-1}\frac{-2\omega C_2 Y_s}{Y_s^2 - (\omega C_2)^2}. \tag{2.10}$$

The voltage distribution and input admittance can now be written in terms of the reflection phase ϕ:

$$v(\ell) = 2\frac{I_0^+}{Y_s}e^{j\phi}\cos(\beta\ell + \phi), \tag{2.11}$$

$$Y_A' = \frac{i(-2L)}{v(-2L)} = jY_s\tan(2\beta L - \phi). \tag{2.12}$$

Finally, the input admittance, Y_A, is calculated:

$$Y_A = Y_A' + j\omega C_1. \tag{2.13}$$

The fundamental resonance occurs at the the lowest frequency at which $\Im[Y_A] = 0$. This occurs when $\pi/2 < 2\beta L - \phi \leq \pi$, and because $\phi \leq 0$, $2\beta L \leq \pi$. In other words, the fundamental resonance of the capacitively loaded slot-ring antenna occurs when the circumference is $<\lambda$.

2.2 A Fixed-Capacitor-Loaded Antenna from 2–5 GHz

The antenna design and results presented in this section were previously presented in [21].

2.2.1 Design and Fabrication

The slot-ring antenna geometry is shown in Fig. 2.4(a). It is square in shape with an inner circumference of 40 mm, a slot width of 3 mm, and is fed by an open-circuited microstrip line. The antenna was designed to be $\hat{x}$-polarized, to have a two-sided broadside radiation pattern, to operate in the fundamental resonance, and to tune from 5 GHz to less than 2 GHz. Due to the nature of the microstrip to slot-ring antenna transition, it is important to maintain symmetry about the x-z plane in order to maintain the desired polarization and radiation pattern [23]. Tuning is achieved by capacitively loading the antenna along the x-axis, preserving the symmetry. The antenna was loaded with surface mount chip capacitors (AVX ACCU-P), but varactor diodes are used in the next design.

The final geometry was determined by tuning the original geometry with a planar full-wave solver [24] until the antenna was matched to 75 Ω over the desired frequency tuning range. The original circumference (referenced to the center of the slot) was chosen to be one free-space wavelength and the original microstrip stub length was chosen to be a quarter-wave at 5 GHz. The slot-width was chosen to be 3 mm because it is relatively wide (increasing the bandwidth), but has not been optimized. The antenna was printed on a 0.787 mm thick copper-clad Taconic TLY5 substrate ($\epsilon_r = 2.2$). Although it was designed assuming an infinite substrate, the antenna was printed on a 60 x 60 mm^2 substrate using standard photolithographic techniques.

The microstrip feed structure is shown in detail in Fig. 2.4(b). The microstrip

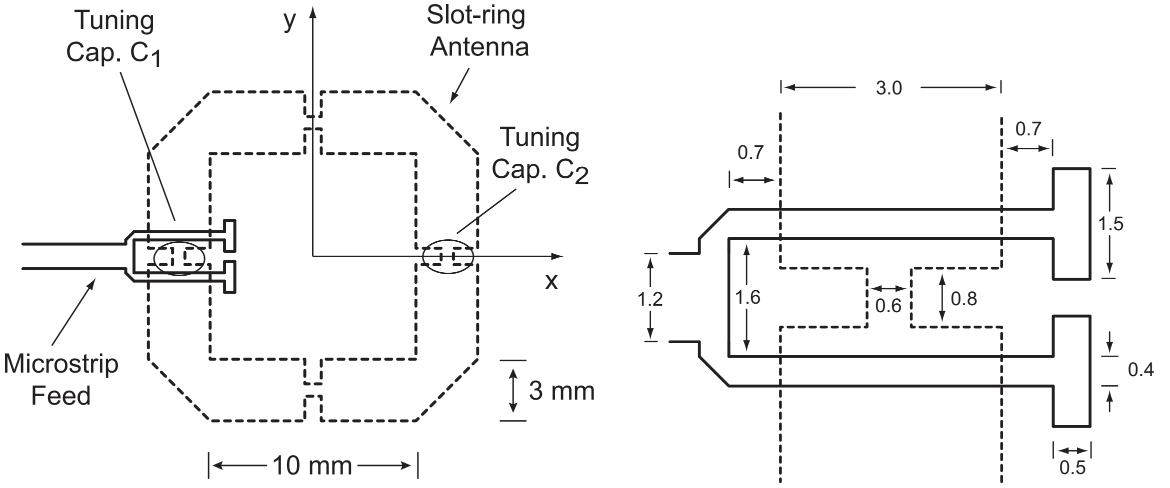

(a) (b)

Figure 2.4: (a) Single-polarized slotring antenna geometry with loading capacitors. (b) Geometry of the microstrip feed. All dimensions are in millimeters.

line would normally cross the slot along the x-axis, but this is directly under one of the loading capacitors. The exact effect of the capacitor on the coupling fields could not be simulated, so the microstrip line was split and crosses on either side of the capacitor. Splitting the microstrip line this way maintains the symmetry about the x-z plane and keeps the majority of the coupling away from the capacitor. The characteristic impedance, Z_0, of the 1.2-mm-wide input microstrip line is 76 Ω, and the 0.4-mm-wide microstrip line has a characteristic impedance of 123 Ω, according to IE3D [24].

Several identical copies of the antenna were fabricated on the same board and then loaded with different capacitance values. End-launch PCB-mount SMA to microstrip transitions were soldered to each antenna at the edge of the substrate. Before mounting the loading capacitors, the capacitance of each capacitor was measured at 30 MHz, and the unloaded frequency response of each antenna was verified.

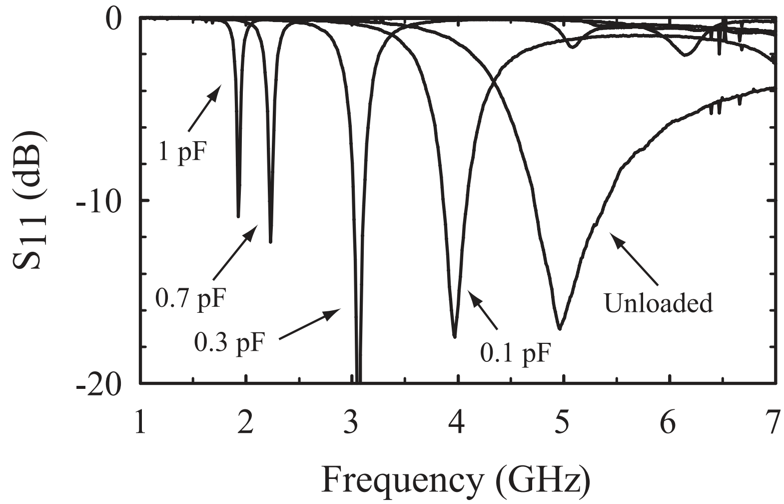

Figure 2.5: Measured return loss with various loading capacitances from 0 to 1 pF ($Z_0 = 76\ \Omega$).

2.2.2 Results and Discussion

The impedance of each antenna was measured with a vector network analyzer (Agilent E5071B). The network analyzer was calibrated by the TRL method to the 76 Ω microstrip line, and the calibration plane was 14 mm from the microstrip split. Fig. 2.5 shows the measured return loss of the antennas with different loading capacitors. It can be seen that the resonant frequency, f_0, varies from 4.96 GHz (unloaded) to 1.93 GHz ($C_1 = C_2 = 1.0$ pF) with better than 10 dB return loss. The -10 dB bandwidth, $B_{10\mathrm{dB}}$, decreases considerably from the unloaded case to the 1 pF case. There are three reasons for this. First, the antenna becomes smaller electrically, second, the return loss was only -11 dB at 1.93 GHz, and finally, the electric field distribution in the slot changes and does not radiate as efficiently. Table 2.1 summarizes f_0 and $B_{10\mathrm{dB}}$ for the different loading capacitance values.

The radiation pattern of each antenna was measured in a Satimo Stargate 32 antenna measurement system courtesy of Qualcomm. The E-plane, H-plane, and 45^{o}-cut patterns are plotted in Fig. 2.6. A bazooka balun was used at 1.93 and

Table 2.1: Measured antenna parameters for different loading capacitances.

C_1 (pF)	C_2 (pF)	f_o (GHz)	$B_{10\text{dB}}$ (%)	Gain (dB)	Efficiency (dB)
0	0	4.96	13.4	4.2	-0.86
0.122	0.122	3.98	5.6	5.4	-0.15
0.316	0.317	3.07	3.1	4.4	-0.44
0.730	0.733	2.23	1.1	2.9	-1.4
1.01	1.01	1.93	-	2.1	-2.4

2.25 GHz to prevent the feed cable from radiating, but baluns were not available at higher frequencies. The measurement cable was coated with an absorbing material to reduce its scattering. The radiation patterns have maxima in the broadside and backside directions and change only slightly as the antenna is loaded. The ripple in the E-plane pattern in Fig. 2.6(a) is most likely caused coupling to the measurement cable, which was in the E-plane. This coupling is most likely higher at 5 GHz than 4 GHz because the substrate is one wavelength long (and therefore resonant) at 5 GHz. The maximum gain is 5.4 dB at 4 GHz and the minimum is 2.1 dB at 1.93 GHz. The antenna gain and efficiency for all variations are given in Table 2.1. The efficiency is highest at 4 GHz, and declines monotonically with stronger loading, as expected. The reduced efficiency at 5 GHz is most likely due coupling to a substrate resonance, which exacerbated the coupling to the measurement cable. This coupling is investigated further in the next section.

2.3 A Varactor-Tuned Antenna from 0.95–1.8 GHz

2.3.1 Design

The single-polarized slot-ring antenna geometry is shown in Fig. 2.7 with a width, w, of 3 mm. The antenna is capacitively loaded along the x-axis with varactor diodes (M/A-Com MA46H071-1056, 2.5 - 0.45 pF from 0 - 20 V) [25], and there are also varactor-mounting pads along the y-axis so that the same slot-ring resonator can be

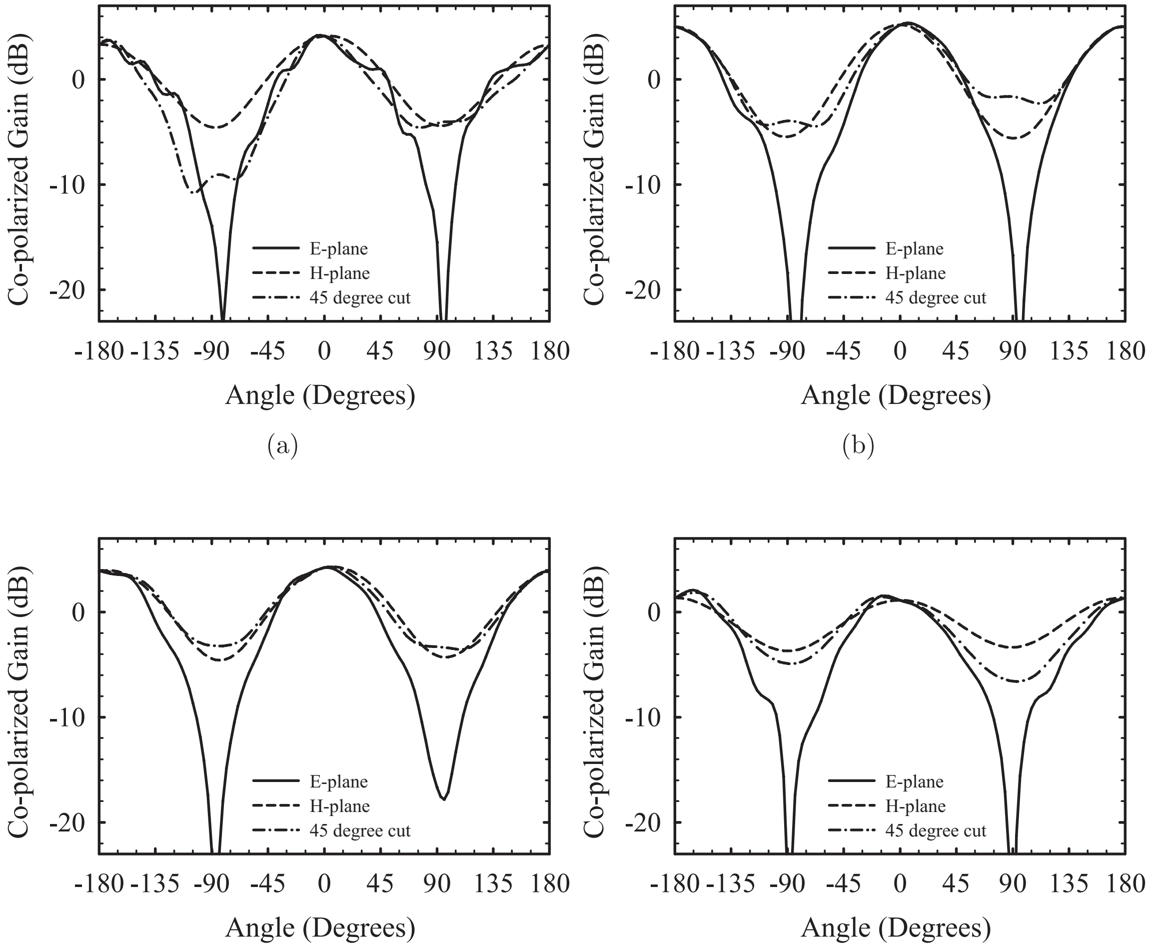

(a) (b) (c) (d)

Figure 2.6: Measured radiation patterns at (a) 4.995 GHz, (b) 4 GHz, (c) 3.1 GHz, and (d) 1.93 GHz.

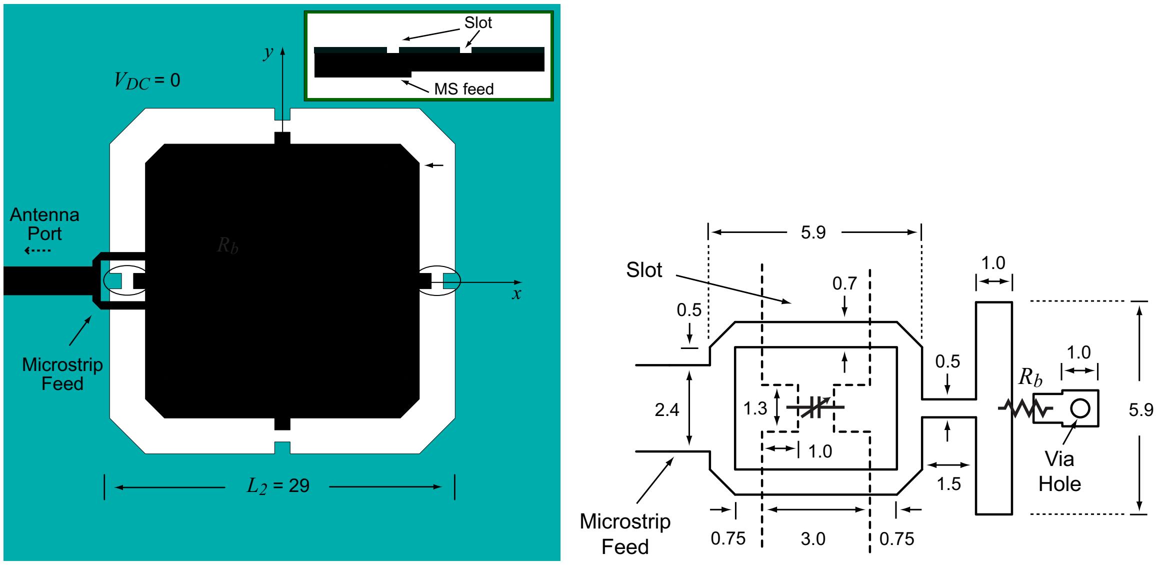

(a) (b)

Figure 2.7: Layout of (a) the slot-ring antenna and (b) the microstrip to slot antenna transition and biasing scheme. All dimensions are in millimeters.

used for both the single- and dual-polarized antennas. The antenna is printed on a 70 x 70 x 0.787 mm^3 Taconic TLY-5 substrate ($\epsilon_r = 2.2$, $\tan\delta = 0.0009$ at 10 GHz).

The tuning characteristics of the antenna were investigated by simulating the slot-ring antenna with gap ports along the x-axis with IE3D [24] (Fig. 2.8(a)). The input impedance of the capacitively-loaded antenna, Z_A, was calculated as shown in Fig. 2.8(b). The real part of Z_A, R_A, is plotted in Fig. 2.9 for tuning capacitances

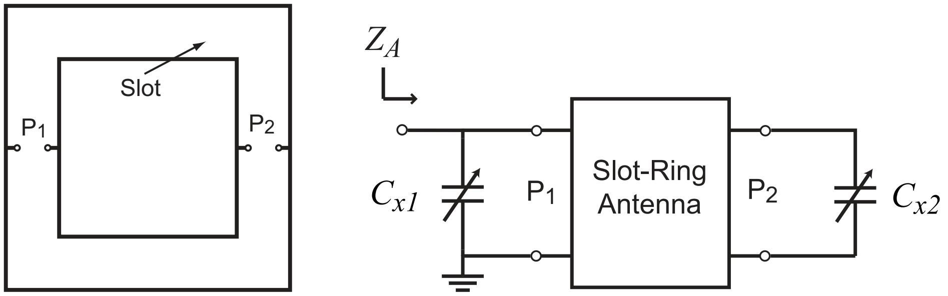

(a) (b)

Figure 2.8: (a) Slot-ring antenna with gap ports along the x-axis. (b) Calculation of the loaded antenna impedance, Z_A.

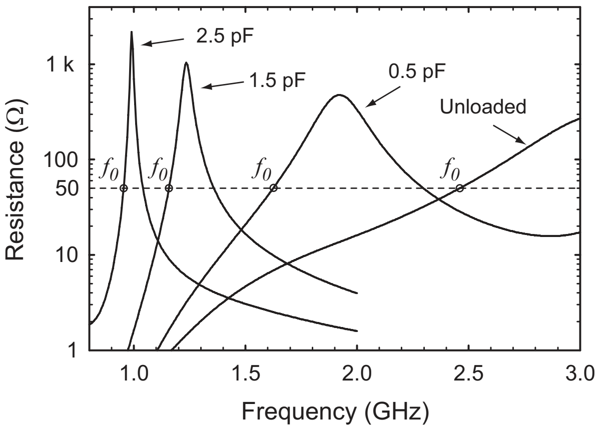

Figure 2.9: R_A for different loading capacitance values ($C_{x1} = C_{x2} = C_x$).

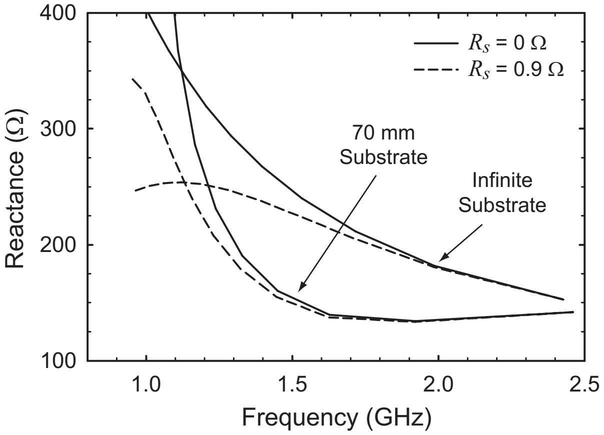

Figure 2.10: $X_A(f_0)$ when $R_A = 50\ \Omega$. The loading capacitance, $C_{x1} = C_{x2}$, is changing from 0 to 2.5 pF.

$C_{x1} = C_{x2} = C_x$ from 0 to 2.5 pF assuming an infinite ground plane and ideal capacitors. The resonant input resistance increases from 300 Ω in the unloaded state to more than 3 kΩ when loaded with 2.5 pF, and therefore, it is difficult to match the antenna at resonance over a large tuning range. However, the slot-ring antenna can be matched directly to the characteristic impedance, Z_0, at a frequency, f_0, that is below resonance by placing a reactive element in series with the antenna. If the point f_0 on each resistance curve is chosen such that $R_A = Z_0$, the antenna reactance at f_0, $X_A(f_0)$, must then be cancelled.

Both the substrate size and the varactor series resistance, R_s, affect the impedance matching. $X_A(f_0)$ for $Z_0 = 50\ \Omega$ is compared in Fig. 2.10 for the following cases: infinite substrate and $R_s = 0$, infinite substrate and $R_s = 0.9\ \Omega$, finite substrate and $R_s = 0$, and finite substrate and $R_s = 0.9\ \Omega$. In the case of an infinite substrate and $R_s = 0$, $X_A(f_0)$ varies as approximately $1/f_0$, which can be cancelled with a series capacitor. However, the non-idealities of the varactor change the shape of $X_A(f_0)$. At low frequencies, the quality factor, Q, of the antenna becomes comparable to the Q of the varactors, and the required reactance to match the antenna decreases. Whereas R_s affects $X_A(f_0)$ at the low frequencies, the finite substrate has an effect over the whole frequency range; it has standing wave currents that increase the effective size of the antenna, reducing the Q. In this case, the required reactance is nearly constant at the high end of the tuning range, but rises sharply at lower frequencies. The effects of both the finite substrate and R_s on $X_A(f_0)$ cancel out sufficiently for the antenna to be matched to better than -13 dB over the tuning range.

It is convenient to feed the slot-ring antenna with a microstrip line, and the analysis of the microstrip to slot antenna transition can be found in [23]. The microstrip feed structure is shown in detail in Fig. 2.7(b), and the equivalent circuit of the antenna and transition is shown in Fig. 2.11. The slot-ring antenna is coupled in series with the microstrip line through a transformer, and therefore,

$$Z_{in} = \frac{Z_A}{n^2} + jX_m, \tag{2.14}$$

where $X_m = -1/\omega C_m$, C_m is the shunt capacitance of everything on the right hand side of the slot—two 83-Ω open-circuited stubs and the 50 fF parasitic capacitance of the bias resistor, n is slightly less than 1, and $R_b = 100$ kΩ is high enough to be neglected. The microstrip line would logically cross the slot along the x-axis, but this is directly under one of the loading varactors. The effect of the varactor's package on

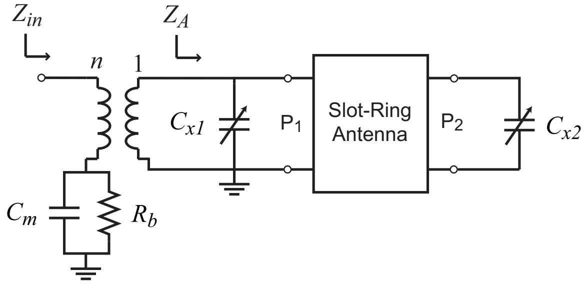

Figure 2.11: Equivalent circuit of the single-polarized tunable slot-ring antenna.

the microstrip to slot fields is not known, so the 50 Ω microstrip line is split into two 100 Ω lines and crosses on either side of the varactor. This maintains the symmetry about the x-z plane and keeps the majority of the coupling away from the varactor.

The varactor diode biasing is achieved by placing a voltage, V_b, on the center of the slot-ring antenna. V_b is externally applied to the RF line with a bias tee, and is connected to the center of the slot-ring through a 100 kΩ resistor and a via hole (Fig. 2.7).

2.3.2 Results and Discussion

Impedance

The antenna input impedance was measured at different bias states with an Agilent E5071B vector network analyzer at -20 dBm source power. Ferrite beads [26] were placed on the measurement cable at the antenna port to suppress the coupling to the cable shield, and the antenna was placed on a foam block about 1 m from any scatterers. The center frequency varied from 0.95 GHz to 1.8 GHz as V_b varied from 0 to 20 V with <-13 dB return loss.

Before the varactor diodes were installed on the antenna, their equivalent series capacitance and resistance were measured versus both frequency and bias voltage using an Agilent E4991A impedance analyzer. The return loss was then simulated

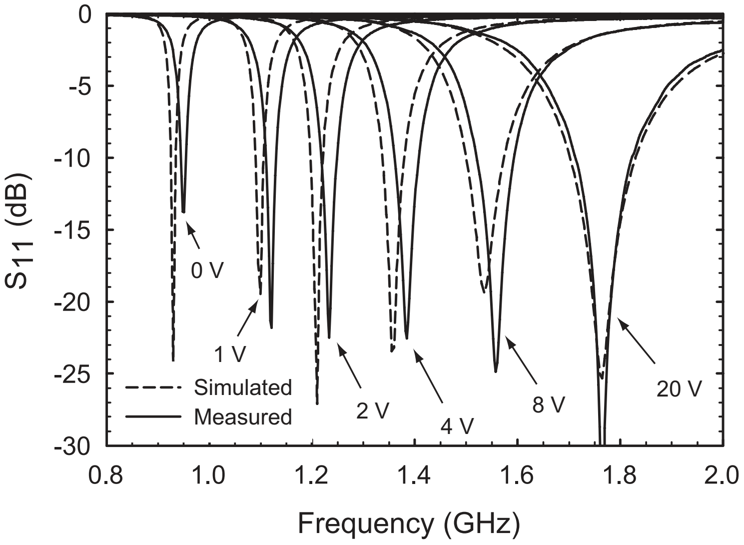

Figure 2.12: Measured and simulated return loss of the single-polarized antenna. The reference plane is the antenna port.

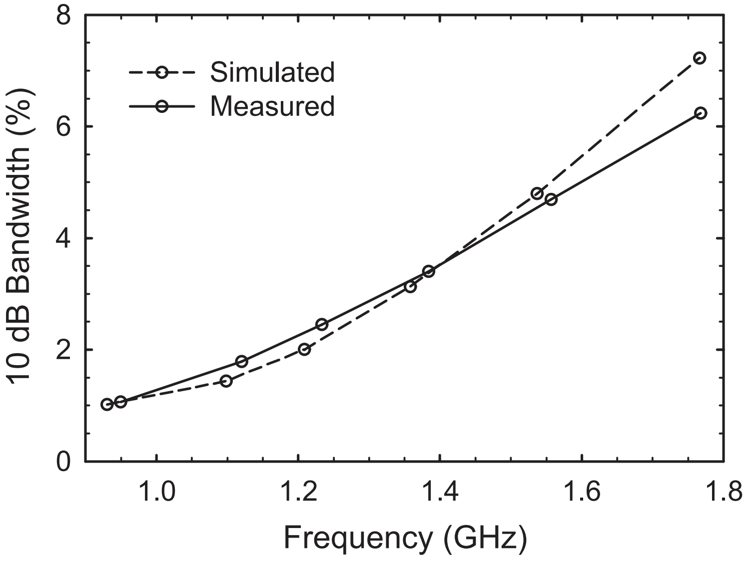

Figure 2.13: Measured and simulated instantaneous 10 dB bandwidth.

using the measured varactor impedance, and is compared to the measured return loss in Fig. 2.12. The measured center frequency is slightly higher for every bias state except 20 V. This difference is most likely due to coupling to the feed cable because the effect of the cable was not simulated. It will be seen from the radiation patterns that, although ferrite beads were used, the coupling to the cable was significant.

The instantaneous 10 dB bandwidth, B_{10dB}, is plotted in Fig. 2.13 as a function of f_0, and is 6% at 1.8 GHz and 1% at 0.95 GHz. Although the antenna (including the substrate) is not electrically small [5], the decrease in bandwidth can be explained as follows. The antenna is operating in a parallel resonance mode, and the radiation conductance decreases as the capacitive loading increases (Fig. 2.9). The quality factor, Q_p, of a parallel resonator is

$$Q_p = \frac{1}{B_{3dB}} = \sqrt{\frac{C}{L}}\frac{1}{G}, \tag{2.15}$$

where C, L, and G are the equivalent capacitance, inductance, and conductance. B_{3dB} decreases as the antenna is loaded with higher capacitance because C increases and G decreases at the same time.

Radiation Patterns and Efficiency

The radiation patterns of the antenna were measured in a Satimo Stargate 32 [27] spherical near-field chamber, and the measured and simulated gain and efficiency are plotted in Fig. 2.14. The measurement cable was coated with absorbing material to reduce scattering, and ferrite beads were placed near the antenna port to reduce the coupling to the cable shield. The measured efficiency is lower than simulated for all frequencies, and the difference is greatest at the low frequencies.

The difference in gain is most likely caused by coupling to the shield of the measurement cable, which was not included in the simulation. The substrate is smaller

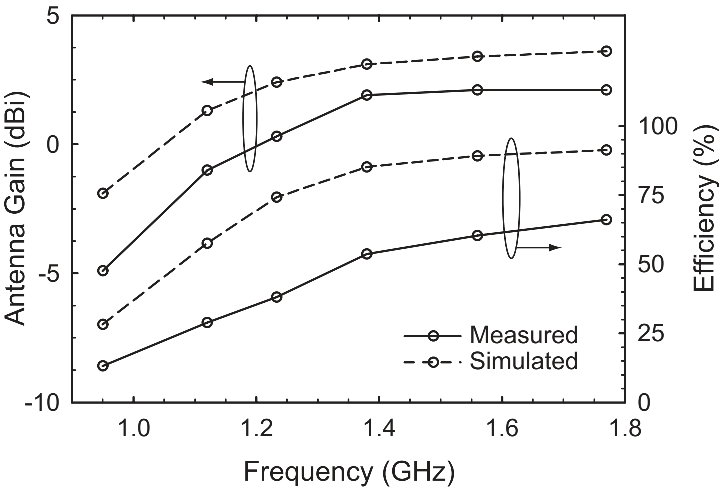

Figure 2.14: Measured and simulated antenna gain and efficiency of the single-polarized antenna.

than $\lambda/2$ at all frequencies, and therefore, the standing-wave current on the finite ground plane is significant. Ferrite beads reduce the coupling from the antenna to the cable shield by presenting a high impedance to the current that would otherwise flow on the cable shield, but the place where the cable is connected is an open-circuit point of the slot-ring–finite-substrate resonator (as can be seen by symmetry), and therefore, current still flows and the efficiency suffers. Some of the lost power is dissipated in the ferrite beads and the resistive coating on the cable, and the rest radiates from the cable—causing ripple in the radiation pattern. The beads used in these measurements have an impedance peak at 2.45 GHz, which is consistent with the fact that the difference between the measured and simulated efficiencies is smaller at the higher frequencies. In future designs, the cable should be attached along the y-axis, which is a short-circuit point of the slot-ring–finite-substrate resonator and is normal to the $\hat{x}$-polarized radiation, and therefore, will result in less coupling to the cable shield.

The radiation patterns are similar for all tuning states, and the measured and simulated patterns at 0.95 and 1.8 GHz are shown in Fig. 2.15. The H-plane pattern

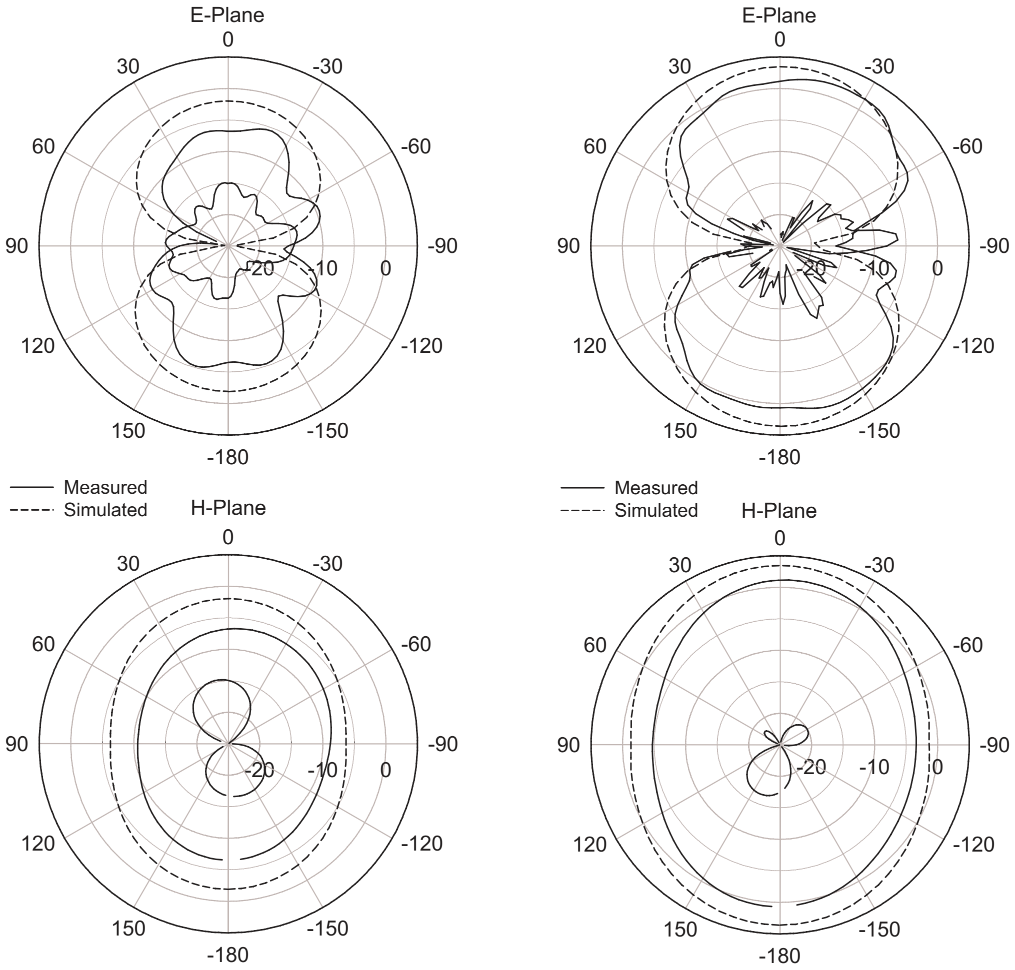

(a)

(b)

Figure 2.15: Antenna gain patterns in the principle planes at (a) f_0 =0.95 GHz (V_b = 0 V) and (b) f_0 = 1.8 GHz (V_b = 20 V).

is nearly constant, and as expected for a slot antenna in a small finite ground plane, there are nulls in the E-plane in the plane of the antenna. The simulated cross-polarization is zero in the E-plane (due to symmetry), and better than -25 dB in the H-plane at all bias states, but the the measured cross-polarization was as high as -8 dB in the E-plane. The high cross-polarization level, as well as the ripple in the E-plane pattern, is most likely due to radiation and scattering from the measurement cable.

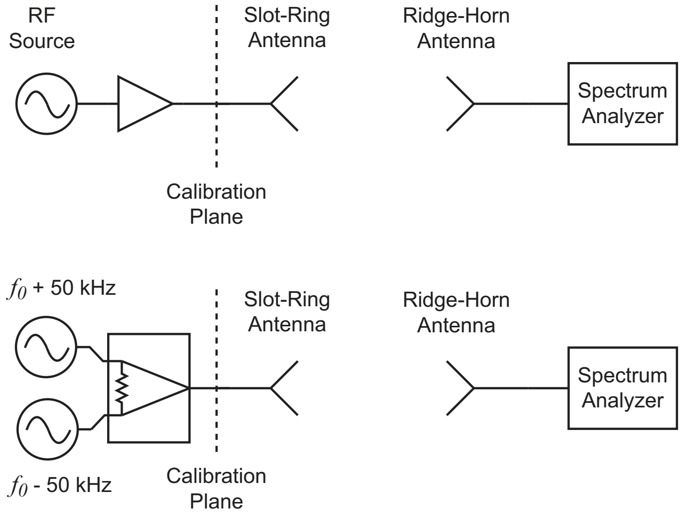

Figure 2.16: Measurement setup for P_{1dB} (top) and IIP3 (bottom).

Nonlinearities

The varactor-tuned slot-ring antenna is non-linear because the junction capacitance, C_j, of the varactor diodes depends on the voltage, V, across it:

$$C_j = C_{J0} \left(\frac{V_{bi}}{V_{bi} + V} \right)^{\Gamma}, \tag{2.16}$$

where C_{J0} is the zero bias junction capacitance, V_{bi} is the built-in potential, and Γ is the power law exponent of the junction capacitance. The non-linearities are most severe at the lower frequencies for two reasons: first, the C-V curve is steeper at lower bias voltages (lower resonance frequencies), and second, the voltage swing across the diodes is larger at the lower resonance frequencies for the same power level (higher $X_A(f_0)$).

The 1-dB compression point, P_{1dB}, and the input third-order intercept point, IIP3, were measured in the transmit mode (Fig. 2.16), and the results are shown in Fig. 2.17. P_{1dB} was measured by feeding the slot-ring antenna with a continuous-wave (CW) source and measuring the signal at one angle with a ridge-horn antenna and a spectrum analyzer (Agilent E4407B). The IIP3 was measured by combining two CW

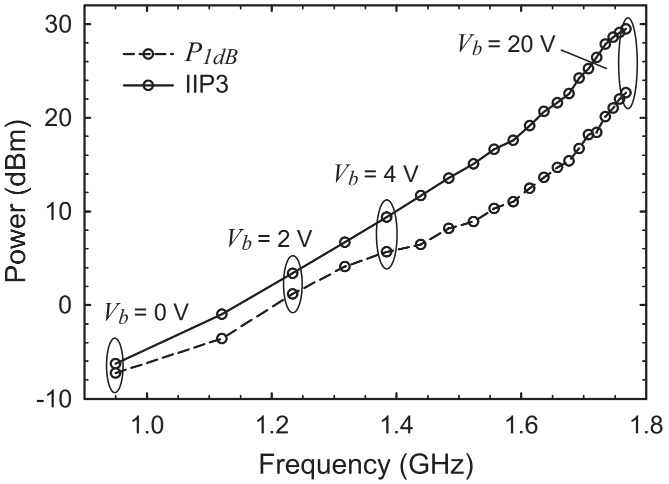

Figure 2.17: Measured input P_{1dB} and IIP3 in the transmit mode.

sources at 100 kHz offset with a power combiner and measuring the radiated signal at one angle with a ridge-horn and a spectrum analyzer. It is assumed that the antenna pattern does not change at power levels in and near the linear region and over a 300 kHz bandwidth.

A considerable contribution to the gain compression of the slot-ring antenna at f_0 is reflection loss due to a shift in the resonance frequency. This can be seen in the measured return loss at 2 V bias with different power levels (Fig. 2.18). The same effect is observed for 0 and 1 V bias. The return loss at P_{1dB} could not be measured for higher bias voltages because the power levels were too high for the network analyzer. The resonance frequency decreases with increased power because as the voltage swing across the diodes increases, the effective capacitance increases. This suggests that P_{1dB} can be improved by dynamically increasing the bias voltage as the power level is increased.

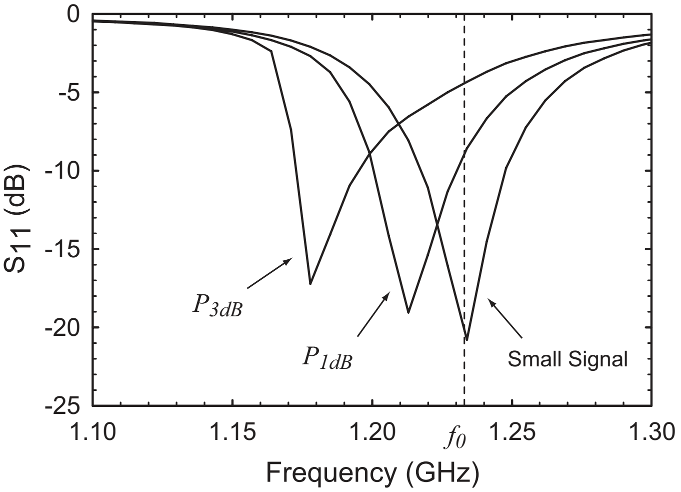

Figure 2.18: Measured return loss when $V_b = 2$ V at three power levels: the small signal region (-20 dBm) and the 1 and 3 dB compression points (1.2 and 5.4 dBm, respectively).

Chapter 3

The Dual-Polarized Tunable Slot-Ring Antenna

Perhaps the most attractive feature of the slot-ring antenna is its dual-polarization capability [15]. Dual-polarized antennas enable polarization diversity, polarization agility, and both polarizations can be used as independent antennas in a MIMO system. Furthermore, it is possible to synthesize tunable circularly-polarized antennas if both polarizations are tuned simultaneously. The requirements for independent tuning of the polarizations of the dual-polarized slot-ring antenna are described, followed by a demonstration of the independent tuning capability using fixed-capacitor loading, and finally, a varactor-tuned dual-polarized slot-ring antenna is presented.

3.1 Capacitively Loaded Slot-Ring Modes

If the slot width, w, is much smaller than the wavelength, λ, the slot can be considered as a slot-line transmission line. The characteristic impedance, Z_s, propagation constant, β, and transverse electric field distribution, e_s, can be calculated by methods described in [23]. The fundamental resonance of the unloaded slot-ring resonator occurs when the circumference of the ring is one guided wavelength. At this frequency, there are two orthogonal voltage modes, Ψ_x and Ψ_y, whose radiation patterns are $\hat{x}$- and $\hat{y}$-polarized, respectively (Fig. 3.1). If the antenna is capacitively loaded, the fundamental resonance occurs at a lower frequency. The eigenmodes can be approximated using the transverse resonance method [8].

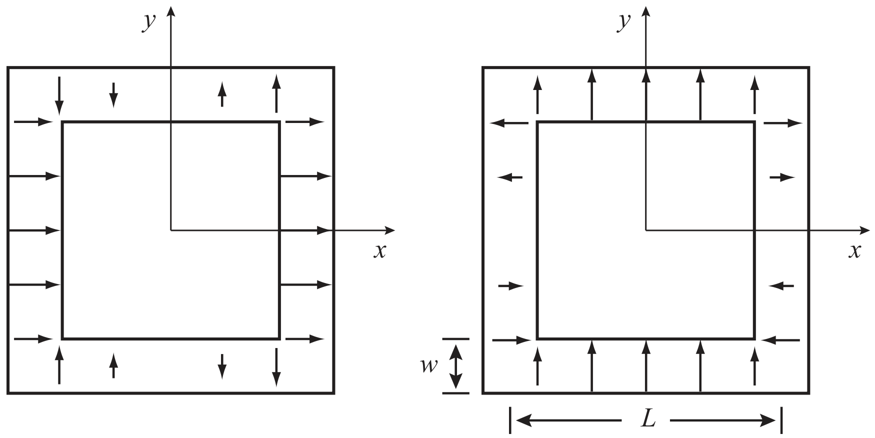

Figure 3.1: Electric field distributions of the two orthogonal voltage modes, $\mathbf{\Psi_x}$ (left) and $\mathbf{\Psi_y}$ (right) assuming $w \ll \lambda$. The voltage is defined from the inside to the outside of the slot-ring.

In a lossless resonator, resonance occurs when $\Gamma_l \Gamma_r = 1$, where Γ_l and Γ_r are the reflection coefficients looking left and right, respectively, from an arbitrary point on the resonator. This is satisfied by either of the following conditions:

$$Z_l + Z_r = 0 \tag{3.1a}$$

$$Y_l + Y_r = 0, \tag{3.1b}$$

where Z_l and Z_r are the impedances looking left and right, respectively, from an arbitrary point on the resonator, and Y_l and Y_r are the respective admittances.

Consider the loaded slot-ring antenna shown in Fig. 3.2(a). The antenna is loaded along the x and y axes with shunt capacitances C_{x1}, C_{x2}, C_{y1}, and C_{y2}. If symmetry is imposed, the resonator can be analyzed by even and odd mode analysis, as shown below.

3.1.1 Two Planes of Symmetry

The loaded slot-ring resonator is symmetric about both the x-z and y-z planes if $C_{x1} = C_{x2}$ and $C_{y1} = C_{y2}$. There are three unique combinations of symmetry:

even-odd, even-even, and odd-odd.

even-odd

Let the voltage be even with respect to the y-z plane and odd with respect to the x-z plane. The equivalent circuit is shown in Fig. 3.2(b). The resonance condition is found by applying (3.1b) at $x = 0$, and is given by

$$\omega C_y Z_s \tan(\beta L) = 2. \tag{3.2}$$

These modes have the same symmetry properties as Ψ_y (no loading), and the fundamental resonance occurs when $\beta L < \frac{\pi}{2}$. Therefore, the fundamental mode, ψ_y is a tuned version of Ψ_y:

$$\psi_y = \frac{1}{\sin(\beta_y L)} \begin{cases} \sin(\beta_y y) & x = \pm L/2, \\ \sin(\beta_y (L - |x|)) & y = L/2, \\ -\sin(\beta_y (L - |x|)) & y = -L/2, \end{cases} \tag{3.3}$$

where β_y is the propagation constant in the slot at the fundamental resonance, f_{0y}, and ψ_y has a maximum value of 1.

If the symmetry planes are rotated 90°, the tuned version of Ψ_x can be found. The resonance condition is

$$\omega C_x Z_s \tan(\beta L) = 2, \tag{3.4}$$

and the eigenmode is

$$\psi_x = \frac{1}{\sin(\beta_x L)} \begin{cases} \sin(\beta_x x) & y = \pm L/2, \\ \sin(\beta_x (L - |y|)) & x = L/2, \\ -\sin(\beta_x (L - |y|)) & x = -L/2, \end{cases} \tag{3.5}$$

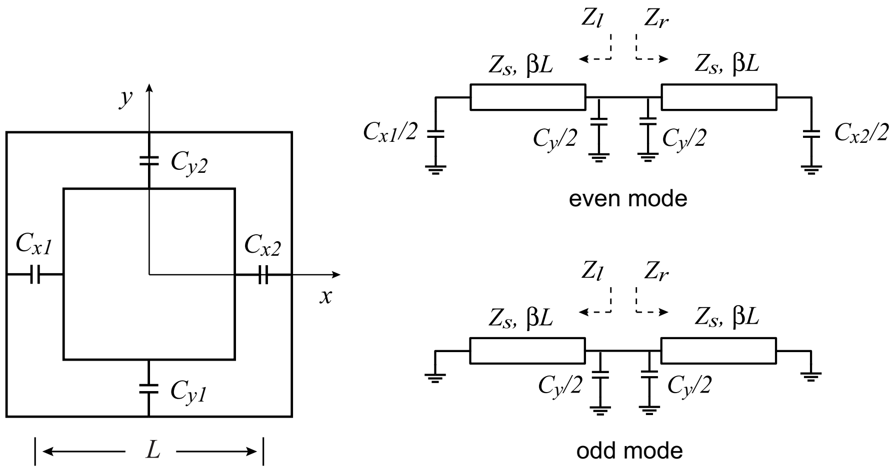

(a) (b)

Figure 3.2: (a) Slotring antenna loaded along the x and y axes. (b) Equivalent circuits of the even and odd modes with respect to the x-z plane assuming $C_{y1} = C_{y2} = C_y$.

where β_x is the propagation constant in the slot at the fundamental resonance, f_{0x}. The implication of (3.2) and (3.4) is that if $C_{x1} = C_{x2} = C_x$ and $C_{y1} = C_{y2} = C_y$, there are two resonant modes, ψ_x and ψ_y, that can be tuned independently. f_{0x} is plotted in Fig. 3.3 for $L = 26$ mm, $w = 3$mm, and a 0.79-mm-thick substrate with $\epsilon_r = 2.2$. This model predicts tuning from 2 to 1.25 GHz as C_x varies from 0.5 to 2.5 pF.

even-even

The even-even modes are dependent on both C_x and C_y, and are found by applying (3.1b) to the even mode circuit in Fig. 3.2(b). Resonance occurs when $Y_l = Y_r = 0$, or equivalently:

$$C_x C_y Z_s \tan(\beta L)\omega^2 - 2(C_x + C_y)\omega - \frac{4}{Z_s}\tan(\beta L) = 0. \tag{3.6}$$

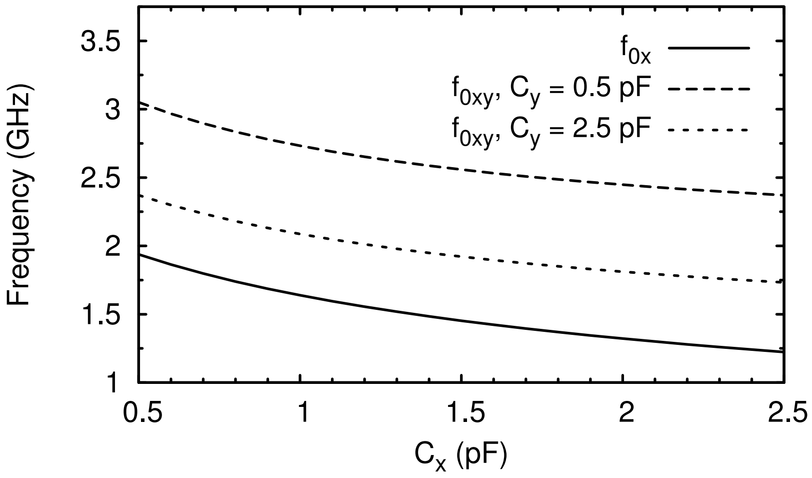

Figure 3.3: Calculated resonance frequencies of the fundamental $\hat{x}$-polarized mode, ψ_x, and the higher order mode ψ_{xy} as a function of C_x when $L = 26$ mm and $w =$ 3mm. The substrate is 0.79 mm thick with $\epsilon_r = 2.2$.

The resonance frequency, f_{0xy}, of the lowest order mode, ψ_{xy}, is higher in frequency than both f_{0x} and f_{0y}. This can be seen for f_{0x} by the following: ψ_x occurs when the capacitively terminated stubs are at their first series resonance ($Z_l = Z_r = 0$), but ψ_{xy} occurs when they are inductive (above the first series resonance) and resonate with $C_y/2$. The same is shown for f_{0y} by exchanging C_x and C_y. f_{0xy} is plotted versus C_x for different values of C_y in Fig. 3.3.

odd-odd

The odd-odd modes all have short circuit points at the locations of all capacitors, and therefore, the capacitors have no effect. Solutions occur when $\beta L = n\pi$ where n is a positive integer, and the first resonance occurs when the circumference of the slot is two wavelengths.

3.1.2 One Plane of Symmetry

If $C_{x1} \neq C_{x2}$ but $C_{y1} = C_{y2} = C_y$, the resonator is symmetric about the x-z plane and there are both odd and even solutions. It can be seen that the odd-mode equivalent circuit (Fig. 3.2(b)) is actually symmetric about the y-z plane, and the solution is ψ_y. Therefore, only the even mode will be analyzed.

One set of even-mode frequencies are found by (3.1a) and occur when

$$Y_y Z_{le}^{'} Z_{re}^{'} = -(Z_{le}^{'} + Z_{re}^{'}). \tag{3.7}$$

where

$$Z_{le}^{'} = Z_s \frac{2 + jY_{x1} Z_s \tan(\beta L)}{Y_{x1} Z_s + j2 \tan(\beta L)} \tag{3.8a}$$

$$Z_{re}^{'} = Z_s \frac{2 + jY_{x2} Z_s \tan(\beta L)}{Y_{x2} Z_s + j2 \tan(\beta L)} \tag{3.8b}$$

are the impedances of each side neglecting Y_y, and

$$Y_y = j\omega C_y, \quad Y_{x1} = j\omega C_{x1}, \quad Y_{x2} = j\omega C_{x2} \tag{3.9}$$

are the admittances of the loading capacitors. If C_{x1} and C_{x2} are nearly equal, the fundamental mode, $\psi_x^{'}$, is similar to ψ_x; the important difference being that its short circuit locations are not on the y-axis, and therefore, it is dependent on C_y.

Another set of resonances can be found from (3.1b), and resonance occurs when

$$Y_{le} + Y_{re} = \frac{1}{Z_{le}^{'}} + \frac{1}{Z_{re}^{'}} + Y_y = 0. \tag{3.10}$$

When C_{x1} and C_{x2} are nearly equal, this resonance is similar to ψ_{xy}, which can be seen by noting that (3.10) reduces to (3.6) if $C_{x1} = C_{x2}$.

3.2 A Demonstration of Independent Tuning with Fixed Capacitors

The antenna design and results presented in this section were previously presented in [22].

3.2.1 Design and Fabrication

The slot-ring antenna geometry is shown in Fig. 3.4(a). It is square in shape with an inner circumference of 40 mm, a slot width of 3 mm, and is fed by 76 Ω open-circuited microstrip lines. The antenna was designed to operate in the first resonance, and to be $\hat{x}$-polarized when fed at port P_x and $\hat{y}$-polarized when fed at port P_y. It was also designed to tune both polarizations independently and to have 20 dB of isolation between P_x and P_y in the band of operation for all tuning states.

Let Ψ_x and Ψ_y be the resonant slot-ring modes excited by P_x and P_y respectively. Independent tuning and good isolation can be achieved if the antenna is loaded symmetrically about both the x-z and y-z planes because then Ψ_x has short-circuit points on the y-axis and Ψ_y has short-circuit points on the x-axis. If Ψ_x has short-circuit points on the y-axis, the slot voltage distribution has odd symmetry with respect to the microstrip feed connected to P_y, and therefore, there is no coupling. Furthermore, C_{y1} and C_{y2} have no effect on Ψ_x. Loading comes from both the tuning capacitors and the microstrip feed. Therefore, symmetry was maintained by requiring that $C_{x1} = C_{x2}$ and $C_{y1} = C_{y2}$, and by placing microstrip reactive loads directly across from the feeds. The microstrip reactive loads were chosen for three reasons. First, they allow the loading capacitor pairs to have the same value, second, they have a similar frequency response to the microstrip feed, and finally, they add no cost to the antenna fabrication.

The final geometry was determined by tuning all microstrip stub lengths with a

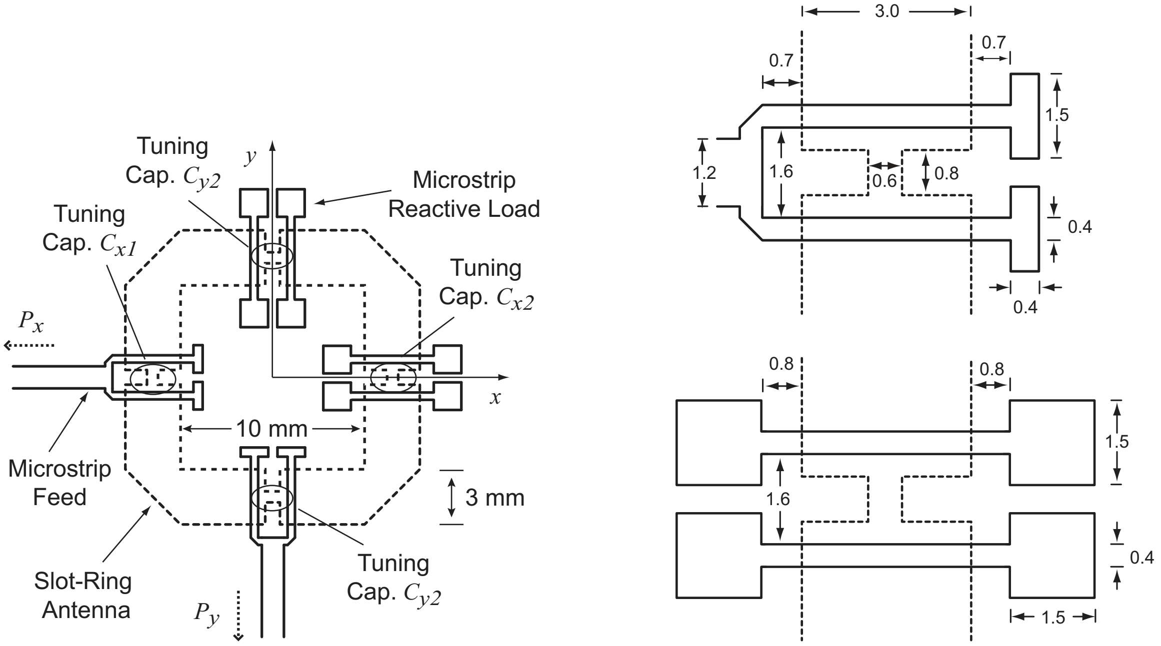

(a) (b)

Figure 3.4: (a) Dual-polarized slot-ring antenna geometry with loading capacitors. (b) Geometry of the microstrip feeds and reactive loads. All dimensions are in millimeters.

planar full-wave solver [24] until the antenna was matched to 75 Ω and the isolation was better than 20 dB over the desired frequency tuning range. The slot-ring resonator was chosen to be the same as in the single-polarized fixed-capacitor demonstration in Chapter 2 for comparison purposes. The antenna was printed on a a 60 x 60 mm^2 copper-clad Taconic TLY5 substrate ($\epsilon_r = 2.2$) with a thickness of 0.787 mm using standard photolithography techniques. Several identical copies of the antenna (including some without the microstrip reactive loads) were fabricated on the same board and then loaded with different capacitance values. End-launch PCB-mount SMA to microstrip transitions were soldered to each antenna at the edge of the substrate. Before mounting the loading capacitors (AVX ACCU-P), the capacitance of each capacitor was measured at 30 MHz and the unloaded frequency responses of the antennas were verified to be consistent with each other.

3.2.2 Results and Discussion

The two port S-parameters of each antenna were measured with a vector network analyzer (Agilent E5071B). The network analyzer was calibrated by the TRL method to the 76 Ω microstrip line and the calibration plane was 14 mm from the microstrip split. Fig. 3.5(a) shows the measured S-parameters of the unloaded antenna without the microstrip reactive loads and Figures 3.5(b)-(f) show the measured S-parameters of the antennas with different loading capacitance combinations. Comparing Figs. 3.5(a) and 3.5(b), it is apparent that the microstrip reactive loads improve the isolation at the resonant frequency from 11 to better than 20 dB, but reduce the resonance frequency from 4.9 to 4.4 GHz. As C_x varies from 0.1 to 0.7 pF with C_y held constant at 0.1 pF (Figures 3.5(c)-(e)), the resonance frequency of Ψ_x, f_x, changes from 3.7 to 2.2 GHz but the resonance frequency of Ψ_y, f_y, remains constant at 3.7 GHz. It can be seen, however, that when C_x is 0.7 pF and C_y is 0.1 pF, a second order resonance is close enough in frequency to f_y that it interacts with Ψ_y. As C_y increases, C_x can be increased beyond 0.7 pF while keeping f_y below the second order resonance frequency.

The radiation pattern of each antenna was measured in a Satimo Stargate 32 antenna measurement system courtesy of Qualcomm, and the patterns of two representative antennas are plotted in Fig. 3.6. The shape of the patterns does not change considerably as the antenna is loaded, but the gain decreases. The gain is 5 dB at 4.4 GHz, 4.3 dB at 3.0 GHz, and 2.2 dB at 1.92 GHz.

Circularly polarized patterns were simulated, and are shown in Fig. 3.7. The simulated axial ratio is better than 2 dB between -30° and 30° at 4.4 GHz, and between -50° and 50° at 1.92 GHz. The axial-ratio beamwidth is wider at 1.92 GHz because the directivity of each mode is lower. It is important to note that the polarization sense is opposite on each side of the antenna.

It has been shown that the slot-ring antenna is capable of dual-polarized operation

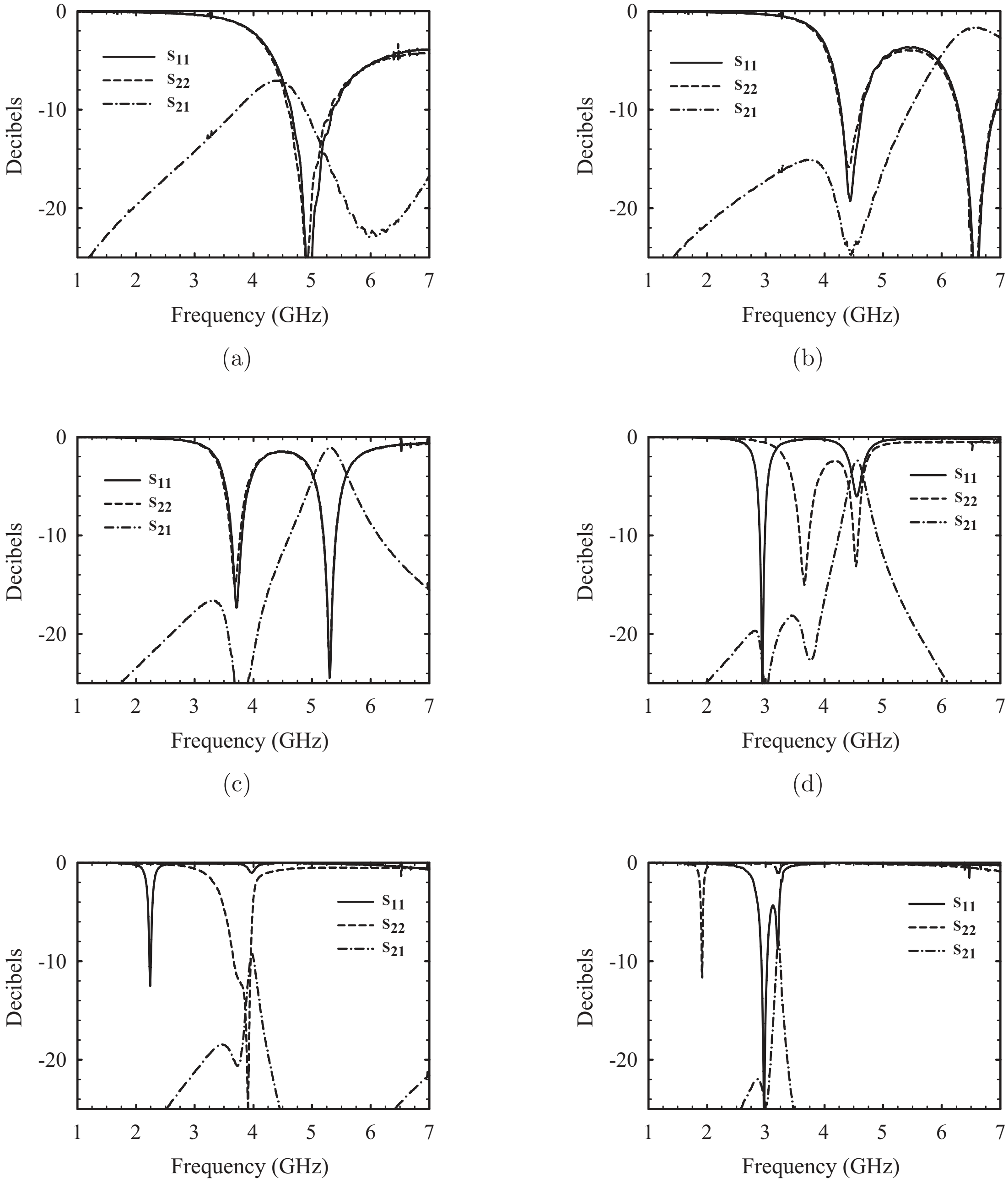

(a) (b)

(c) (d)

(e) (f)

Figure 3.5: Measured S-parameters with (a) $C_x = C_y = 0$ and no microstrip reactive loads, (b) $C_x = C_y = 0$, (c) $C_x = C_y = 0.1$, (d) $C_x = 0.3$ and $C_y = 0.1$, (e) $C_x = 0.7$ and $C_y = 0.1$, and (f) $C_x = 0.3$ and $C_y = 1$ pF. The characteristic impedance is 76 Ω.

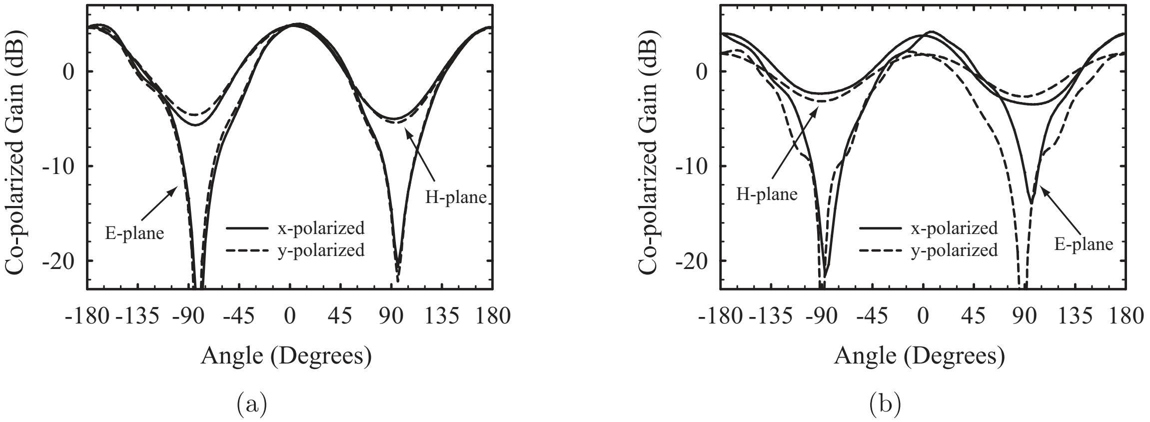

Figure 3.6: Measured radiation patterns at (a) $f_x = f_y = 4.4$ GHz and (b) $f_x = 3.0$ and $f_y = 1.92$ GHz.

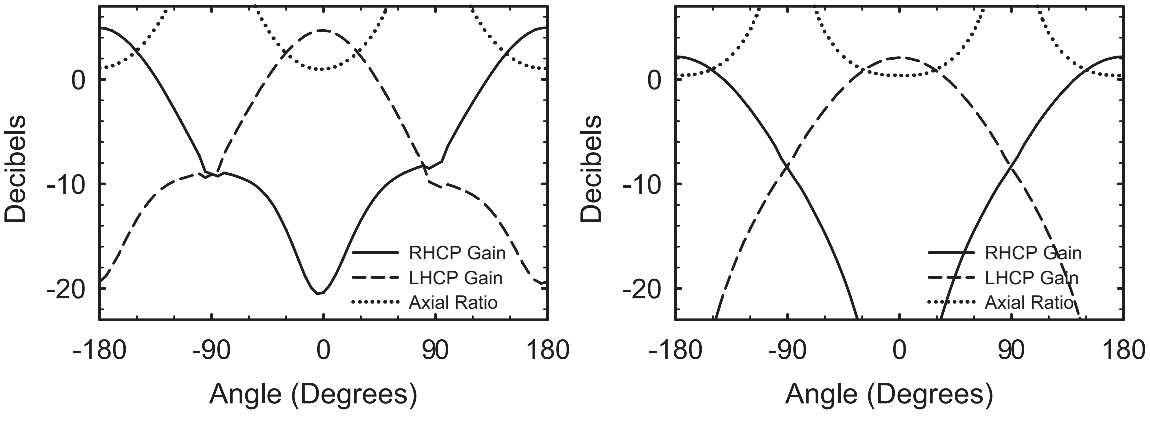

Figure 3.7: Simulated circularly-polarized radiation patterns at (a) 4.4 GHz and (b) 1.92 GHz.

with independent tuning of each polarization when $C_{x1} = C_{x2}$, $C_{y1} = C_{y2}$, and reactive loads are used to balance the loading of the microstrip feed.

3.3 A Varactor-Tuned Dual-Polarized Antenna from 0.93–1.6 GHz

Whereas the fixed-capacitor-loaded antennas in the previous section demonstrated both the dual-polarized tuning capability of slot-ring antenna and the necessity of the reactive loads in providing >18 dB of port-to-port isolation, true tuning elements and the biasing scheme necessary to achieve independent tuning is demonstrated by the antenna presented in this section.

3.3.1 Design

The varactor-tuned dual-polarized slot-ring antenna is made by feeding the slot-ring resonator along both the x and y axes as shown in Fig. 3.8. The microstrip lines continue along the x and y axes to port 1 and port 2, respectively, at the edges of the 70×70 mm^2 substrate where SMA connectors are attached. The same slot-ring is used for both the single- and dual-polarized designs, so the dimensions that are not specified in Fig. 3.8 can be found in Fig. 2.7. The substrate is 0.787 mm Taconic TLY-5 substrate ($\epsilon_r = 2.2$, $\tan\delta = 0.0009$).

It has already been shown that there are two orthogonal resonant modes, ψ_x and ψ_y, that can be tuned independently if the antenna is symmetric about both the x and y axes. The microstrip feeds destroy this symmetry by adding reactance to C_{x1} and C_{y1}, and therefore, microstrip reactive loads were placed opposite the feeds to restore the symmetry. If symmetry were not restored, ports 1 and 2 would couple to resonant modes, $\psi_x^{'}$ and $\psi_y^{'}$, that cannot be tuned independently because $\psi_x^{'}$ is not zero on the y axis, and likewise, $\psi_y^{'}$ is not zero on the x axis. For the same reason, there would be significant coupling between ports 1 and 2. This port-to-port coupling, and the effectiveness of the microstrip reactive loads in reducing it, were demonstrated in [22], where the isolation at the center frequency was improved from 11 dB to >20 dB with the use of the reactive loads. A side effect of the reactive loads is that they reduce the resonance frequency for a given capacitance value.

The reactive loads have the same shape as the microstrip-to–slot-antenna transitions except for the width of the end stub, which was tuned using IE3D to result in maximum isolation at $V_{bx} = V_{by} = 20$ V (Fig. 3.8(b), Fig. 3.9(a)). They have a similar frequency response to the feed transition, and therefore, provide wideband decoupling of ports 1 and 2.

Capacitive loading is achieved by placing varactor diodes (M/A-Com MA46H071-1056, 2.5 - 0.45 pF from 0 - 20 V) across the slot as shown in Fig. 3.8. Independent tuning is achieved with the following conditions:

$$\begin{aligned}
C_{x1} = C_{x2} = C_x \quad &\Longrightarrow \quad V_{bx1} = V_{bx2} = V_{bx} \\
C_{y1} = C_{y2} = C_y \quad &\Longrightarrow \quad V_{by1} = V_{by2} = V_{by} \\
C_x \text{ and } C_y \text{ independent} \quad &\Longrightarrow \quad V_{bx} \text{ and } V_{by} \text{ independent,}
\end{aligned}$$

where V_{bx} and V_{by} are the $\hat{x}$- and $\hat{y}$-polarized bias voltages. A 150 μm gap is cut in the center part of the slot-ring in order to decouple V_{bx} and V_{by}, and 22 pF capacitors (AVX ACCU-P, 0603, 1.8 GHz SRF) are placed across the gaps to allow the RF current to pass. The bias voltages are applied to the center part of the slot-ring from the RF line through 100 kΩ resistors and via holes.

3.3.2 Results and Discussion

The two-port S-parameters of the dual-polarized slot-ring antenna were measured using an Agilent E5071B network analyzer at all combinations of V_{bx} and V_{by} in

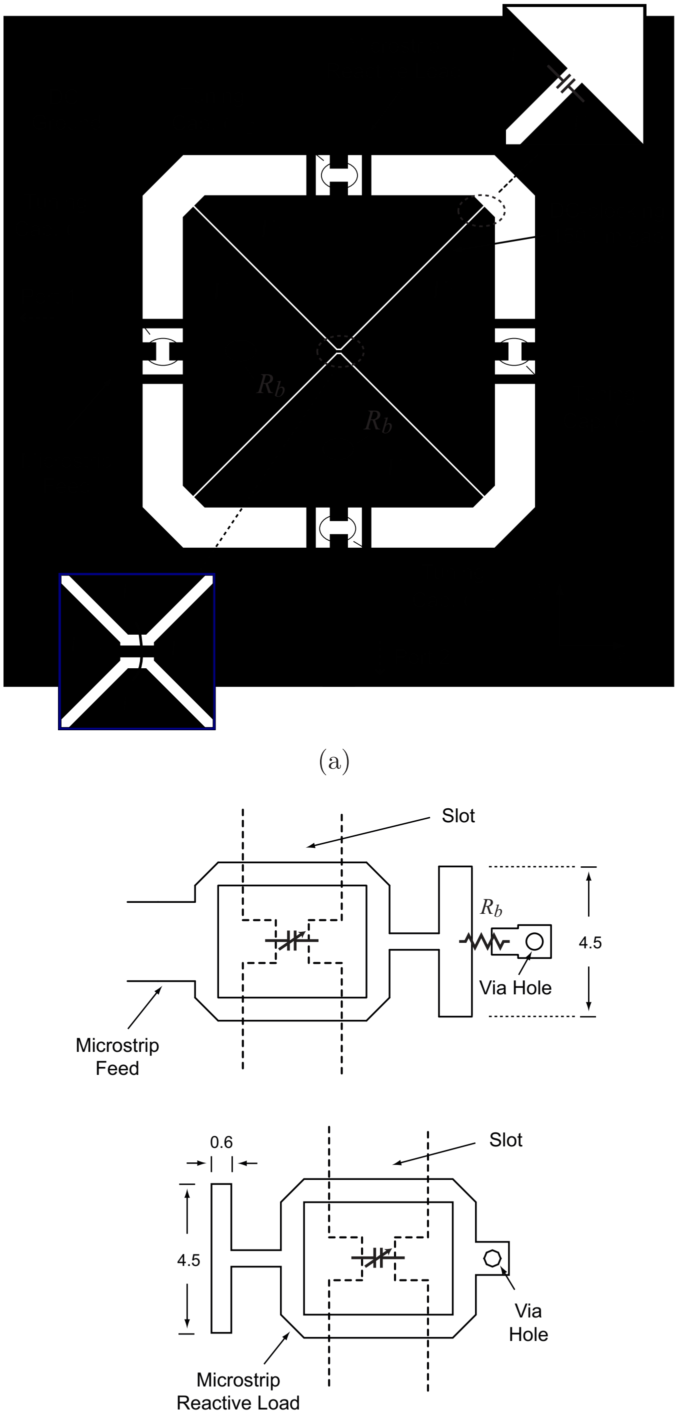

(a)

(b)

Figure 3.8: Layout of (a) the slot-ring antenna and (b) the microstrip to slot antenna transition and microstrip reactive loads. All dimensions are in millimeters; dimensions that are not specified are the same as in Fig. 2.7.

$\{0, 1, 2, 4, 8, 20\}$. Ferrite beads were placed on the cable at the connection to the antenna to reduce the coupling to the cable shields, and the antenna was placed on a foam block at least 1 m away from any scatterers. Figure 3.9 shows the S-parameters of four different combinations of V_{bx} and V_{by}. As V_{bx} is held at 20 V and V_{by} varies from 20 to 0 V, the $\hat{x}$-polarized center frequency, f_{0x}, remains nearly constant and the $\hat{y}$-polarized center frequency, f_{0y}, varies from 1.6 GHz to 0.93 GHz with better than -14 dB isolation. As V_{bx} changes, f_{0x} changes accordingly without changing f_{0y}.

It is apparent that there is a second resonance in which ports 1 and 2 are moderately coupled. This resonance, ψ_{xy}, occurs at a frequency, f_{0xy} (Eq. (3.6)), that is higher than both f_{0x} and f_{0y}, and is dependent on both C_x and C_y. When C_x is small and C_y is large, f_{0xy} is very close to f_{0x} and the impedance match and isolation are degraded.

The S-parameters of all 36 bias-voltage combinations are summarized in Figures 3.10 and 3.11. Both f_{0x} and the $\hat{x}$-polarized 10-dB impedance bandwidth, B_{10dBx}, are nearly constant as V_{by} varies from 0 to 20 V, except for the points where V_{bx} is large and V_{by} is small. Figure 3.11 shows the minimum port-to-port isolation within B_{10dBx} centered about f_{0x}. The isolation is better than 20 dB over most of the tuning range, and is 14 dB when $f_{0x} = 1.56$ GHz and $f_{0y} = 0.93$ GHz (the maximum frequency difference). If V_{bx} and V_{by} are interchanged, the $\hat{y}$-polarized center frequency, bandwidth, and isolation are nearly identical to the $\hat{x}$-polarized characteristics shown in Figures 3.10 and 3.11, as expected by symmetry.

The $\hat{x}$-polarized radiation patterns were measured at several bias voltage combinations. Port 1 was connected to the RF source through a bazooka balun (centered at either 0.8 or 1.6 GHz), and a coaxial cable with ferrite beads was connected to port 2 in order to set V_{by}. The $\hat{y}$-polarized antenna patterns were not measured, but should be nearly identical to the $\hat{x}$-polarized patterns due to symmetry.

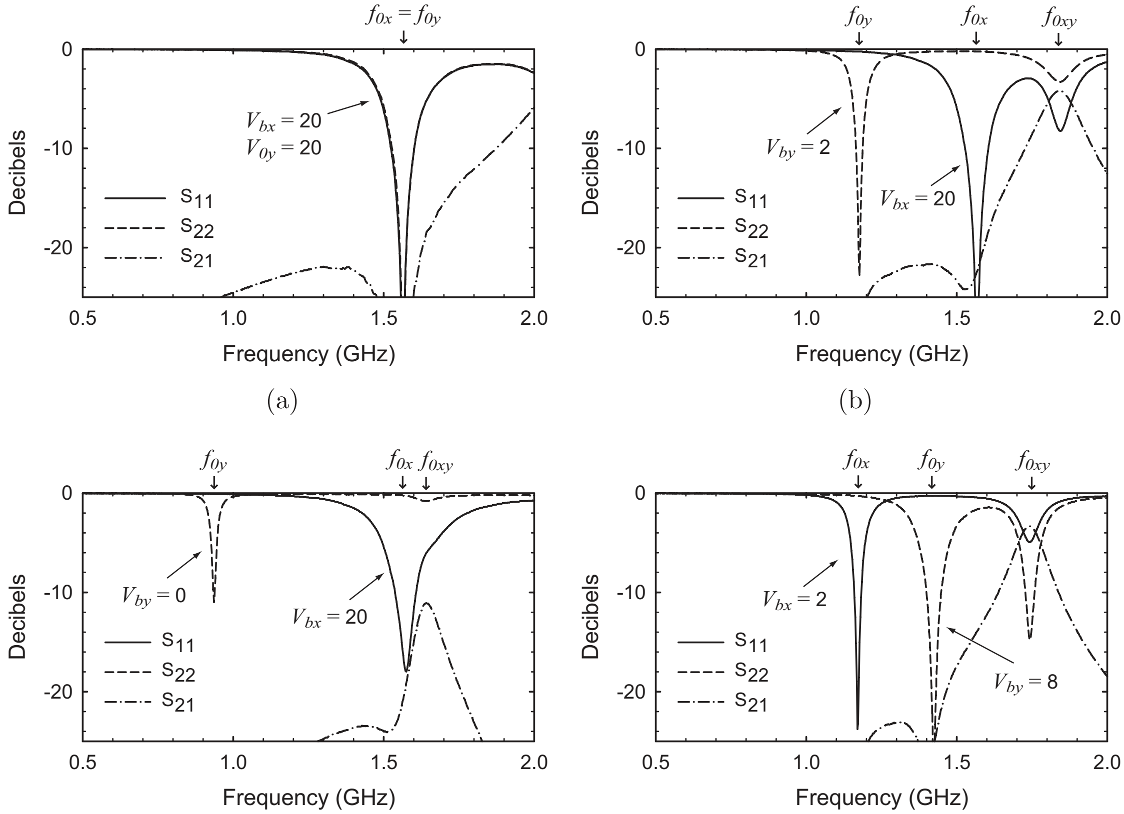

(a) (b)

(c) (d)

Figure 3.9: Measured s-parameters when (a) $V_{bx} = V_{by} = 20$ V, (b) $V_{bx} = 20$ V, $V_{by} = 2$ V, (c) $V_{bx} = 20$ V, $V_{by} = 0$ V, and (d) $V_{bx} = 2$ V, $V_{by} = 8$ V.

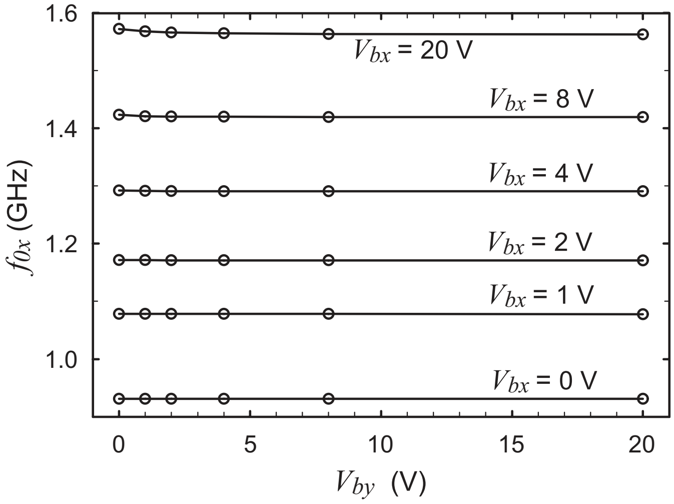

(a)

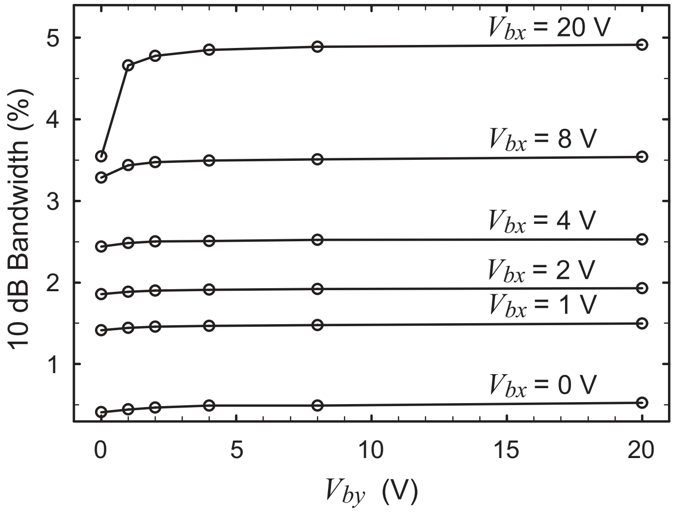

(b)

Figure 3.10: Measured $\hat{x}$-polarized (a) center frequency and (b) 10-dB bandwidth at different V_{bx} and V_{by}.

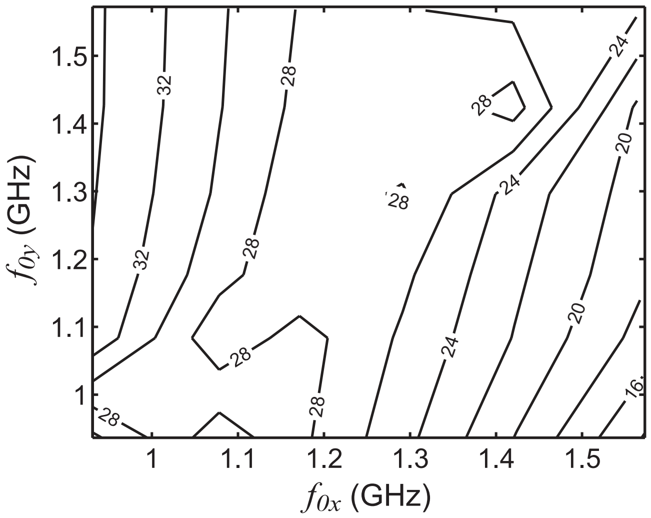

Figure 3.11: Measured port-to-port isolation (in decibels) within B_{10dBx} centered about f_{0x}.

As expected, the radiation patterns and efficiencies are very similar to those of the single-polarized antenna. The measured and simulated efficiencies at 0.93 GHz are 20% and 25%, respectively; at 1.6 GHz, they are 85% and 93% respectively. The agreement between the measured and simulated efficiencies at 1.6 GHz, which is at the center frequency of the balun, suggest that the measured efficiency at 0.93 GHz would be closer to 25% if a 0.93 GHz balun were used.

The measured radiation patterns at 0.93 and 1.56 GHz are shown in Fig. 3.12. The H-plane patterns are smooth despite the fact that a coaxial cable was attached to port 2 during the measurement. This supports the theory that placing the feed cable of the single-polarized antenna in the H-plane will improve the efficiency and make the pattern smoother. The simulated cross-polarization levels are below −25 dB in the principle planes and, even with the scattering from the two cables feeding the antenna at ports 1 and 2, the measured cross-polarization levels are at least −15 dB at most angles at 1.43 and 1.56 GHz.

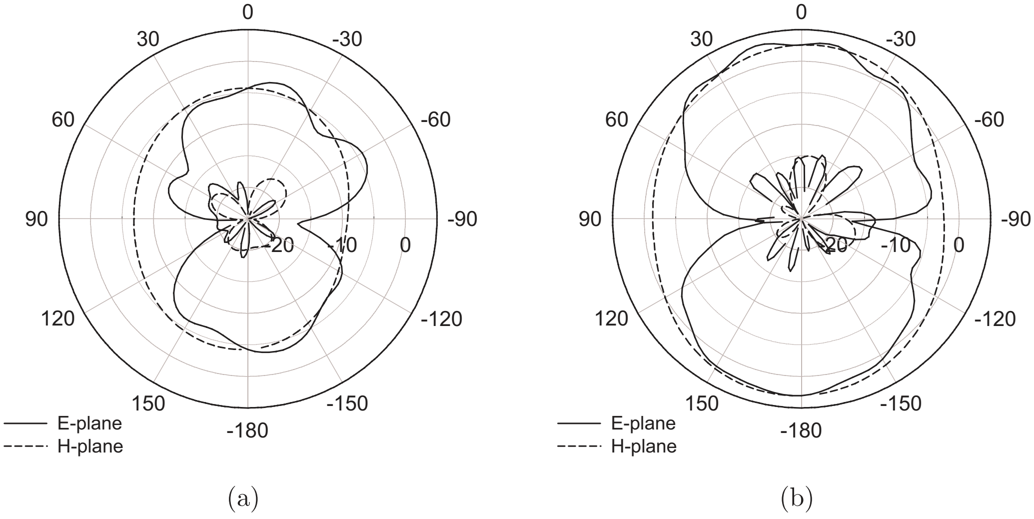

Figure 3.12: Measured $\hat{x}$-polarized E and H-plane patterns of the dual-polarized antenna at (a) 0.93 GHz when $V_{bx} = 0$ V and $V_{by} = 4$ V, and (b) 1.56 GHz when $V_{bx} = V_{by} = 20$ V.

Chapter 4

Shallow Varactor-Tuned Cavity-Backed Slot Antennas

Previously demonstrated wideband-tunable slot antennas have two-sided radiation, and therefore, are unsuitable for conformal mounting on a ground-plane, printed circuit board, or other scattering object. The Cavity-Backed-Slot (CBS) antenna achieves single-sided radiation by placing a conducting enclosure behind the slot. Although CBS antennas are not usually thought of as being planar, two shallow ($\approx 0.025\ \lambda$) cavity-backed slot antennas have recently been demonstrated that are compatible with printed circuit-board fabrication techniques. The first is a circularly-polarized crossed-slot that is fed by a single coaxial probe [28], and the second is a one-wavelength microstrip-fed linear slot [29]. A ferrite-tuned cavity backed slot antenna has been tuned over a small range [30], but no tunable CBS was found in the literature. This chapter first discusses the operation of the shallow cavity-backed slot, and then a CBS antenna is presented that is compatible with planar printed circuit board fabrication techniques and tunes from 1.0–1.9 GHz using a varactor diode. Finally, the miniaturization of the tunable CBS antenna is discussed in light of efficiency and bandwidth.

4.1 CBS Antenna Background

4.1.1 Methods to Achieve Single-Sided Radiation from a Slot Antenna

There are several methods used to direct the radiation of a slot antenna to a single side of the substrate. The structure is often designed so that the reflected field is in phase with the field in the slot aperture—i.e. appearing as an open circuit, and therefore, adding no susceptance to the slot admittance at resonance [31]. The ideal solution would be to place a perfect magnetic conductor (which is an open circuit at all frequencies) a small distance below the slot. This would enable one to make any existing tunable slot antenna one-sided with minimal change to the antenna itself, but no known material acts as a wideband perfect magnetic conductor at microwave frequencies. Slot antennas have been demonstrated, however, over artificial high impedance surfaces [32, 33], and have limited bandwidth. Spiral antennas with decade bandwidth have been made one-sided using absorptive cavities [34], but the efficiency suffers. Another solution is to place a conducting plane a distance of $\lambda/4$ behind the slot [31, 35]. This method suffers from poor efficiency due to coupling to the parallel plate waveguide created by the slot and reflector planes. Similarly, the radiation from the slot can be directed mostly to one side by placing it on a substrate with a high dielectric constant, but a significant amount of power is coupled to substrate modes. This is overcome by using a dielectric lens instead of a planar substrate layer [36], but the size and weight of such a lens is prohibitive for many microwave applications.

In the CBS, a conducting enclosure behind the slot directs all of the radiation to the other side. This antenna is highly efficient because there is little absorption in the cavity, but the bandwidth is limited (especially at the fundamental resonance) because the cavity strongly loads the slot.

4.1.2 Calculation of the Input Impedance

Cavity-backed-slot antennas have been studied extensively; more than 50 papers on the subject have been published in the IEEE as of the year 2007. Two methods of feeding the antenna are considered: either the slot is excited itself, in which case the cavity is a load, or the cavity is excited, in which case the slot is the load. The latter case has been analyzed in the literature [37, 38], but only the case where the slot is directly excited is considered in this chapter.

Previous models

Perhaps the most important consideration in designing a CBS antenna is the effect of the cavity on the admittance of the antenna. The admittance of the antenna is generally calculated by dividing the problem into two parts—the cavity and freespace—and adding the admittances. A simple method presented by Cockrell is to assume a sinusoidal aperture distribution and find the cavity fields by mode-matching. The contribution of the cavity to the antenna susceptance is calculated by the complex Poynting theorem [39]. Galejs calculated the admittance using a variational approach to better approximate the aperture field [40]. A more accurate approach is to solve for the aperture field using the Method of Moments [41], but the previously mentioned methods seem to be sufficient for many cases.

An intuitive approach was presented by Liang which expresses cavity as a terminated waveguide section that is coupled to the slot antenna through an ideal transformer [42]. The admittance of the slot and the admittance of each mode, whether propagating or not, add in parallel:

$$Y_{in} = Y_A - j \sum_n A_n^2 Y_n \cot(k_n d), \tag{4.1}$$

where Y_{in} is the impedance at the feed, Y_A is the admittance of the slot on the

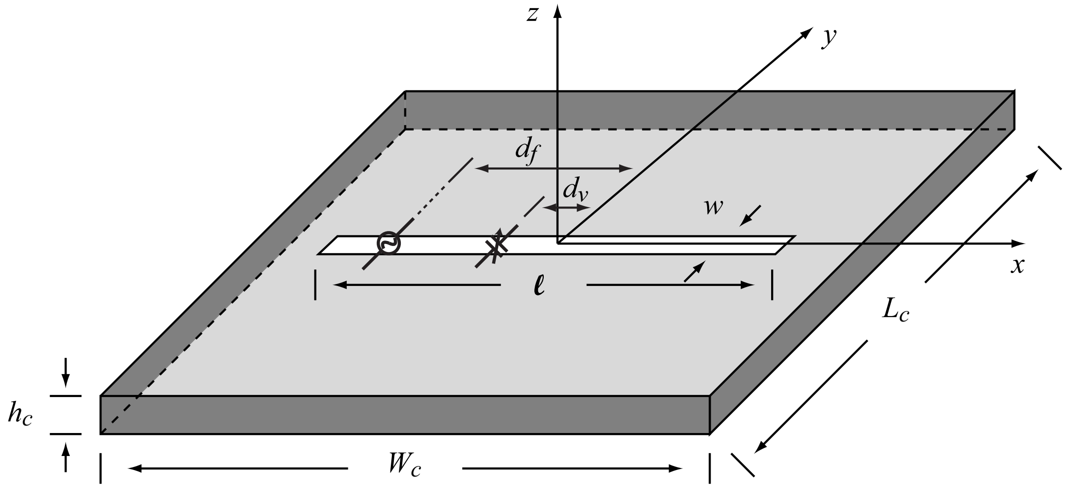

Figure 4.1: Geometry of the shallow varactor-tuned cavity-backed slot antenna.

radiating side, Y_n is the characteristic admittance of each mode, and $A_n =< E_s, e_n >$ is the coupling coefficient of the aperture field to each mode. This approach is used to intuitively understand how a CBS antenna can be tuned with a varactor diode.

Waveguide model for shallow symmetric CBS antennas

Consider a shallow rectangular cavity with length, L_c, width, W_c, and height $h_c \ll \lambda$, (Fig. 4.1) whose top conducting sheet extends infinitely in the x-y plane. A slot—with length, ℓ, in the $\hat{x}$ direction and width, $w \ll \lambda$, in the $\hat{y}$ direction—is cut in the center of the top wall and is excited by a gap source a distance d_f from the center. It is helpful to notice that the x-z plane is a PEC symmetry plane (Fig. 4.2(a)), and therefore, no cavity mode that exhibits PMC symmetry about the x-z plane will be excited. For example, the cavity may be resonant in the TE_{110} mode ($\lambda/\sqrt{2} \times \lambda/\sqrt{2}$), but this mode is not excited when the slot is in the center.

The odd-mode structure (Fig. 4.2(b)) is a slot that radiates into the quarter-space constrained by the infinite ground plane and the PEC symmetry plane. The slot is backed by a folded short-circuited waveguide stub, and the equivalent circuit is given in Fig. 4.3(a) assuming that the TE_{10} mode is dominant. The validity of

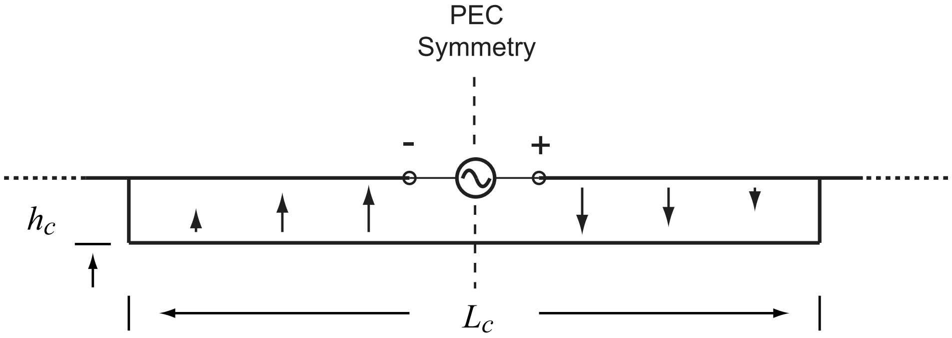

(a) Full structure

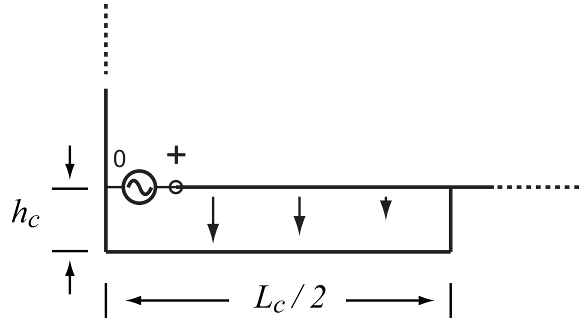

(b) Equivalent structure

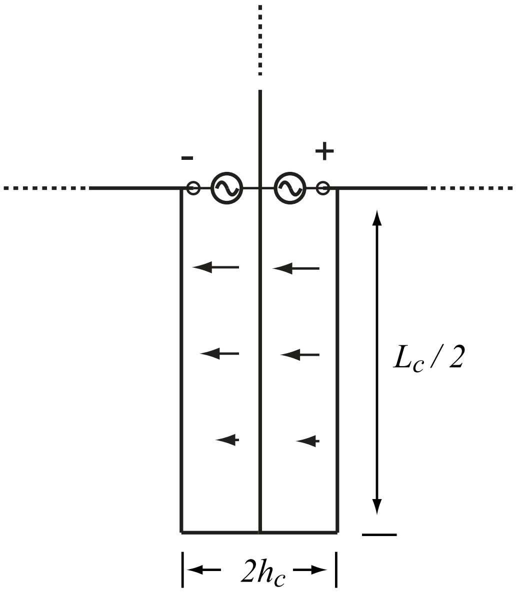

(c) Wrapped approximation

Figure 4.2: Cross sectional view of the shallow cavity-backed slot. There is a PEC symmetry plane when the slot is at the center and the excitation is across the slot.

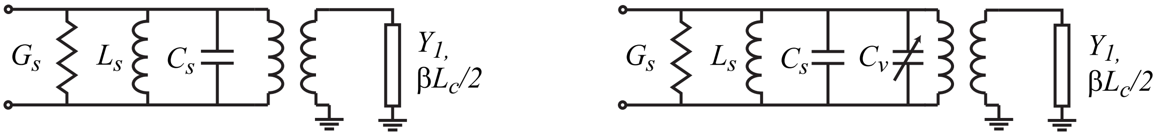

(a) Unloaded (b) Varactor placed at excitation point

Figure 4.3: Equivalent circuit of the unloaded and capacitively loaded cavity-backed slot assuming one dominant mode in the cavity.

this assumption is based mostly on the magnitude of the Fourier coefficients, A_n, and the TE$_{10}$ mode can be either propagating or evanescent. The radiation conductance and slot inductance and capacitance are represented by G_s, L_s, and C_s, respectively. The susceptance of all higher order modes, as well as due to the waveguide corner, can be absorbed into L_s and C_s. Calculating the coupling coefficients A_n, is not as straightforward due to the folding of the cavity and will not be attempted here. However, it is clear that the slot couples significantly to the TE$_{10}$ mode if it is near its first resonance because its voltage distribution is nearly the same as that of the TE$_{10}$ mode.

The waveguide section appears as an open circuit (parallel resonance) at the frequency f_1 when

$$\beta\frac{L_c}{2} = \frac{\pi}{2}, \tag{4.2}$$

where

$$\beta^2 = k^2 - k_c^2, \tag{4.3}$$

k is the propagation constant in the material filling the waveguide, and k_c is the cutoff wave number of the TE$_{10}$ mode. The resonance frequency of the antenna, f_0, occurs when $\Im[Y_{in}] = 0$, and is determined by both the waveguide section and the slot. If the slot resonance frequency, f_s, is equal to f_1, then $f_0 = f_s = f_1$; otherwise, f_0 is between f_s and f_1.

Table 4.1: Dimensions of the shallow CBS antenna in both millemeters and wavelengths at 2 GHz. * referred to λ_d, ** referred to λ_s.

	size (wavelengths)	size (mm)
L_c	$1\sqrt{2}$ *	71
W_c	$1\sqrt{2}$ *	71
h_c	0.031 *	3.175
ℓ	0.5 **	59
w	0.025 **	3

4.1.3 Tuning the Shallow CBS

It is evident that the resonance frequency of the circuit in Fig. 4.3(a) is tuned by placing a variable capacitance in parallel with C_s (Fig. 4.3(b)). Physically, this is achieved by placing a variable capacitance across the slot in a place where the voltage is non-zero, i.e. by the same method used in the previous chapters, as well as in [7] and [8].

4.2 A Varactor-Tunable Shallow CBS covering 1–1.9 GHz

4.2.1 Design and Fabrication

The starting point of the antenna design is to choose resonant dimensions for both the slot and the cavity. The length, L_s, of the slot is $\lambda_s/2$, where $\lambda_s = \lambda_0/\sqrt{\epsilon_s}$, λ_0 is the freespace wavelength, and $\epsilon_s = 0.5(1+\epsilon_r)$ is the effective relative permittivity of the slot [15]. The cavity is square, with $L_c = W_c = \lambda_d/\sqrt{2}$, and $h_c = 0.031\lambda_d$, where $\lambda_d = \lambda_0/\sqrt{\epsilon_r}$, λ_0 is the free-space wavelength, and $\epsilon_r = 2.2$ is the relative permittivity inside of the cavity. The dimensions are summarized in Table 4.1 for an unloaded resonance frequency of 2 GHz.

Feed and loading locations

Although it is trivial to tune the resonance frequency of any slot antenna with a variable shunt capacitance, a wide-band impedance match is critical for wide-band tuning. This impedance match over a large tuning range was achieved for the slot-ring antenna (Chapter 2) by operating below resonance for every tuning state at the point where the input resistance is equal to the characteristic impedance of the system (Fig. 2.9). At this point, there is a significant series reactance, $X_A(f_0)$. For the slot-ring antennas presented in Chapter 2, the slope of $X_A(f_0)$ is such that it can be canceled with a series capacitance. An impedance match over a wide tuning range for a microstrip-fed slot antenna was also reported in [7, 8]. These results suggest that there may be combinations of feed point, d_f, and loading point, d_v, that allow the shallow CBS antenna to have a good impedance match over a wide tuning range.

A computer program was written in MATLAB [43] to search for combinations d_f and d_v that provided a return loss of better than Γ_{max} over the entire capacitance range of the varactor diode. Ten equally-spaced locations were chosen between -0.45ℓ and 0.45ℓ, and every unique location where $d_f \neq d_v$ was simulated using the IE3D MoM solver [24] (for the purpose of the impedance match, the cases (d_{f1}, d_{v1}) and (d_{f2}, d_{v2}) are identical if $d_{f1} = -d_{f2}$ and $d_{v1} = -d_{v2}$). The substrate configuration consists of two parallel infinite conducting planes separated by 3.175 mm (the top and bottom of the cavity) with dielectric material (ϵ_r =2.2) between them (Fig. 4.4). The cavity walls are modeled by vertical conducting plates between the top and bottom at $(x = \pm W_c/2, -L_c/2 < y < L_c/2)$ and $(-W_c/2 < x < W_c/2, y = \pm L_c/2$. The slot is modeled as magnetic current in the top sheet, and is excited by gap ports at d_f (port 1) and d_v (port 2). Finally, a 0.787-mm-thick layer of dielectric material is placed above the top sheet in anticipation of feeding the antenna with a microstrip line. These simulations are quite efficient for shallow cavities because only the slot and the sidewalls are meshed; the total time to simulate all 45 cases was less than 40

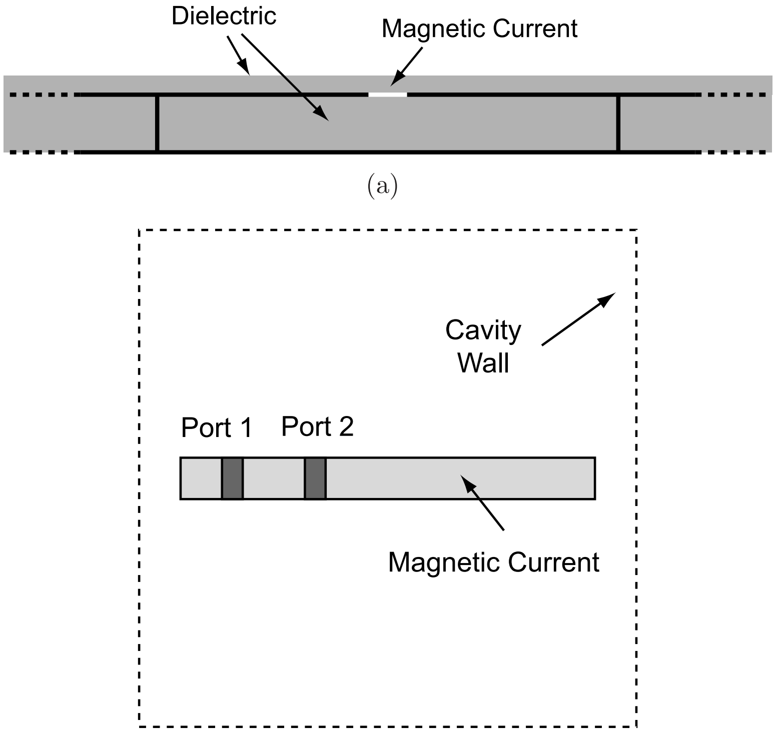

(a)

(b)

Figure 4.4: (a) Side view and (b) top view of the CBS structure that was simulated in IE3D. The horizontal layers extend to infinity.

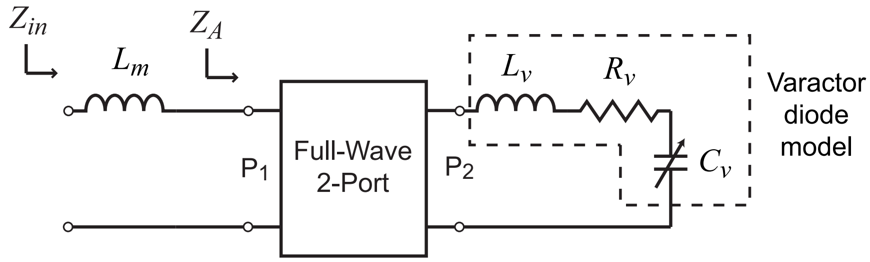

Figure 4.5: Circuit model for Z_A and Z_{in} when the antenna (Fig. 4.4) is loaded at port 2 with a varactor diode.

minutes on a 32-bit 3.2-GHz Intel Pentium IV processor.

The 2-port S-parameters from each simulation were processed by the following method to find the combinations of (d_f, d_v) that produce a good impedance match over tuning. First, Z_0 is chosen and it is decided whether the antenna will be matched by a series capacitor or inductor. The antenna impedance is then calculated by loading port 2 with a varactor diode as shown in Fig. 4.5:

$$Z_A = R_A + jX_A = Z_0 \frac{1+\Gamma_A}{1-\Gamma_A}, \tag{4.4}$$

where

$$\Gamma_A = s_{11} + \frac{s_{12}s_{21}\Gamma_v}{1 - s_{22}\Gamma_v} \tag{4.5}$$

is the reflection coefficient at port 1, and

$$\Gamma_v = \frac{Z_v - Z_0}{Z_v + Z_0} \tag{4.6}$$

is the reflection coefficient of the varactor diode with respect to the characteristic impedance Z_0. Z_v is the impedance of the varactor diode with capacitance C_v, Equivalent Series Resistance (ESR) R_v, and parasitic inductance L_v:

$$Z_v = R_v + j\omega L_v - \frac{j}{\omega C_v}. \tag{4.7}$$

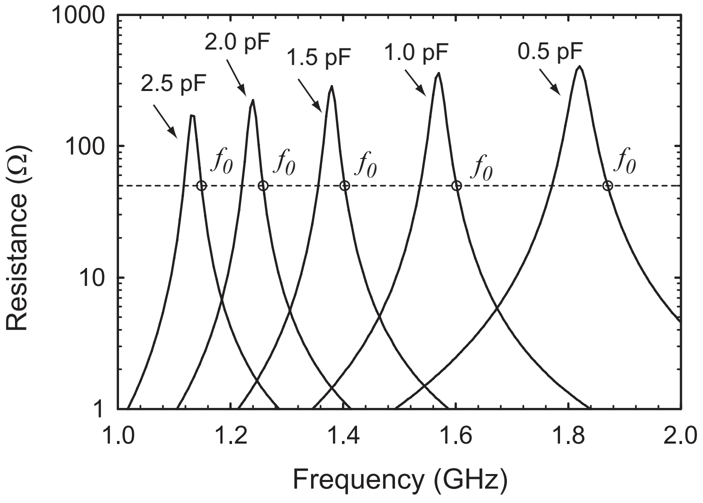

Figure 4.6: $R_A(f)$ for different C_v for $d_f/\ell = 0.35$ and $d_v/\ell = 0.05$.

$R_A(f, C_v)$ is plotted in Fig. 4.6 for $d_f/\ell = 0.35$ and $d_v/\ell = 0.05$. The input resistance at resonance varies from 400 Ω when $C_v = 0.5$ pF, to 200 Ω when $C_v = 2.5$ pF. This resistance should not be confused with $1/G_r$, where G_r is the radiation conductance, because the feed is offset from the center of the slot. G_r is actually decreasing as the antenna is tuned to lower frequencies, but the input conductance at d_f is scaled in a frequency dependent way. Although a 2:1 impedance variation does not produce large reflections in itself (one could, for example, operate at 300 Ω), transforming the impedance to 50 Ω over an octave bandwidth is a problem. As with the slot-ring antennas in the previous chapters, however, the antenna is matched using a series reactance at frequencies away from its natural resonance where $R_A(f) = Z_0$. For each combination of (d_f, d_v), the frequency points above and below resonance, f_{01} and f_{02}, respectively, are found where $R_A(f) = Z_0$. $X_A(f_{01})$ is positive, and $X_A(f_{02})$ is negative. Therefore, $f_0 = f_{01}$ is chosen for capacitive matching and $f_0 = f_{02}$ is chosen for inductive matching. Inductive matching is described in the rest of this section, but the same methodology can be used for capacitive matching.

Once f_0 is known, the inductance, $L_m(C_v)$, required to cancel $X_A(f_0)$ is calculated

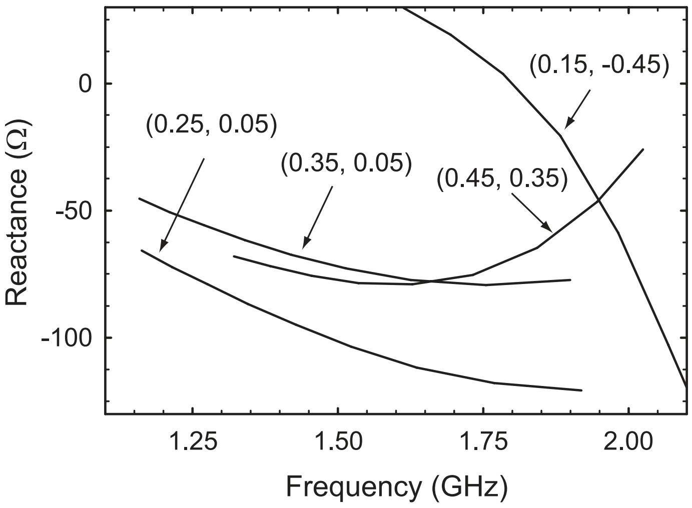

Figure 4.7: $X_A(f_0)$ for various combinations of $(d_f/\ell, d_v/\ell)$.

for each tuning state. If $L_m(C_v)$ is constant, the antenna can be matched perfectly over the whole tuning range. In general, L_m varies with C_v, and therefore, the average value over the tuning range is chosen. Finally, the return loss is evaluated over the tuning range for each (d_f, d_v), and the combinations that meet the requirement Γ_{max} are returned.

This method was applied to the CBS antenna with the dimensions specified in Table. 4.1. The varactor diode was the M/A-Com MA46H071 (0.45–2.5 pF, 0.9 Ω series resistance), and the return-loss threshold, $|\Gamma_{max}|$, was set to -20 dB. A series inductance, $L_v = 0.4$ nH, was added to the varactor in anticipation that it would be connected to the slot through two 0.25-mm via holes [44]. $X_A(f_0)$ is plotted for four combinations of (d_f/ℓ,d_v/ℓ) in Fig. 4.7. Two satisfactory solutions were found and are given in Table. 4.2, and the return loss of solution 1 is plotted in Fig. 4.8.

Realization of the prototype

Two combinations of feed and loading positions have been found for which the tunable shallow CBS antenna is impedance matched over the whole tuning range

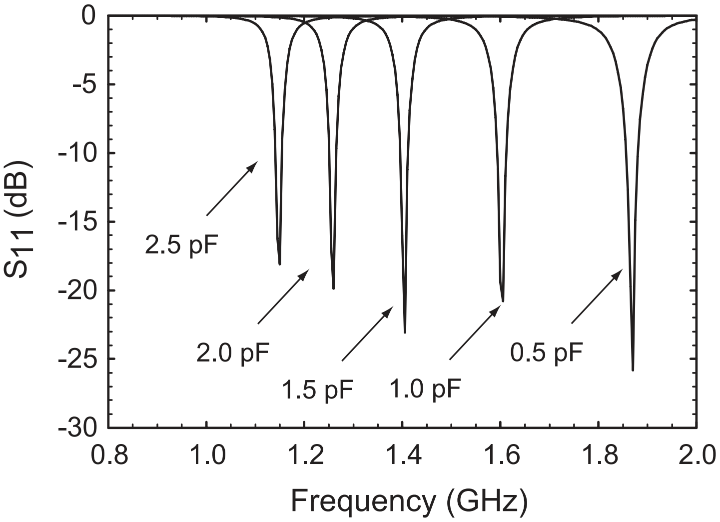

Figure 4.8: Simulated return loss for Solution 1 (Table 4.2) of the tunable CBS antenna.

Table 4.2: Combinations of (d_f, d_v) that allow better than 20 dB return loss over the tuning range of the varactor.

Solution	d_f (mm)	d_v (mm)	L_m (nH)
1	$0.35\ell = 20.8$	$0.05\ell = 3.0$	7.1
2	$0.25\ell = 14.8$	$0.05\ell = 3.0$	10.2

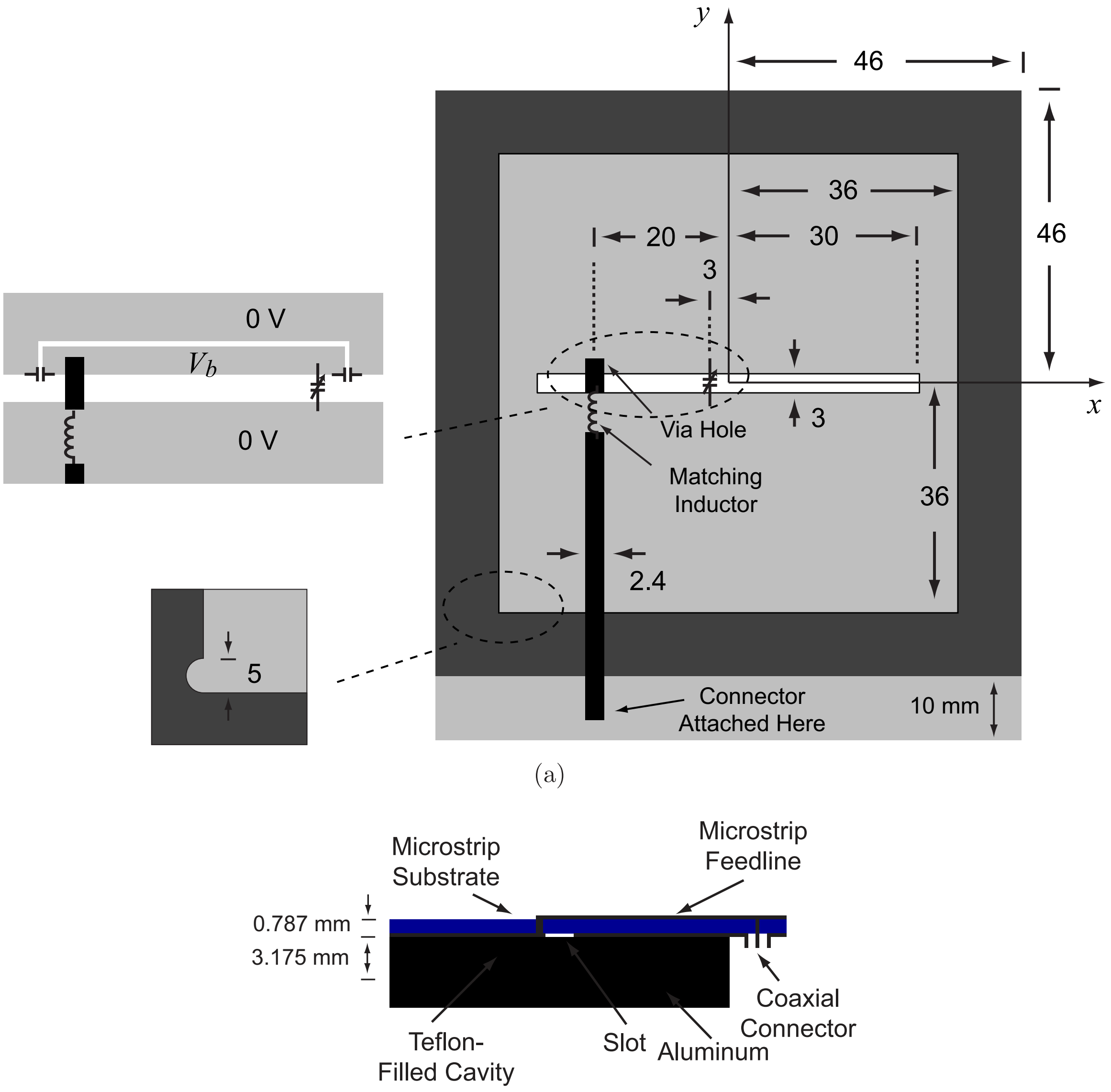

(a)

(b)

Figure 4.9: (a) Top and (b) cross sectional view of the shallow cavity backed slot prototype. All dimensions are in millimeters.

of the varactor diode. A prototype based on Solution 1 has been realized, and the geometry is shown in Fig. 4.9. A cavity with dimensions $L_c \times W_c \times h_c$ is machined into a block of aluminum, and a PTFE ($\epsilon_r = 2.1$) card is cut to fit inside the cavity. There are two minor differences between this cavity and the one in the previous section: first, there are small air-filled cutouts due to the machining process, and second the dielectric constant is 2.1 instead of 2.2. These are expected to have only a minor effect on the impedance characteristics.

The slot is etched on the bottom of a 0.787-mm-thick Rogers 5880 ($\epsilon_r = 2.2$) substrate, which is screwed onto the cavity by eight screws. The feed at d_f is achieved by crossing the slot perpendicularly with a microstrip line and short-circuiting it directly to the slot edge on the far side with a via hole. Inductive matching is achieved by placing a 7.5-nH surface-mount inductor (Coilcraft 0603CS-7N5XJL) [45] in series with the microstrip line just before it crosses the slot. The microstrip substrate continues slightly beyond the cavity on one side so that a PC-mount SMA connector can be attached from below—minimizing the interaction with the feed cable and enabling conformal mounting of the antenna.

Normally, the varactor diode is connected directly across the slot, but the slot is on the bottom of the top substrate and the cavity is filled with dielectric. Instead, the varactor is mounted on the top, and is connected to the slot edges through via holes. Varactor biasing is achieved by cutting a 150 μm strip in the top of the cavity to create a small area that is connected to both the RF line and the cathode of the varactor diode, but is isolated from the rest of the cavity. These gaps are then RF-short-circuited along the slot edge by 22 pF capacitors (AVX ACCU-P, 0603) [46]. The bias voltage is applied to the RF line, through a bias tee. There is no appreciable DC resistance between the RF port and the cathode of the varactor diode, and therefore, a 1 kΩ resistor was placed on the source during measurements. Although not important for this demonstration, this resistance value is a critical parameter in the tuning speed of the antenna.

Two environments in which this antenna may operate are freespace and conformally mounted to a large conducting surface. The second case was tested by mounting the antenna at the center of a 1.2 × 1.2 m^2 conducting plane made of aluminum foil, which was constructed as follows. A piece of plywood was cut to 1.2 × 1.2 m^2, and a hole was cut in the center for the cavity. The plywood was laminated with aluminum foil, and all of the seams were short-circuited with conductive-adhesive-backed copper tape. A piece of copper foil (thickness = 0.25 mm) then connected the antenna to the ground plane. The shape of the cavity was cut out of the center, and it was placed between the cavity and the conducting plane containing the slot.

4.2.2 Results and Discussion

Impedance

The impedance of the antenna was measured with an Agilent E5071B network analyzer for both the free-standing and conformally mounted cases for bias voltages between 0 and 20 V. The free-standing condition was achieved by placing the antenna on a foam block about 1 m from any scatterers. The measured return loss of the two cases is compared in Fig. 4.10. There is almost no difference between the two cases, suggesting that this antenna is not sensitive to the substrate size. This is most likely the case because the susceptance of the cavity is large compared to the susceptance of the radiating side, and is consistent with the results in [47]. This also suggests that the antenna is not sensitive to objects placed near it.

Before it was mounted on the antenna, the impedance of the varactor diode was measured versus frequency using and Agilent E4491A impedance analyzer for bias voltages $V_b = \{0, 1, 2, 4, 8, 20\}$, and the effective series capacitance, C_v, and quality factor, Q_v, are plotted in Fig. 4.11. C_v varies from 0.45 pF at 2 GHz and 20 V to

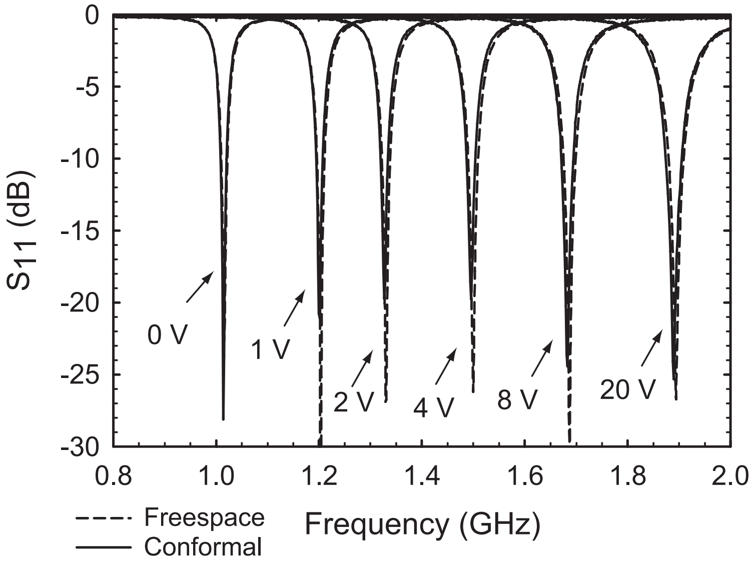

Figure 4.10: Measured return loss for both the free-standing and conformally mounted cases.

2.7 pF at 1 GHz and 0 V. The S-parameters were re-simulated using the measured impedance of both the varactor and the matching inductor, and using the correct dielectric constant for the cavity. The results are compared with the measured data in Fig. 4.12. It is clear that the simulation method presented in the previous section is not effective in predicting the resonance frequency, although in this case it led to a solution that is more desirable than predicted. Although the simulation does not physically include the SMA-microstrip transition, microstrip line, biasing gap, or RF-shorting capacitors—full-wave simulations containing all of these factors did not give physically reasonable results—the two most likely causes of the error are coupling from the cavity to the biasing gap and an error in the simulation.

The 10-dB impedance bandwidth B_{10dB} varies from 1 to 2 percent as the antenna is tuned from 1 to 1.9 GHz (Fig. 4.13). The reduction in bandwidth as the antenna is capacitively loaded is consistent with slot antennas in the literature. For a well matched resonant circuit, the 3-dB bandwidth is related to the quality factor as $2\pi B_{3dB} = 1/Q$. The quality factors of the free-standing and conformally mounted

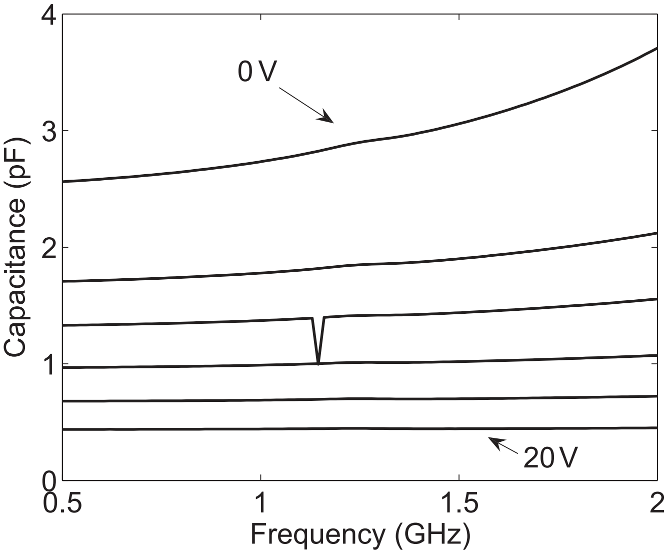

(a)

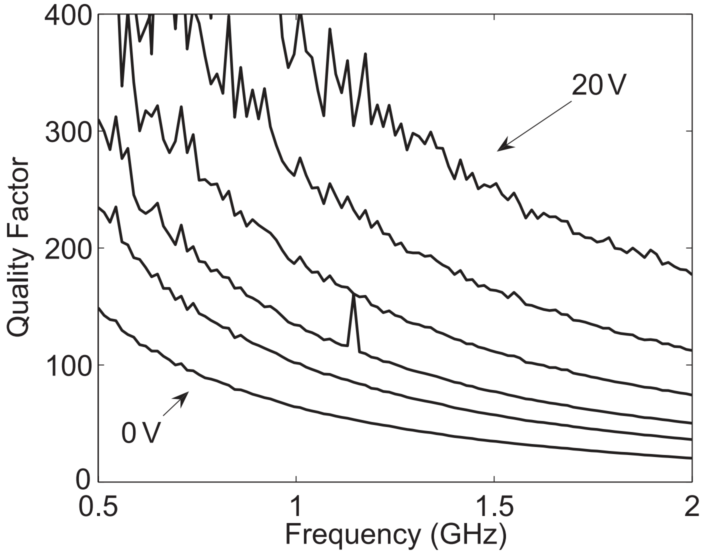

(b)

Figure 4.11: Measured (a) series capacitance, C_v, and (b) quality factor, Q_v of the varactor diode.

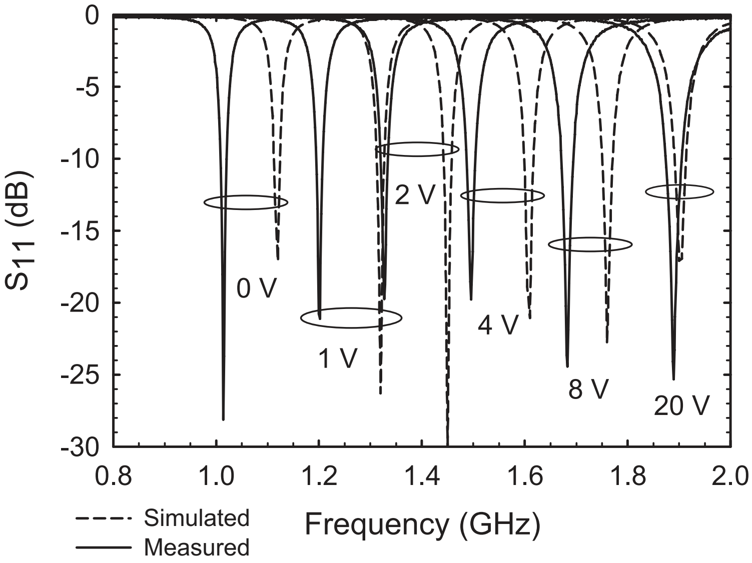

Figure 4.12: Comparison of the measured and simulated return loss.

antennas are nearly the same, as shown in Fig. 4.14. The conformally-mounted antenna has slightly higher Q, and this is not surprising because it cannot radiate to the back side, and therefore, should have a slightly lower radiation conductance. The difference in Q, however, is not significant. The variation of the radiation Q of a lossless tunable CBS with frequency is more severe than $1/f^3$ [48], but the measured total Q of the antenna varies more gently due to loss.

Radiation patterns and efficiency

The radiation patterns of the antenna in an infinite ground plane (including the circuit models of the varactor and matching inductor) were simulated in IE3D. The radiation pattern of the prototype was measured in a Satimo Stargate32 spherical near-field pattern measurement system [27], and the configuration is shown in Fig. 4.15. The antenna antenna rotates in azimuth as the near-fields are measured in elevation by an array of dual-polarized probes. The far-field pattern is then computed by a Fourier transform, and the efficiency (accurate to within ±0.8 dB) is calculated

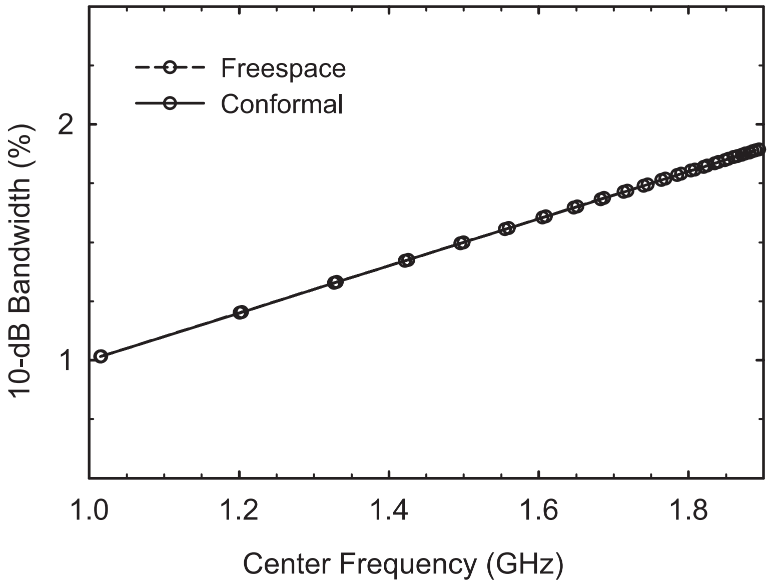

Figure 4.13: Measured 10-dB bandwidth of both the free-standing and conformally-mounted cases.

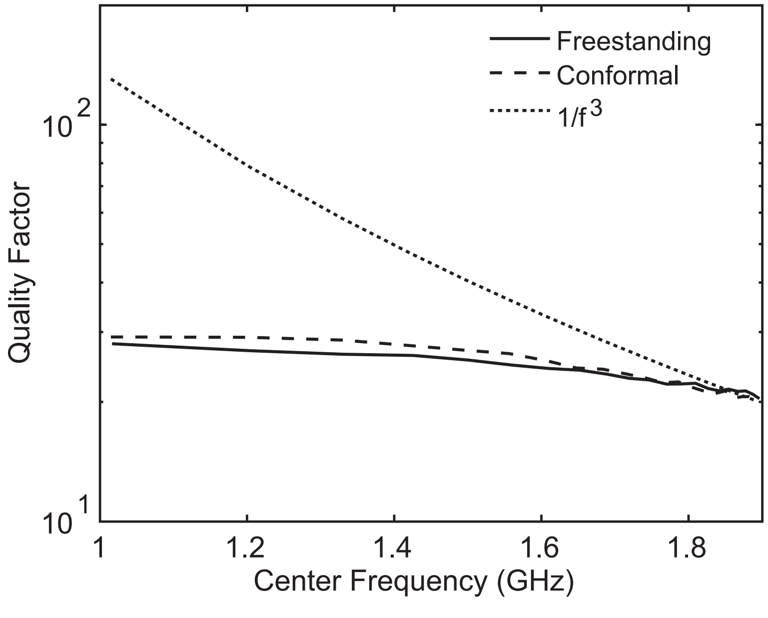

Figure 4.14: Measured Q of both the free-standing and conformally-mounted cases compared with the $1/f^3$ variation assumption.

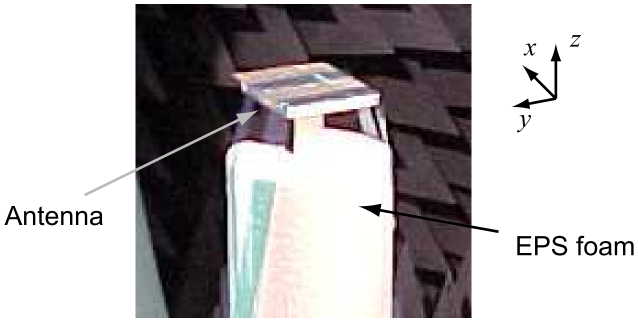

Figure 4.15: The antenna was placed on a rotating foam cylinder for the pattern measurement.

by averaging the gain over the sphere. The bias voltage was applied to the RF cable from outside the chamber, which required re-arranging the cables and attenuators. Unfortunately, time did not allow for a re-calibration of the system, and therefore, the potential error in the measured gain is significant.

The simulated radiation pattern at 1.8 GHz of the antenna placed in an infinite ground plane is plotted in Fig. 4.16. The pattern is constant in the E-plane, and has nulls in the H-plane in the plane of the antenna. The radiation patterns at other frequencies are nearly the same because the slot is smaller than $\lambda/2$ and in its first resonance. The measured radiation patterns of free-standing antenna (as in Fig. 4.15) are shown in Fig. 4.17 for 1.0, 1.5, and 1.9 GHz (0, 4, and 20 V bias, respectively). The patterns have nearly symmetric E- and H-plane patterns, and are linearly polarized with cross-polarization levels of <-25 dB. The front-to-back ratio is as low as 5 dB for 1.0 GHz, and as high as 13 dB at 1.5 GHz. Both the symmetric E- and H-plane patterns and the low front-to-back ratio occur because the antenna is less than one wavelength in dimension at the highest frequency. It was shown that the input impedance is relatively insensitive to the ground plane size, and therefore, lower front-to-back ratio can be achieved by simply increasing the ground-plane size and/or shape.

The measured gain and efficiency vary from -2 to 5 dB and 18 to 76%, respectively,

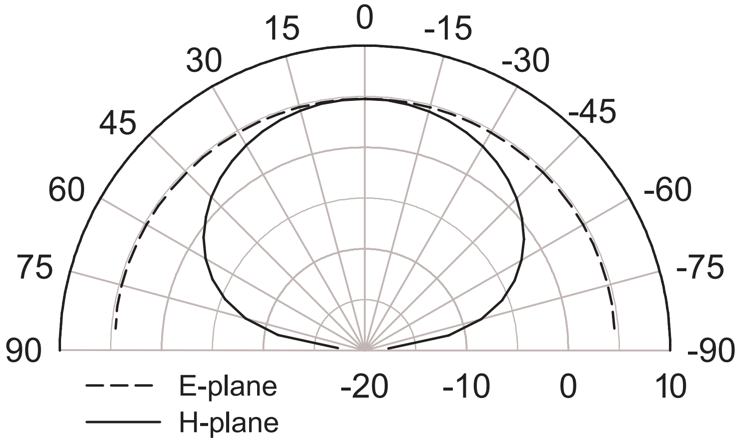

Figure 4.16: Simulated antenna-gain pattern (in dBi) of the tunable CBS antenna at 1.8 GHz when $C_v = 0.5$ pF (infinite ground plane).

over the 1.0–1.9 GHz range (Fig. 4.18). As mentioned previously, however, there is up to 0.8 dB uncertainty in the measurement. The main contribution to the loss at low frequencies is the varactor diode. Other contributions to the loss, which may become dominant at higher frequencies, are the use of aluminum for the cavity, resistance in the interface between the top substrate and the cavity—to which force is applied by 8 screws—the finite Q of the RF-short-circuiting capacitors across the bias gap, and losses in the SMA connector (≈0.2 dB based on a measured test structure). The simulated gain is 5 dB at 1.8 GHz, and is greater than 0 dB down to 1.3 GHz. The simulated efficiency has a much steeper slope than the measured efficiency; it is again apparent that this simulation method is sufficient for finding feed and loading locations for the shallow CBS, but is not satisfactory for predicting the resonance frequency and efficiency.

Power handling

The varactor diode is a non-linear device, and therefore, its capacitance depends not only on the bias voltage, but also on the RF voltage across it. As the power

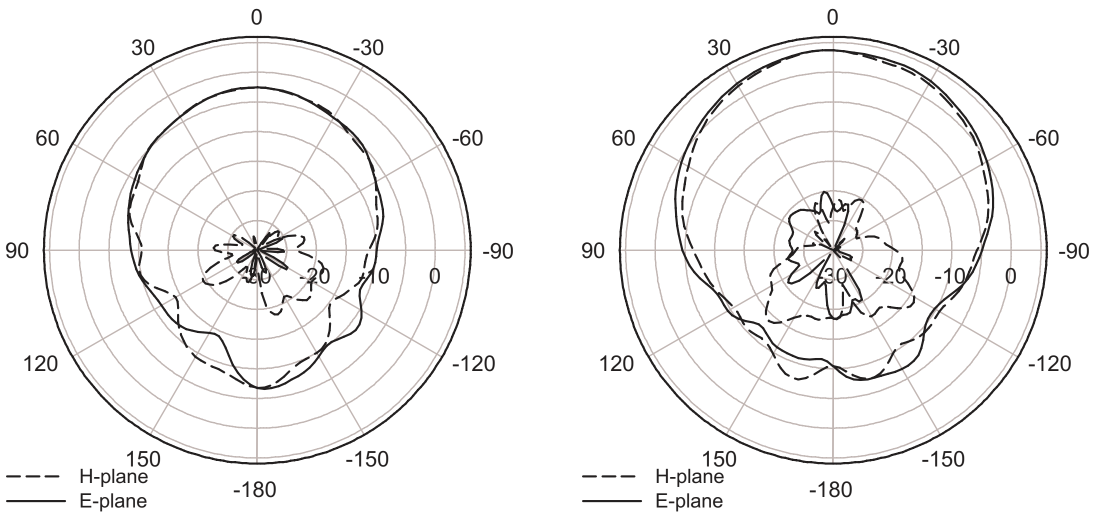

(a) 1.0 GHz, $V_b = 0$ V (b) 1.5 GHz, $V_b = 4$ V

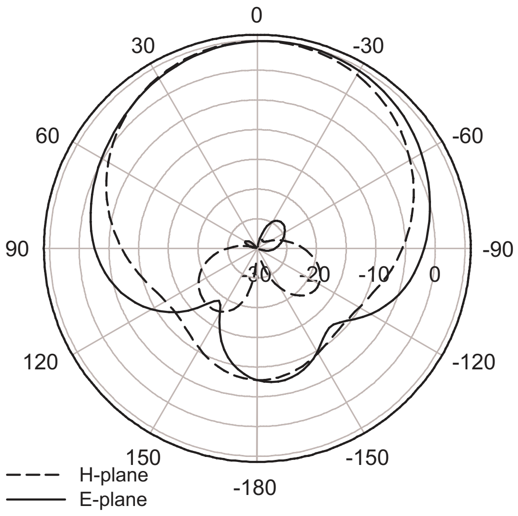

(c) 1.9 GHz, $V_b = 20$ V

Figure 4.17: Measured antenna-gain patterns (in dBi) over the tuning range of the tunable CBS antenna (finite ground plane).

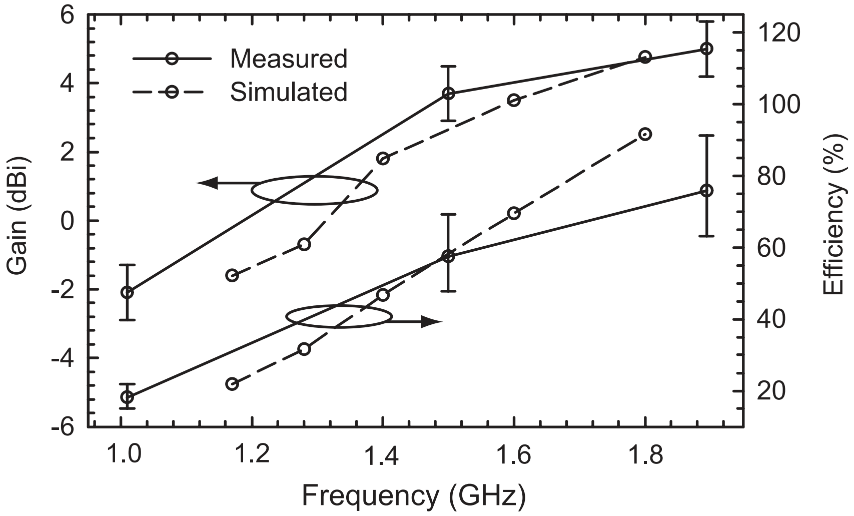

Figure 4.18: Measured and simulated antenna gain and total efficiency.

incident upon the antenna increases, two things occur that degrade the performance of the antenna: first, the effective capacitance increases—which reduces resonance frequency, as in Fig. 2.18 for the slot-ring antenna—because the capacitance versus voltage curve is steeper at lower frequencies, and second, some of the power is converted to harmonics of the signal. The input 1-dB-compression point, P_{1dB}, was measured using the setup in Fig. 2.16, and varies from -10 dBm at 1 GHz to 10 dBm at 1.9 GHz (Fig. 4.19). P_{1dB} is lower at lower frequencies (lower bias voltages) because the capacitance varies most rapidly with voltage at 0 V, and because the Q, and therefore the RF voltage across the varactor, is higher at lower frequencies. With P_{1dB} values in this range, the varactor-tuned CBS is most suited for receive applications.

4.3 Miniaturization of the Varactor-Tuned CBS

Although the CBS antenna presented in the previous section has excellent tuning performance, it is 9 × 10 cm^2, making it too large for many mobile communication devices. A method to reduce the size of the CBS antenna in one dimension has

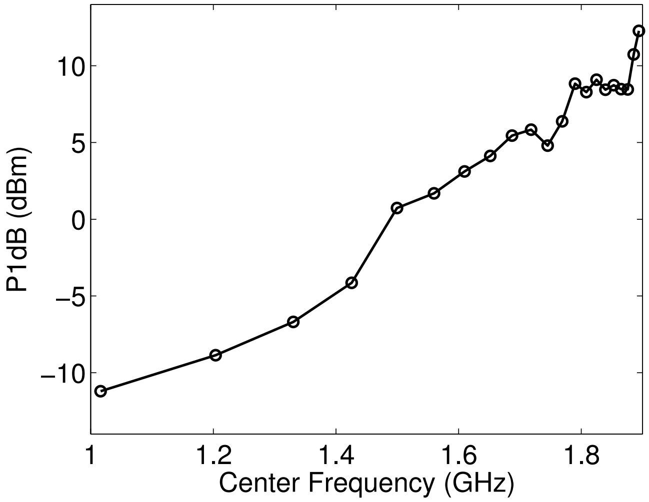

Figure 4.19: Measured input 1-dB compression point.

been developed; replacing top of the cavity with meandered strips makes it appear electrically longer than its physical length, and the antenna is matched with an off-set microstrip feed (which is also meandered) [49]. In this section, varactor-tuned miniaturized cavity-backed slot antennas are investigated. First, the calculation of the bandwidth and varactor efficiency are discussed, and second, three varactor-tuned miniaturized CBS-antenna designs are compared in light of tuning range, efficiency, and bandwidth.

4.3.1 Efficiency and Bandwidth

The bandwidth and efficiency will be studied assuming that the slot is center-fed and center-loaded in order to simplify the analysis. In the general case, the admittances are scaled in a frequency dependent way as the feed and loading varactor are offset from the center.

Efficiency

Consider the CBS geometry in Fig. 4.1, with d_f and d_v set to zero. In this case, the antenna is also symmetric about the y-z plane, and because we are concerned with making the antenna small, $\ell < \lambda_s/2$. In this case the maximum voltage is at the origin and the unloaded input admittance is given as:

$$Y'_A = G'_A + jB'_A = G_s + j(B_s + B_{cav}), \tag{4.8}$$

where Y_s is the admittance of the slot in the upper half-space, and B_{cav} is the susceptance due to the cavity. The loaded input admittance is

$$Y_A = G'_A + G_v + j(B'_A + B_v), \tag{4.9}$$

where (if $Q_v \gg 1$)

$$\begin{aligned} G_v =& \omega^2 C_v^2 R_s = B_v/Q_v, & \text{(4.10a)} \\ B_v =& \omega C_v, & \text{(4.10b)} \\ Q_v =& \frac{1}{\omega C_v Rs}, & \text{(4.10c)} \end{aligned}$$

and R_s is the equivalent series resistance of the varactor diode. The varactor efficiency can be expressed as a current divider network:

$$\eta_v = \frac{G_s}{G_s + G_v} = \frac{G_s}{G_s + B_v/Q_v} = \frac{G_s}{G_s + B_v^2 R_s}. \tag{4.11}$$

It is clear from (4.11) that the efficiency decreases as B_v increases, and therefore, starting with an antenna that is already miniaturized (i.e. it already resonates at low frequency, thus requiring less susceptance from the varactor) before applying the varactor increases its efficiency at the high end of the tuning range. However, the behavior of Y_s must be considered over the whole tuning range to understand the tuning performance. Perhaps the most simple example to consider is the small slot ($k_0\ell/2 < 1$); its input admittance can be calculated from the well known impedance for the short dipole through Booker's relation [12]:

$$Y_s \approx \left\{ \frac{1}{180\pi^2} \left(k_0 \frac{\ell}{2} \right)^2 - \frac{j}{30\pi^2} \ln \left(\frac{\ell}{2a} - 1 \right) \cot \left(k_0 \frac{\ell}{2} \right) \right\}, \tag{4.12}$$

where $a = w/4$ is the equivalent wire radius. Here, G_s is proportional to k_0^2, which is typical for small antennas, and B_s is given by $Y_{0a} \cot(k_0\ell/2)$, where Y_{0a} is the characteristic admittance of the slot. The admittance of the cavity-backed slot in an infinite ground plane is given by one half of Y_s in (4.12) plus the reactive contribution of the cavity. If there are propagating modes in the cavity, a rough approximation for the characteristic admittance is

$$B'_A \approx -Y_{eff} \cot(p\omega), \tag{4.13}$$

where Y_{eff} is the effective characteristic admittance of the slot and the cavity, and p is a constant. The detailed susceptance is given in [39], and is quite complicated to analyze due to the dispersive nature of waveguides.

As the antenna is miniaturized, the efficiency is degraded if either G_s is reduced, or if the amount of susceptance needed to resonate the antenna increases. The radiating slot should be kept as long as possible to maximize G_s. Although the antenna can be resonated slightly above the tuning range to minimize the amount of susceptance needed from the varactor, this may limit the performance at lower frequencies. Consider the case of dielectric loading: this increases both the characteristic admittance and propagation constant of the resonator(s) in the antenna. If the antenna is resonated with the dielectric, B'_A is small at the top end of the tuning range where the cotangent term is nearly zero. By the time it has been tuned to half of the maximum frequency, however, $B_s \approx -Y_{eff}$. Therefore, an increased dielectric constant leads to a faster degradation in the efficiency over the tuning range. It is expected that a low-loss material with high permeability would lead to better miniaturization of the cavity backed slot in one dimension without a reduction in the efficiency.

Bandwidth

The fractional bandwidth of the antenna is inversely proportional to its resonator Q. For an arbitrary parallel resonator with $Q > 7$:

$$Q \approx \frac{\omega_0}{2G}\frac{\partial B}{\partial \omega}, \tag{4.14}$$

where G and B are the total conductance and susceptance of the resonator. Well below its natural resonance, the antenna can be approximated as an inductor, and the Q reduces to the familiar

$$Q = \frac{B_v}{G} = \frac{B'_A}{G}. \tag{4.15}$$

As with the efficiency, B_v should be minimized and G_s should be maximized for maximal instantaneous bandwidth over the tuning range. Near the natural resonance, the Q is calculated by (4.14), but many factors must be considered due to the dispersion of the waveguide modes.

4.3.2 A Comparison of Three Designs

Three miniaturization methods are compared to investigate the tuning performance of the miniaturized CBS: simply tuning with a varactor diode, loading the cavity with a high dielectric constant, and replacing the top of the cavity with meandered strips, as in [49]. Three identically sized antennas were simulated with gap ports at the center (Fig. 4.20), their input admittance was extracted, and their tuning

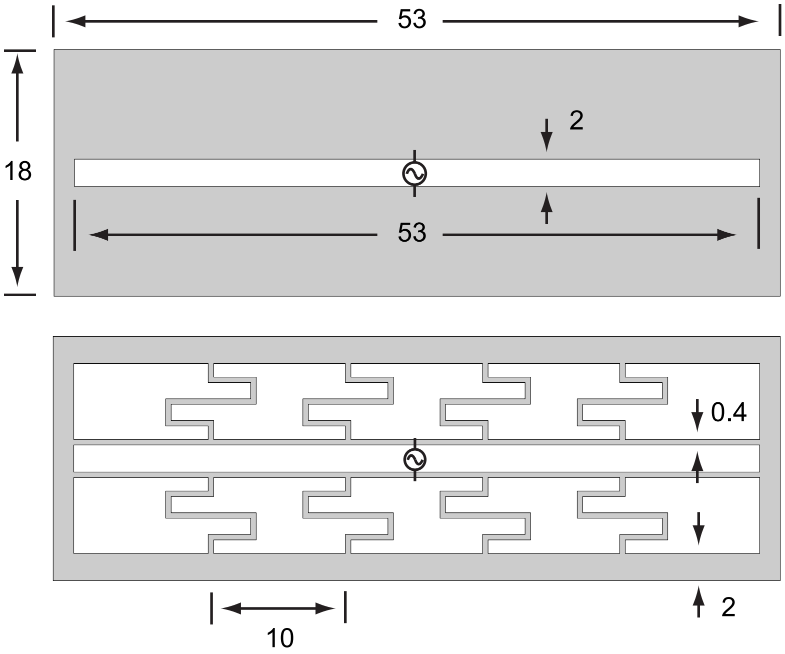

Figure 4.20: Geometry of the miniaturized CBS antennas. (top) the nominal and high-dielectric designs, (bottom) the meandered strip design. The cavities are 6.35 mm deep and all dimensions are in millimeters.

performance is evaluated in this section. The first design, referred to as the Nominal Design, is a simple cavity-backed slot placed at the center of a small ($53 \times 18 \times 6.35$ mm^3) cavity. The cavity is filled with Rogers TMM3 dielectric material ($\epsilon_r = 3.3$, $\tan\delta = 0.002$) [50]. A second design, the ϵ_r-10 design, is exactly the same as the nominal design except that it is filled with $\epsilon_r = 10$ dielectric material. The final design, the Meandered-Strip design, is filled with TMM3, but the top of the cavity is replaced by meandered strips. The details of the three designs are summarized in Table 4.3, where f_{0c} is the unloaded cavity resonance and f_{0s} is the resonance frequency of the a $\ell \times w$ slot on a dielectric half-space. The metal conductivity is assumed to be that of copper in the simulations.

Table 4.3: Details of the three miniaturized CBS antennas. All dimensions are in millimeters and all frequencies are in GHz.

Design	ϵ_r	L_c	W_c	h_c	ℓ	w	f_{0c}	f_{0s}	L_m (nH)
Nominal	3.3	18	56	6.35	50	2	4.8	2.0	28
ϵ_r-10	10.0	18	56	6.35	50	2	2.8	1.3	35
Meandered-strip	3.3	18	56	6.35	50	2	–	2.0	60

Slot admittance

The slot admittances for the three cases are compared in Fig. 4.21. There is a significant difference in the three cases. It was expected that the nominal and ϵ_r-10 cases would have the same slot conductance, but the ϵ_r-10 design has significantly more. This could be explained by dielectric losses because $\tan\delta$ is set to 0.002 for both cases (and the antenna is not scaled), or by the fact that the slot is above its natural resonance. The meandered design has the lowest input conductance. This is perhaps caused by electric fields that oppose the radiating field in the slot. As expected, the nominal design has the most susceptance, and the ϵ_r-10 design has the highest susceptance slope, passing through a resonance at 2.3 GHz. The meandered design has the smallest susceptance over a large range, especially at the lower frequencies.

Impedance match over the tuning range

When a variable capacitance is placed across the slot, changing the resonance frequency, the resonant slot conductance varies approximately as ω_0^2. If the tuning varactor is lossless, this results in a 4:1 admittance variation over a 2:1 tuning range, which would slightly degrade the impedance match if the antenna were matched at resonance over the whole range. However, the input admittance is very small for small antennas, and therefore, an admittance transforming element is needed to

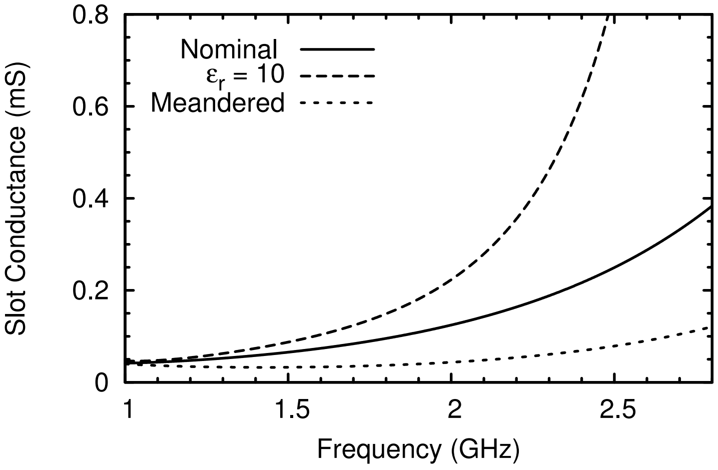

(a) G_s

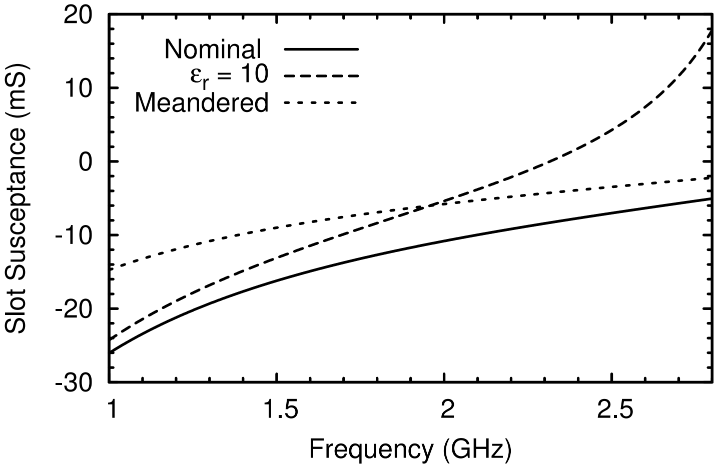

(b) B_s

Figure 4.21: Slot admittance of the three different miniaturized CBS antennas.

operate over a large bandwidth. The J-inverter scales the admittance as

$$Y_{in} = J^2/Y_A, \tag{4.16}$$

where $J = \omega C$ and $J = 1/\omega L$ for capacitive and inductive inverters, respectively [51]. Therefore, a small slot antenna that is tuned with a lossless varactor can be matched perfectly over more than an octave with a capacitive admittance inverter. A simple series capacitor is a good approximation to this, as demonstrated in Chapter 2.

In this analysis, a varactor with a tuning range of 0.5–2.5 pF and $R_s = 0.9$ is assumed. In this case, the total input conductance is a function of both G_s and B_v^2, and may decrease with frequency; therefore, inductive matching is preferred. If a single series inductor is used to approximate an inverter, and the matching condition is:

$$Z_0 = \frac{G_A \omega L}{B_A}. \tag{4.17}$$

It is important to note that this method of matching changes the resonance frequency slightly. Also, the slope of G_s is different for offset feeds due to the frequency dependent impedance scaling along the length of the slot.

Simulated results

Series matching inductors were added to all three antennas, and their values are given in Table 4.3. Although the matching inductors slightly increase the resonance frequency, the following analysis is justified because the observed phenomena are more significant than this change in resonance frequency. Furthermore, some kind of frequency dependent matching is necessary if the antennas are to be used at 50 Ω. Finally, the comparison of the resonance frequencies can simply be made from B_s (Fig. 4.21(b)) and C_v. The reflection coefficient is plotted on the Smith chart in Fig. 4.22, and in dB in Fig. 4.23. It is clear that the input impedance is behaving

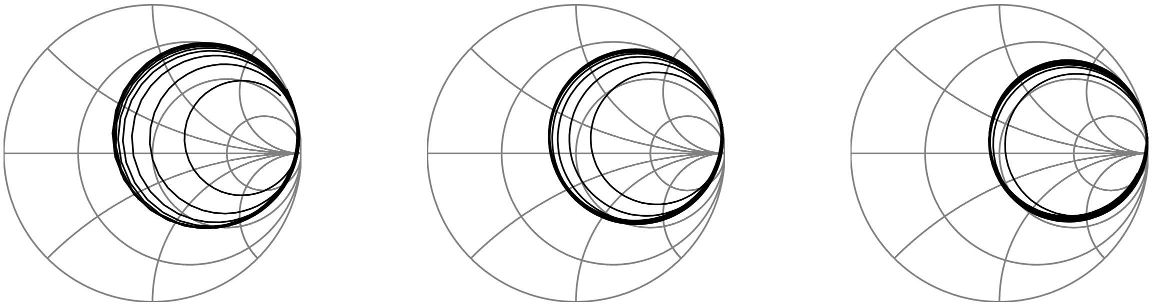
(a) Nominal

(b) ϵ_r-10

(c) Meandered

Figure 4.22: Reflection coefficient of the miniaturized CBS antennas from 1–2.8 GHz as C_v varies from 0–2.5 pF and $R_s = 0.9\ \Omega$.

as a series resonance, and therefore, that L_m is indeed acting as an inverter. All three antennas are matched over a significant tuning range, and as predicted from the slot-admittance, the meandered-strip antenna has the largest tuning range (Fig. 4.24).

The varactor efficiency and Q were calculated using (4.11) and (4.14), respectively, and are plotted in Fig. 4.25. The varactor efficiency is severely degraded over the tuning range. For the nominal design, it varies from -1 dB at 2.6 GHz down to -10 dB at 1.4 GHz. The varactor efficiency of the ϵ_r-10 antenna is the highest above 1.4 GHz due to its larger radiation conductance, but below 1.4 GHz, the meandered-strip antenna is the most efficient. Although it has the lowest slot conductance, the meandered-strip antenna has much less susceptance than the other designs at lower frequencies. It should be noted that any conductor and dielectric losses will degrade the efficiency further. The Q of the antenna is calculated from (4.14), and is the reciprocal of the bandwidth of the antenna if the feeding admittance is included in G. The nominal design has the lowest Q, due to its moderate susceptance slope and slot conductance. The meandered-strip design has the highest Q, which can be plainly seen in Fig. 4.23, because of its small slot conductance.

In summary, varactor-diode tuning of two miniaturized CBS antennas—one with

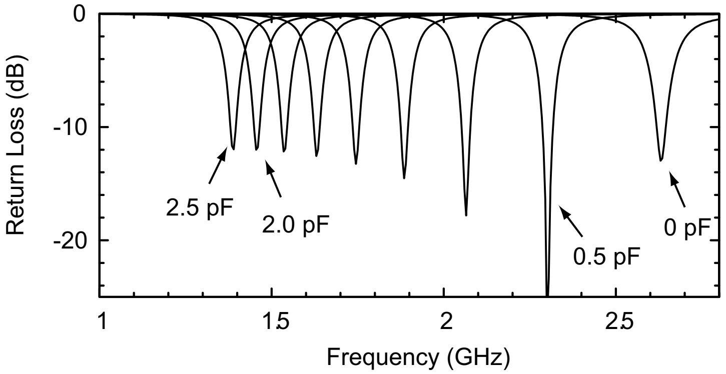

(a) Nominal

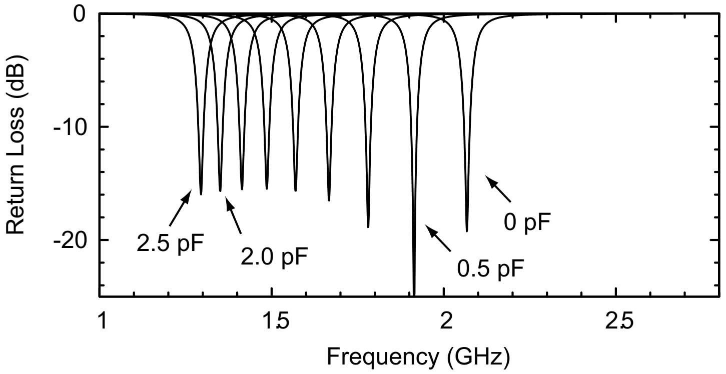

(b) ϵ_r-10

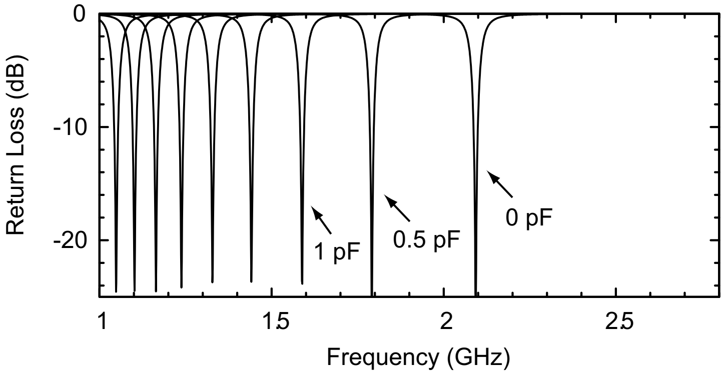

(c) Meandered

Figure 4.23: Return loss of the miniaturized CBS antennas as C_v varies from 0–2.5 pF and $R_s = 0.9\ \Omega$.

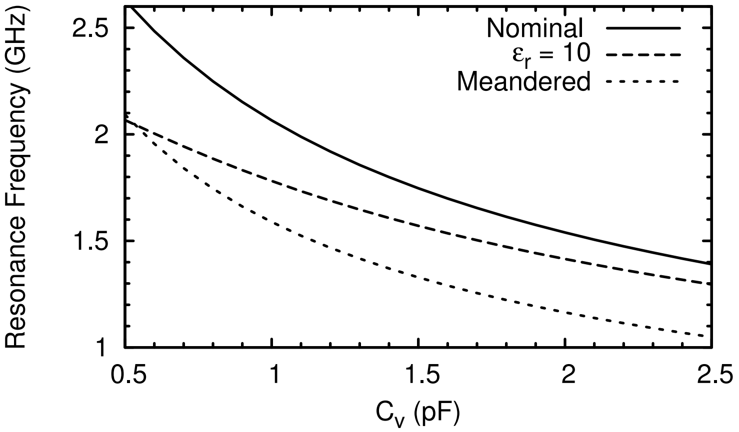

Figure 4.24: Center frequency of the miniaturized CBS antennas as a function of the loading capacitance.

a higher dielectric constant, and one where the top of the cavity has been replaced by meandered strips—have been compared with the nominal design. Simulations show that all three center-fed antennas are matched to 50 Ω over at least a 1.6:1 frequency range by placing an inductor in series with the antenna. The higher dielectric constant provides higher efficiency versus frequency, but limits the tuning range. The meandered strips reduce the reactance slope, achieving the highest level of miniaturization and the largest tuning range, but the low slot conductance of the meandered-strip antenna degrades both its efficiency and bandwidth.

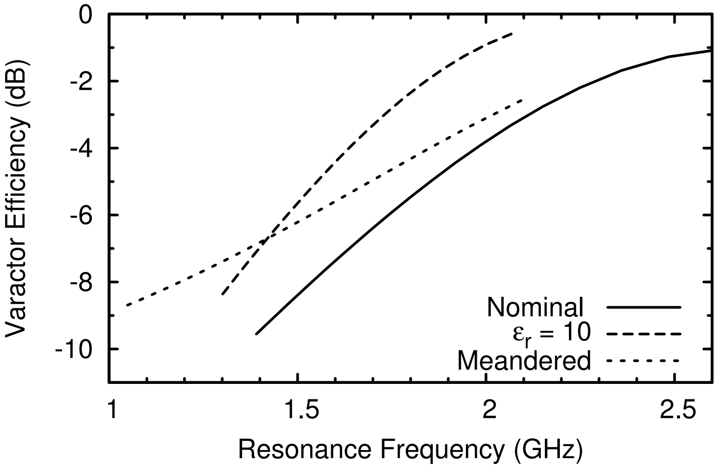

(a)

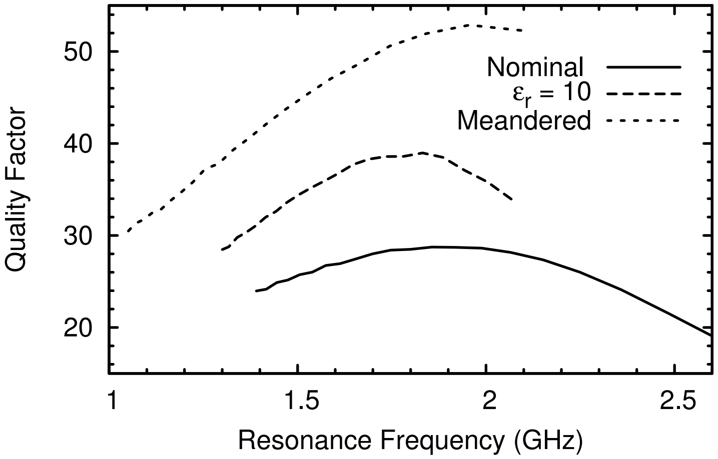

(b)

Figure 4.25: Varactor efficiency and Q over the tuning range of the miniaturized CBS antennas when $R_s = 0.9\ \Omega$. C_v is varying from 0–2.5 pF.

Chapter 5

A Dual-Polarized Tunable Cavity-Backed Patch Antenna with Independent Tuning

A dual-polarized tunable antenna with double-sided radiation was presented in Chapter 3, where both polarizations are independently tunable over a 1.7:1 bandwidth. Single-sided radiation is necessary for most wireless applications, however, because the antenna must be mounted on or near a scattering surface. The square microstrip patch antenna is a good candidate for a dual-polarized tunable antenna with single-sided radiation. Frequency agility [1, 11, 52, 53] and dual-polarized operation [16] have been studied in detail, but a literature search produces few dual-polarized antennas with independent tuning. In this chapter, the operation of the tunable patch antenna is reviewed, and a dual-polarized cavity-backed patch antenna with differential probe-feeds is presented that tunes over a 1.7:1 bandwidth with varactor diodes. To the author's knowledge, this is the first dual-polarized antenna with independent tuning over a 1.7:1 bandwidth and single-sided radiation.

5.1 Patch Antenna Overview

The microstrip patch antenna has been studied extensively in the literature [54],[55] and is one of the most convenient antennas for integration with planar printed circuits. It is a narrowband antenna that consists of a resonant patch of metal placed a small distance ($< \lambda_0/10$) above a ground plane as shown in Fig. 5.1(a). It is usually rectangular in shape and operated in its first resonance, which occurs when its length is slightly less than half of the guided wavelength. Its resonant modes are often approximated by assuming that the it is a rectangular cavity with Perfect Electric Conducting (PEC) top and bottom walls and Perfect Magnetic Conducting (PMC) side walls [56]. The fundamental $\hat{x}$-polarized mode, the TM^z_{100} mode, has 2 planes of symmetry; the x-z plane is a PMC symmetry plane, and the y-z plane is a PEC symmetry plane. The radiation is $\hat{x}$-polarized and primarily occurs because the $\hat{x}$ component of the fringing electric fields at edges a and b are in phase, and therefore, add constructively in the far field [57]. Because of this, the radiation is usually analyzed as slots radiating into a half-space. The $\hat{y}$ component of the fringing field at edges c and d is odd with respect to both the x-z and y-z planes, and therefore, does not radiate in either of these planes. Radiation from these edges is often neglected.

The microstrip patch antenna is almost always printed on a grounded dielectric slab, and therefore, couples to the TM_0 substrate mode. The bandwidth of the patch increases as the substrate height increases, but the coupling to the TM_0 mode also increases, reducing the efficiency. If the patch is to be used as an array element, the TM_0 mode increases the mutual coupling between elements and can lead to scan blindness [58]. The cavity-backed patch [59–61] (Fig. 5.1(b)) is very similar to the microstrip patch, but the ground plane is at the same level as the patch (or even above it) instead of below. The cavity-backed patch is not printed on a grounded dielectric slab, and therefore, has less mutual coupling in an array setting than the microstrip patch [59]. Furthermore, if the patch and ground plane are in the same plane (which is very convenient for a varactor-tuned antenna), the radiation and impedance characteristics are very similar to those of the microstrip patch [61]; if the cavity/substrate is thin, the radiating slots are the same as the *equivalent* radiating slots of the microstrip patch antenna, and the fringing fields at the edges have only a minor effect on the characteristic admittance of the fundamental microstrip mode.

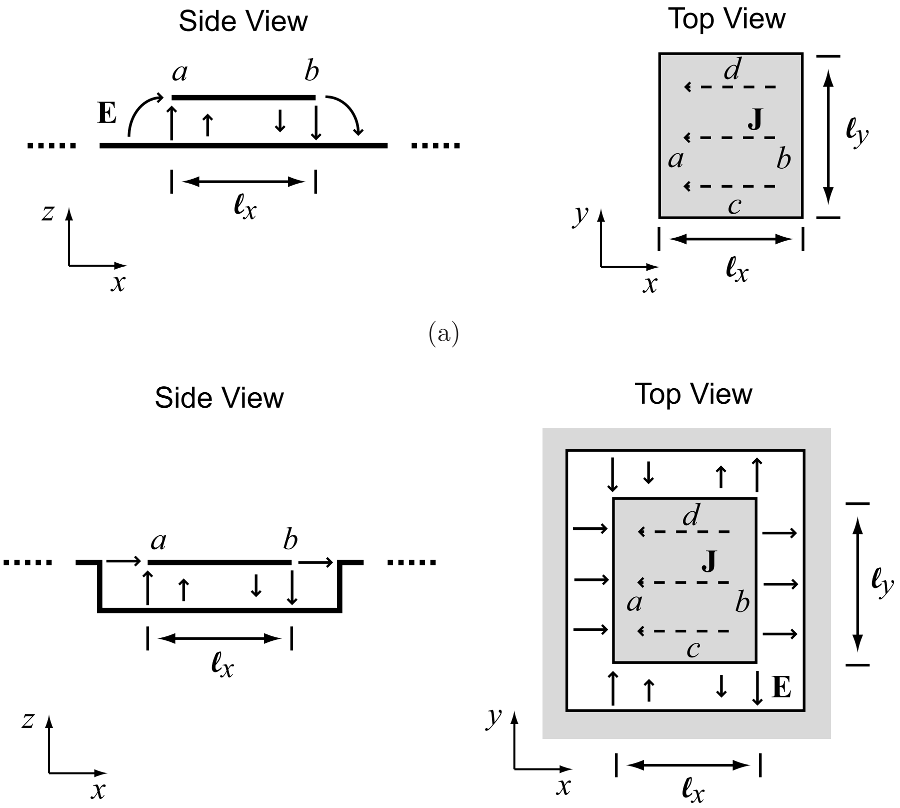

(a)

(b)

Figure 5.1: Typical geometries and field distributions of the fundamental $\hat{x}$-polarized mode, Ψ_x, of the (a) microstrip and (b) cavity-backed patch geometries.

5.1.1 Dual-Polarized Patch Antenna Feeds

The TM_{100}^{z} mode, shown in Fig. 5.1(a), can be excited at any point that is not in the y-z plane, which is a short circuit for the TM_{100}^{z} mode. Some common feeding methods for the microstrip patch are a coaxial probe, a microstrip line connected to the edge of the patch, and an aperture in the ground plane below the patch [62]. The cavity-backed patch is usually probe-fed, although aperture and Coplanar Waveguide (CPW) feeds should be possible. The input impedance is generally much higher than 50 Ω at the patch edges, but can be reduced by moving the feed closer to the center.

The rectangular microstrip patch antenna has another fundamental mode, the TM_{010}^{z} mode, which occurs when $\ell_y \approx \lambda_g/2$ and is $\hat{y}$-polarized. If the patch is square ($\ell_x = \ell_y$), the TM_{100}^{z} and TM_{010}^{z} modes occur at the same frequency and have the same Quality Factor (Q) and radiation pattern (rotated 90° about the z axis from each other). Dual polarized operation is achieved by placing the x-polarized feed along the x-z plane (where the TM_{010}^{z} mode is short-circuited), and the y-polarized feed in the y-z plane (where TM_{100}^{z} mode is short-circuited).

5.1.2 Frequency-Agile Microstrip Patch Antennas

Frequency agility has been implemented in the microstrip patch antenna in several ways, using either switches or varactor diodes. Shaubert et al. placed shorting pins under the patch at varying locations, changing the operating frequency over a 1.5:1 range [52]. In this scheme, a number of switches can be place under the antenna to reconfigure not only the operating frequency, but also the polarization characteristics. Sheta and Mahmoud demonstrated a compact antenna that switches between four bands in a 1.85:1 frequency range using this method [63]. Dual-band reconfigurability has been achieved by re-routing the current with the use of switched slots in the patch [64], and an antenna containing multiple such slots has been demonstrated

Figure 5.2: Side view of the probe-fed microstrip patch antenna with tuning varactors at the radiating edges, as in [1].

that switches between several bands over a 2:1 frequency range [65]. Finally, sections of the patch can be switched in or out, operating at bands as different as L-band and X-band [66].

A patch antenna with a 1.35:1 tuning range was first presented by Bhartia and Bahl [1]. The resonance frequency is reduced by placing shunt varactors at the radiating slots, as in Fig. 5.2. Since then, tuning ranges of 1.6:1 [9, 10] and 1.85:1 [11] have been reported using the same method. Tuning has also been demonstrated over a 1.5:1 range by putting the varactors in series with the patch, although the impedance match seems to have been an issue [53]. The efficiency of varactor-tuned antennas is reduced as they are tuned to lower frequencies [67], and the antenna gain over the tuning range has been improved by placing multiple varactor diodes with small capacitance, which have a higher Q than a single diode with the same capacitance, at the radiating edges [68].

5.2 Design of the Dual-Polarized Tunable Antenna

5.2.1 Conditions for Dual-Polarized Independent Tuning

It was shown for the slot-ring antenna in Chapter 3 that dual-polarized independent tuning with high isolation can be achieved under the following conditions:

1. The antenna has two planes of symmetry.
2. The modes responsible for the two polarizations are orthogonal due to their even-odd symmetry with respect to the two symmetry planes (e.g. mode Ψ_1 has PEC^{yz} and PMC^{xz} symmetries, and mode Ψ_2 has PMC^{yz} and PEC^{xz} sym-

metries, where PEC^{xz} symmetry means that the x-z plane is a PEC symmetry plane).

3. The antenna feeds for Ψ_1 and Ψ_2 have the same symmetry as Ψ_1 and Ψ_2, respectively. The simplest case is when the feed for Ψ_1 is in the PEC symmetry plane of Ψ_2, and vice versa for the feed of Ψ_2.

4. The tuning elements for Ψ_1 are in the PEC symmetry plane of Ψ_2 and vice versa.

Although the slot-ring antenna in Chapter 3 does not truly have two symmetry planes, this symmetry is approximated through the use of microstrip reactive loads. For the patch antenna, however, the PEC symmetry planes are commonly enforced by using differential (antisymmetric) probe-feeds [69],[70].

If the patch antenna is fed in a single-ended manner, the feed couples to higher-order modes that then couple to the feed of the orthogonal polarization. Furthermore, coupling to higher-order modes increases the cross-polarized radiation. If fed differentially, however, the patch antenna satisfies all of the above conditions. When the patch is not loaded, Condition 2 is satisfied by the TM^z_{100} and TM^z_{010} modes. As tuning elements change the resonance frequencies and mode distributions, orthogonality—and therefore, port-to-port isolation—is preserved due to the even-odd symmetry of the modes.

The resonance frequency of Ψ_1, f_{01}, can be tuned without changing the resonance frequency of Ψ_2, f_{02}, if the tuning elements for Ψ_1 are placed in the PEC symmetry plane of Ψ_2 because they are short circuited from the perspective of Ψ_2. In the same manner, f_{02}, can be tuned without changing f_{01}.

5.2.2 Antenna Geometry

The geometry of the dual-polarized tunable cavity backed patch antenna is shown in Fig. 5.3. The patch is 84 × 84 mm^2, and the horizontal and vertical polarizations ($\hat{h}$-pol and $\hat{v}$-pol, respectively) are fed by differential probe-feeds at ports 1 and 2, respectively, where each probe is connected to an SMA connector soldered to the bottom of the cavity. The four probes are placed 16 mm from the center along the x and y axes. A square gap with inner and outer widths of 3.5 and 4.7 mm, respectively, surrounds the probe feeds. This type of gap was used by Hall [71] to compensate for the probe-feed inductance in thick substrates. In this work, however, it allows the antenna to be impedance matched over the entire tuning range by placing surface-mount 5.8-nH lumped inductors (Coilcraft 0603CS-5N6X_L [45], 5.8 nH at 900 MHz) in series with the antenna at each feed while directly connecting the coaxial feed to the patch.

The cavity is $100 \times 100 \times 6.35$ mm^3, and is filled with Rogers 5880 ($\epsilon_r = 2.2$, $\tan\delta = 0.0009$) [50] dielectric material. The sidewalls of the cavity wrap around to the top producing a 2-mm-wide ring of metal which aids in the fabrication. It can also be used to conformally mount the antenna to a ground plane. This leaves a 6-mm-wide slot surrounding the patch.

Varactor diodes C_{11} and C_{12} are placed across the radiating slots along the x axis and tune the $\hat{h}$-pol; C_{21} and C_{22} are placed along the y-axis and tune the $\hat{v}$-pol. Pads are extended from both the patch and the cavity walls to mount the varactor diodes; the pads are 2 mm wide and the gap across which the diodes are mounted is 1 mm wide. The diodes are Skyworks SMV1405-074 silicon abrupt-junction common-cathode pairs [72] that are connected in parallel to achieve a capacitance range of $\approx$ 1.2–5.4 pF from 0–30 V with an equivalent series resistance (ESR) of $\approx 0.55\ \Omega$. This configuration was chosen because it resulted in a higher varactor Q than using a single diode with higher junction capacitance, which is consistent with [68].

The varactor diodes are reverse biased by applying a DC voltage to the patch

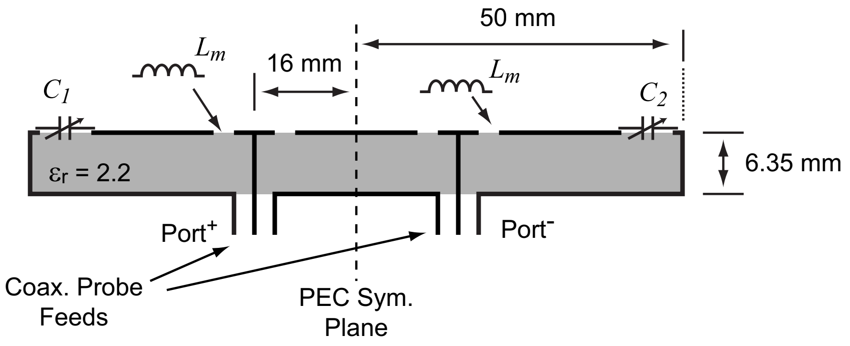

(a) Side View

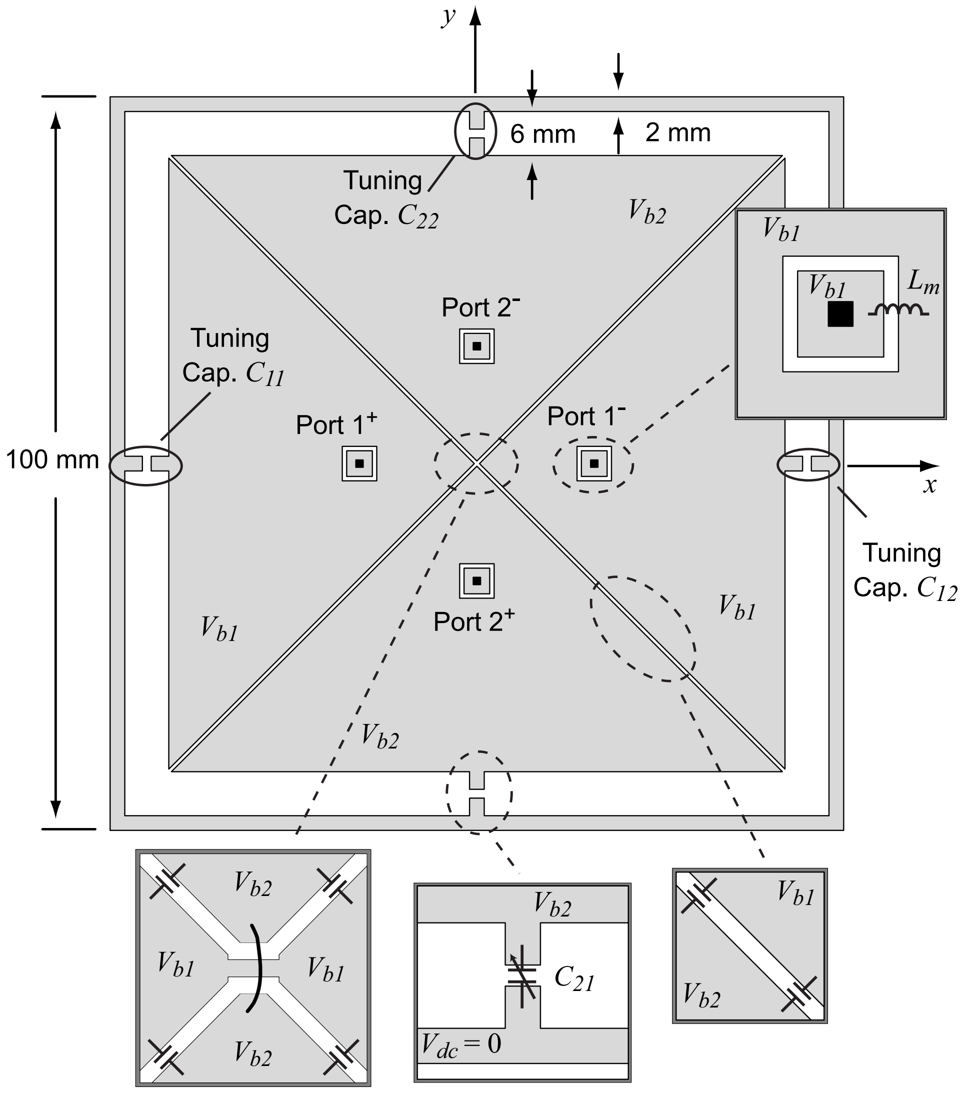

(b) Top View

Figure 5.3: Geometry of the dual-polarized cavity-backed patch antenna with independent tuning. RF-short-circuiting capacitors are placed across the diagonal biasing slots every 11 mm, as shown in the insets.

relative to the cavity. Independent tuning with high isolation requires that

$$\begin{aligned} C_{11} = C_{12} = C_1 \quad & \Longrightarrow \quad V_{b11} = V_{b12} = V_{b1} \\ C_{21} = C_{22} = C_2 \quad & \Longrightarrow \quad V_{b21} = V_{b22} = V_{b2} \\ C_1 \text{ and } C_2 \text{ independent} \quad & \Longrightarrow \quad V_{b1} \text{ and } V_{b2} \text{ independent,} \end{aligned}$$

where $V_{b\alpha\beta}$ is the bias voltage across varactor $C_{\alpha\beta}$. Therefore, the patch is separated into quadrants by 0.5-mm-wide biasing gaps. Each of these quadrants is DC-connected to Ports 1^+, 1^-, 2^+, and 2^- through the matching inductors, L_m, and the feed probes, and therefore, independent bias voltages can be applied to each quadrant through bias tees. Although each varactor can be biased independently to compensate for varactor mismatch, the horizontal and vertical quadrants are connected with jumpers in this work (Fig. 5.3(b)), reducing the complexity by enforcing $V_{b11} = V_{b12} = V_{b1}$ and $V_{b21} = V_{b22} = V_{b2}$.

The current on the patch from the TM^z_{100} and TM^z_{010} modes is significant over the whole width of the patch, but goes to zero at the respective E-plane edges. Therefore, the biasing gaps must be RF-short-circuited everywhere, except perhaps at the corners. Several methods of accomplishing this are explored in the results section, but finally, five 47-pF capacitors (AVX SQCS, 0603 package, $-j5.6\ \Omega$ reactance at 600 MHz) [46] are placed across the slot at an interval of 11 mm starting 11 mm from the corners.

5.2.3 Circuit Model and Full-Wave Simulations

Although the patch antenna can be simulated accurately using full-wave simulation methods such as the Method of Moments (MoM) and the Finite Element Method (FEM), considerable insight is gained using the transmission-line model. The tuning characteristics of the capacitively loaded patch are investigated using the transmission

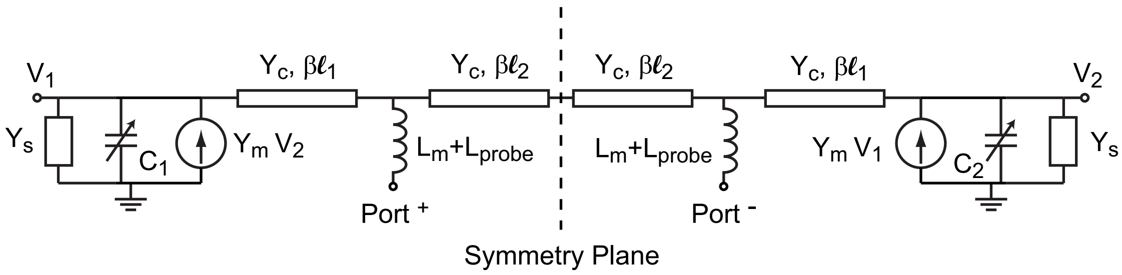

(a) With two probe feeds

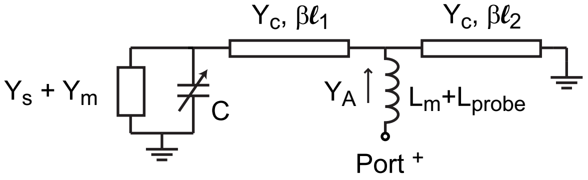

(b) Odd mode

Figure 5.4: Transmission-line model of the differentially-fed varactor-tuned patch antenna with mutual coupling analysis based on [2].

line model, and then compared with full-wave MoM simulated results.

Transmission-line model

In the transmission-line model, the patch is assumed to be a transmission-line section terminated by radiating slots. In the most simple model, introduced by Munson for the long microstrip radiator, the admittance of each slot is calculated by assuming that it is infinitely long, finding the admittance per unit length, and multiplying it by the length of the radiating slot [73]. This model was used by Schaubert et al. to predict the shift in resonance frequency of the microstrip patch when shorting pins are placed in various locations along its length [52]. A more accurate transmission-line model was presented by Pues et al. [2] that uses a more accurate model for the radiation conductance, including mutual coupling [74] and the effect of the side slots. The calculation of $Y_s = G_s + jB_s$, $Y_m = G_m + jB_m$, Y_c, β, and L_{via} is explained in Appendix B.

When the tuning capacitors are symmetric ($C_1 = C_2 = C$) and the antenna is fed

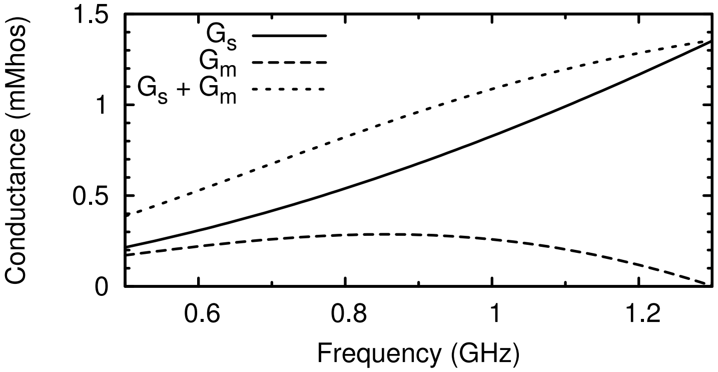

Figure 5.5: Radiating and mutual conductances of the radiating slots for an 84 × 84 mm^2 microstrip patch on a 6.35-mm-thick substrate with $\epsilon_r = 2.2$.

differentially, $V_1 = -V_2$ and the odd-mode equivalent circuit is shown in Fig. 5.4(b). The slot conductances are plotted in Fig. 5.5 for an 84 × 84 mm^2 microstrip patch on a 6.35-mm-thick substrate with $\epsilon_r = 2.2$ (the same dimensions patch dimensions as the cavity-backed patch presented in this chapter, except with no cavity). G_s increases as the square of the frequency, but the effective slot conductance, $G_s^e = G_s + G_m$ is increases linearly with frequency over the 0.5–1 GHz band. The effective slot susceptance, $B_s^e = B_s + B_m$, is capacitive and increases linearly with frequency.

The input impedance is calculated as follows:

$$Z_{in} = 1/Y_A + j\omega(L_{probe} + L_m), \tag{5.1}$$

where

$$Y_A = G_A + jB_A = Y_c \frac{jY_c \sin(\beta\ell_1) + Y_T \cos(\beta\ell_1)}{Y_c \cos(\beta\ell_1) + jY_T \sin(\beta\ell_1)} - jY_c \cot(\beta\ell_2) \tag{5.2}$$

is the admittance of the antenna at the probe feed,

$$Y_T = G_T + jB_T = Y_s^e + Y_{var} \tag{5.3}$$

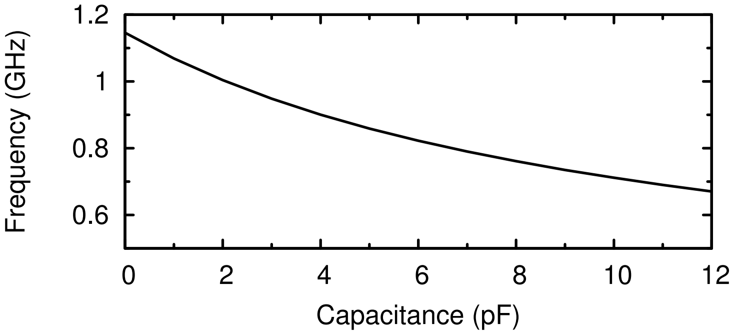

Figure 5.6: Calculated resonance frequency of the 84 × 84 mm^2 microstrip patch on a 6.35-mm-thick substrate with $\epsilon_r = 2.2$.

is the total admittance at the slot, $Y_s^e = Y_s + Y_m$, and

$$Y_{var} = (R_s - j/\omega C)^{-1} = \frac{j\omega C + \omega^2 C^2 R_s}{1 + (\omega C R)^2} \tag{5.4}$$

is the admittance of the varactor diode with capacitance C and series resistance R_s. Equivalently,

$$Y_{var} = \frac{B_{var}(j + 1/Q_{var})}{1 + 1/Q_{var}^2} \approx B_{var}(j + 1/Q_{var}) \tag{5.5}$$

when $Q_{var} \gg 1$, where $B_{var} = \omega C$ and $Q_{var} = 1/(\omega C R_s)$. Resonance occurs at the frequency, f_r, where

$$\Im\{Y_A\} = 0. \tag{5.6}$$

As C varies from 0–15 pF, f_r varies from 1.15–0.62 GHz (Fig. 5.6). Now that the circuit parameters and resonance frequency have been calculated, the varactor efficiency, η_{var}, and antenna conductance, G_A, can be calculated.

The varactor efficiency is the ratio of the power absorbed in G_s^e to the total power absorbed at the slot. It is simply a current divider:

$$\eta_{var} = \frac{G_s^e}{G_s^e + B_{var}/Q_{var}}. \tag{5.7}$$

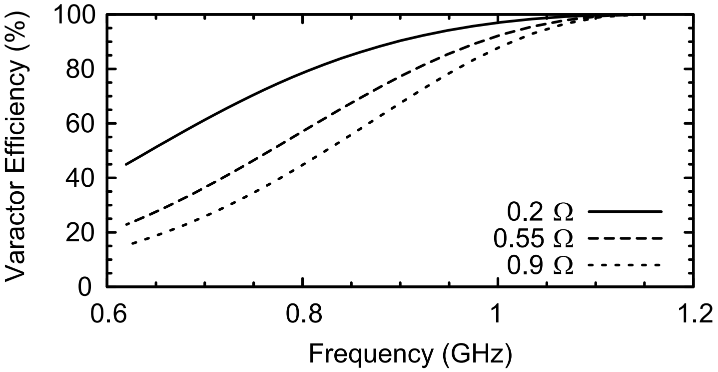

Figure 5.7: Calculated varactor efficiency, η_{var}, versus resonance frequency for the 84 × 84 mm^2 microstrip patch for different values of R_s.

The efficiency is plotted in Fig. 5.7 for $R_s = \{0.2, 0.55, 0.9\}$ Ω and C varying from 0–15 pF. R_s for the 10-cm and 5-cm antennas is 0.55 and 0.9 Ω, respectively.

G_A is found by taking the real part of the first term in (5.2):

$$G_A = \frac{Y_c^2 G_T}{Y_c^2 \cos^2(\beta\ell_1) - 2Y_c B_T \sin(\beta\ell_1)\cos(\beta\ell_1) + (G_T^2 + B_T^2)\sin^2(\beta\ell_1)}. \tag{5.8}$$

If G_T and B_T are $\ll Y_c$, then (5.8) reduces to $G_A = G_T/\cos^2(\beta\ell_1)$, as in [74]. For the varactor-tuned antenna, however, $G_T \ll Y_c$, but B_T can be comparable to Y_c when the capacitance is large. From (5.5) and (5.8), the antenna conductance is then:

$$G_A \approx \frac{Y_c^2(G_s^e + B_{var}/Q_{var})}{\left(Y_c\cos(\beta\ell_1) - (B_s^e + B_{var})\sin(\beta\ell_1)\right)^2}. \tag{5.9}$$

The impedance match to 50 Ω is one factor that determines the useful tuning range of the antenna. As the capacitance increases and f_r decreases, $B_{var}(f_r)$ increases, Q_{var} decreases, and G_s^e decreases. The behavior of the denominator in (5.9) depends on the location of the feed. G_A is plotted for feed locations $\ell_2 = 8$ and 16 mm in Fig. 5.8 for different values of R_s. For ideal varactors, G_A is nearly constant for the high frequencies, but decreases at the low frequencies when $\ell_2 = 8$ and 16 mm. As R_s increases, G_A increases at the low frequencies. When $\ell_2 = 8$ mm and $R_s \leq$

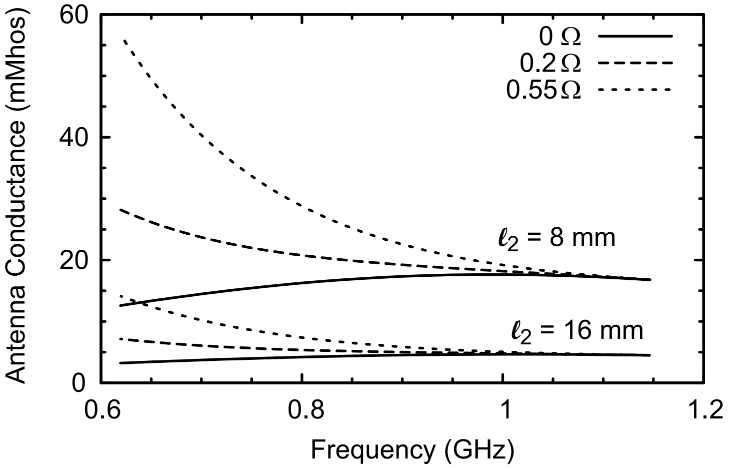

Figure 5.8: Antenna conductance, G_A, for different values of R_s and ℓ_2 for the 84 × 84 mm^2 microstrip patch.

0.2 Ω, the antenna is matched to 50 Ω over the tuning range, but these resistance values are unrealistic in most cases. Therefore, the antenna cannot be matched at resonance over the 0.6–1 GHz frequency range. Instead, it is matched with a series inductor like the cavity-backed slot antenna in Chapter 4. This inductor behaves like an inductive admittance inverter [51], which scales an admittance, Y, as $Y' = 1/(\omega^2 L^2 Y)$. Although the series inductor is not exactly an admittance inverter, it has similar behavior, having a larger effect on the higher frequencies. A capacitor has the opposite effect, and would be chosen if G_A were increasing with frequency. The fact that an inductor is the matching element of choice is quite convenient because the probe feeds are inductive.

Finally, Z_{in} is plotted in Fig. 5.9 for L_m = 5.8 nH as C varies from 0–15 pF. The transmission-line model predicts one octave of tuning for this capacitance range, which is much larger than is practical. It will be shown by full-wave simulation and measurement that the transmission-line model underestimates the sensitivity of the microstrip patch antenna to capacitive loading. Reducing L_m will result in a better impedance match over this tuning range, but 5.8 nH is plotted in order to compare with full-wave simulations.

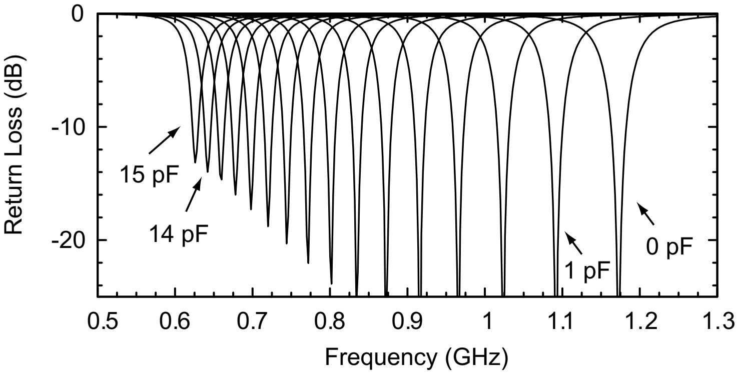

(a)

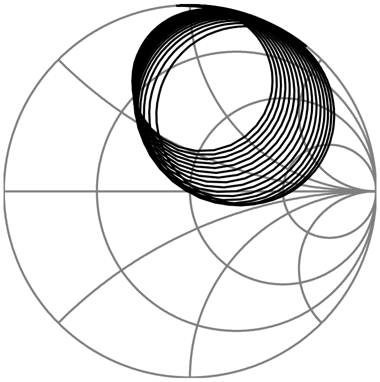

(b) Z_{in}

Figure 5.9: Return loss and input impedance of the 84 × 84 mm^2 microstrip patch predicted by the transmission-line model as C varies from 0–15 pF.

Full-wave simulation

The tunable cavity-backed patch antenna was simulated in IE3D (MoM) [24]. First, simulated results of an 84 × 84 mm^2 microstrip patch antenna are presented to evaluate the transmission-line model, and second, simulated results for the cavity-backed patch are presented.

The microstrip patch antenna with $W = L = 84$ mm, an infinite 6.35-mm-thick substrate with $\epsilon_r = 2.2$, 5.8 nH matching inductance, and a differential feed with $\ell_2 = 16$ mm was simulated in IE3D by placing probe ports along the x axis at the locations of the coaxial feeds and vertical localized ports along the x axis at the patch edges for the varactor diodes. The 4-port S-parameters were reduced to 2-port by placing capacitors and resistors across the appropriate ports, and then calculating the differential reflection coefficient, as explained later in this section. The reflection coefficient is plotted in Fig. 5.10 for $R_s = 0.55\ \Omega$ and C varying from 0–6 pF. The simulated results show that the microstrip patch is much more sensitive to capacitive loading than predicted by the transmission-line model (Fig. 5.9); the antenna tunes from 1.14 down to 0.65 GHz over this range, whereas the transmission-line model predicts that 13 pF are required to tune down to 0.65 GHz. This was also observed in [9] and [10], and can be explained as follows: the transmission-line model assumes no variation of the field or the current along the radiating slot, i.e. that the slot admittance is distributed along its length. When a single varactor diode is placed across each slot, current flows toward it along the slot edge to meet the reactive boundary condition at the location of the varactor—adding inductance in series with the varactor and increasing its loading effect. This effect is negligible at small capacitances, and therefore, the tuning range for a given capacitance ratio is higher than the transmission-line model predicts. Although the model underestimates the tuning sensitivity, the difference in the resonant input resistance is small enough (at least in this case) that the transmission-line model provides good initial values

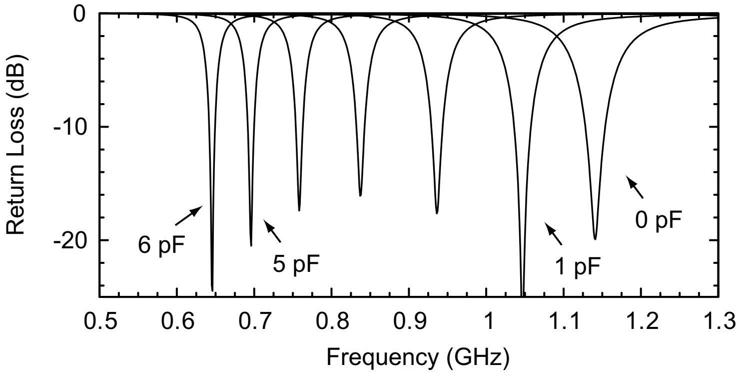

(a)

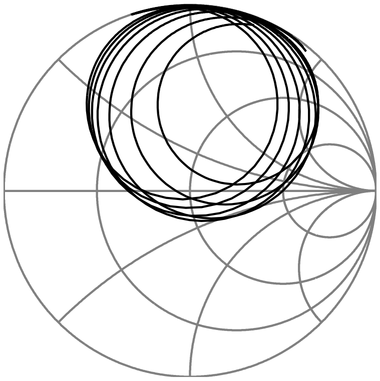

(b) Z_{in}

Figure 5.10: Simulated return loss and input impedance of the 84 × 84 mm^2 microstrip patch as C varies from 0–6 pF.

for the feed location and matching inductance.

A finite dielectric, meshed at 40 cells per wavelength, was used to simulate the cavity-backed patch as shown in Fig. 5.3. Copper (conductivity 5.8×10^7 S/m) was assumed for all metal. Probe ports were used at ports 1^+, 1^-, 2^+, and 2^-, and horizontal localized ports were used in place of the varactor diodes. An infinite ground plane was used for the bottom of the cavity, both to reduce the computational complexity, and to simulate the case where the antenna placed on a large conducting object. The gaps for bias isolation and the matching inductors were not included in the simulation. The 8-port structure was re-simulated with the matching inductors on all four input ports, and then, the varactor loading was calculated as explained in

Appendix C.

The differential and common mode S-parameters are found by assuming that the antenna is connected to an ideal 180° hybrid. The differential-to-differential-mode S-parameters are calculated as

$$S_{11}^{dd} = 0.5(S_{1p1p} - S_{1p1m} - (S_{1m1p} - S_{1m1m})), \tag{5.10a}$$

$$S_{22}^{dd} = 0.5(S_{2p2p} - S_{2p2m} - (S_{2m2p} - S_{2m2m})), \tag{5.10b}$$

$$S_{12}^{dd} = 0.5(S_{1p2p} - S_{1p2m} - (S_{1m2p} - S_{1m2m})), \tag{5.10c}$$

$$S_{21}^{dd} = 0.5(S_{2p1p} - S_{2p1m} - (S_{2m1p} - S_{2m1m})), \tag{5.10d}$$

where the subscripts p and m refer to $^+$ and $^-$ respectively. The differential-to-common-mode S-parameters are calculated as

$$S_{11}^{cd} = 0.5(S_{1p1p} - S_{1p1m} + (S_{1m1p} - S_{1m1m})), \tag{5.11a}$$

$$S_{22}^{cd} = 0.5(S_{2p2p} - S_{2p2m} + (S_{2m2p} - S_{2m2m})), \tag{5.11b}$$

$$S_{12}^{cd} = 0.5(S_{1p2p} - S_{1p2m} + (S_{1m2p} - S_{1m2m})), \tag{5.11c}$$

$$S_{21}^{cd} = 0.5(S_{2p1p} - S_{2p1m} + (S_{2m1p} - S_{2m1m})). \tag{5.11d}$$

The simulations predict tuning from about 1 GHz to 0.6 GHz for a capacitance range of 1.2–5.4 pF (Figs.5.11 and 5.12). The simulated 10-dB impedance bandwidth varies from about 1.8–1% over the tuning range. As the loading capacitors C_1 and C_2 become independent, the two polarizations resonate at different frequencies; f_{01} is dependent on C_1 but not C_2, and vice versa. The simulated differential-differential-mode isolation (S_{12dd} and S_{21dd}) and differential-common-mode coupling (S_{11cd}, S_{22cd}, S_{12cd}, and S_{21cd}) are < -40 dB over the tuning range, as expected due to symmetry.

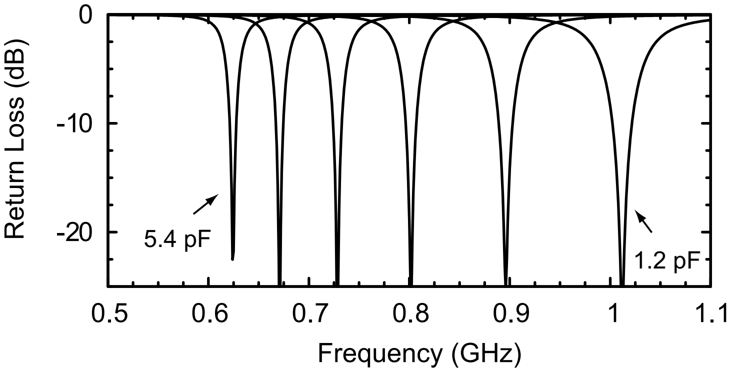

(a)

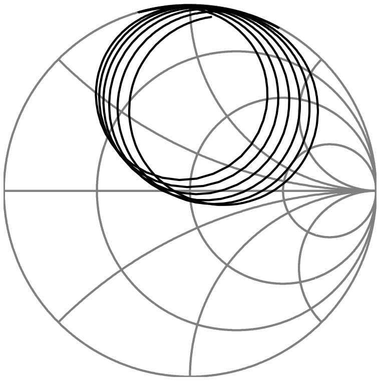

(b) Z_{in}

Figure 5.11: Simulated return loss and input impedance of the 10-cm antenna as all loading capacitors vary from 1.2–5.4 pF in 0.84-pF steps.

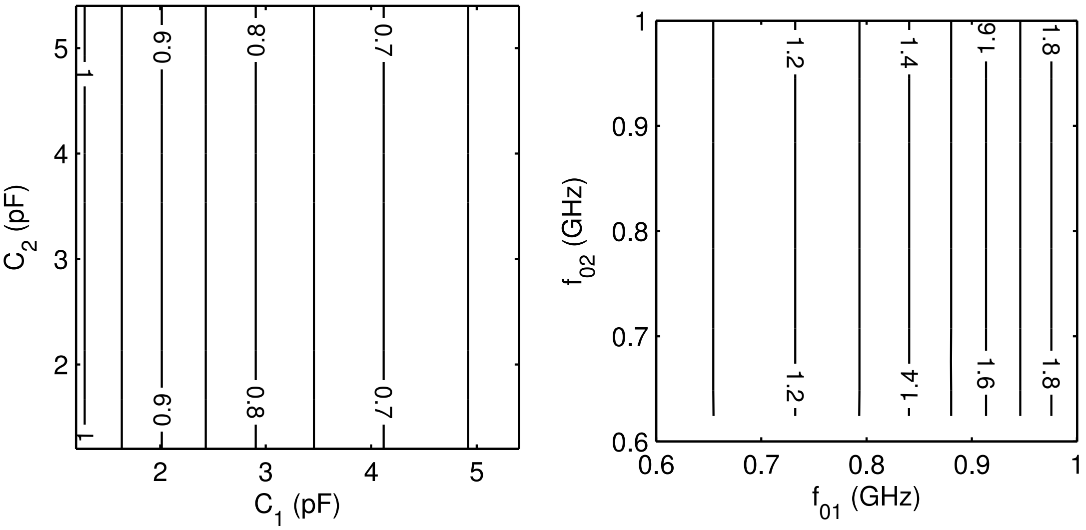

(a) f_{01} (GHz)

(b) 10-dB bandwidth (%)

Figure 5.12: Simulated center frequency and 10-dB impedance bandwidth over the tuning range of the cavity-backed patch when fed at Port 1.

5.2.4 Fabrication of the Prototypes

Two prototypes of the cavity-backed patch antenna were fabricated based on the geometry in Fig. 5.3. The first is a full-scale prototype of the antenna described above, hereafter referred to as the 10-cm antenna, and the second is a 0.5:1 scale model, hereafter referred to as the 5-cm antenna.

10-cm Antenna

The antenna was fabricated using two 3.18-mm sheets of Rogers 5880 substrate material with double-sided 35 μm copper cladding. The antenna was constructed in the following way:

1. The top metal pattern (Fig. 5.3(b)) was created on one sheet by removing the copper from the slot areas with a CNC milling machine.

2. Holes were drilled in both the top and bottom sheets for the probe feeds, and circular sections of metal (5 mm in diameter) were removed on the bottom sheet to allow the coaxial lines to mate with the bottom of the cavity (Fig. 5.3(a)).

3. Excess substrate material was removed from around the edges of the antenna with a shear, and the unwanted copper layers (the bottom of the top sheet and the top of the bottom sheet) were removed with a milling machine.

4. Flange-mount SMA connectors were soldered to the bottom ground, and the top sheet was set in its place. The center pins were then soldered to the patch, connecting the two sheets.

5. The sidewalls of the cavity were made by wrapping conductive-adhesive copper tape from the bottom ground to the metal ring at the edge of the top sheet. All seams were soldered to ensure low resistance.

6. The varactor diodes and matching inductors (Coilcraft 0603CS-5N6X_L [45], 5.8 nH at 900 MHz) were soldered to the top sheet. The varactor diodes are Skyworks SMV1405-074 silicon abrupt-junction common-cathode pairs [72] that are connected in parallel to achieve a capacitance range of ≈ 1.2–5.4 pF from 0–30 V with an equivalent series resistance (ESR) of ≈ 0.55 Ω.

7. Different methods of RF-short-circuiting the bias gaps are described in the results section, but finally, five 47-pF capacitors were soldered across each biasing gap at an interval of 11 mm.

5-cm Antenna

The 5-cm antenna is approximately a 0.5:1 scale model of the 10-cm antenna. The cavity is $5 \times 5 \times 3.18$ mm^3, and the radiating slots are 3 mm wide. The probe-feeds are 8 mm from the center of the antenna. Many of the small dimensions, however, are not scaled; as in the 10-cm antenna, the biasing gaps are 0.5 mm wide, the gaps surrounding the probe feeds have inner and outer widths of 3.5 and 4.7 mm, respectively, and the ring surrounding the radiating slots is 2 mm wide. Furthermore, the SMA connectors are not scaled. The varactor diodes in the 5-cm antenna are M/A Com MA46H071-1056 GaAs hyperabrupt junction diodes with a capacitance range of ≈ 0.45–2.5 pF from 0–20 V with an ESR of ≈ 0.9 Ω. The matching inductors are 2.2 nH (Coilcraft 0603CS-2N2X_L [45], 2.2 nH at 1.7 GHz).

The prototype was fabricated in the same manner as the 10-cm prototype, except that it was made from a single sheet of substrate material.

5.3 Results and Analysis

The 5-cm antenna was fabricated first, and its S-parameters were measured with several different configurations for RF-short-circuiting the biasing gaps. Insight was gained from these tests, and applied to the 10-cm antenna. The S-parameters and antenna gain patterns of the 10-cm antenna were measured, and are presented below.

5.3.1 5-cm Antenna

The 4-port S-parameters of the antenna were measured using a 2-port Agilent E5071B network analyzer by measuring the two-port S-parameters of at all six combinations of ports $\{1^+, 1^-, 2^+, 2^-\}$ with the unused ports terminated in 50 Ω. The bias voltage for this antenna is applied to the RF lines with bias tees, and therefore, all antenna ports have a DC voltage. DC blocks were placed on the antenna ports that did not have bias tees in order to isolate the bias voltage from the network analyzer and the 50 Ω loads. The measurement setup to measure ports 1^+ and 1^- is shown in Fig. 5.13. The source power was set to -30 dBm in order to ensure that the diodes were in the small signal region, and the antenna was placed on a foam block about 1 m from any scatterers.

It was assumed in the design and simulations that the patch is one continuous piece of metal, but it is necessary to divide it into at least two sections in order to bias the two polarizations independently. Capacitance is then placed across the biasing gaps in order to RF-short-circuit them. The S-parameters of the following cases were compared for $V_{b1} = V_{b2}$ in order to determine how much capacitance is needed:

- Two capacitors across each biasing gap.

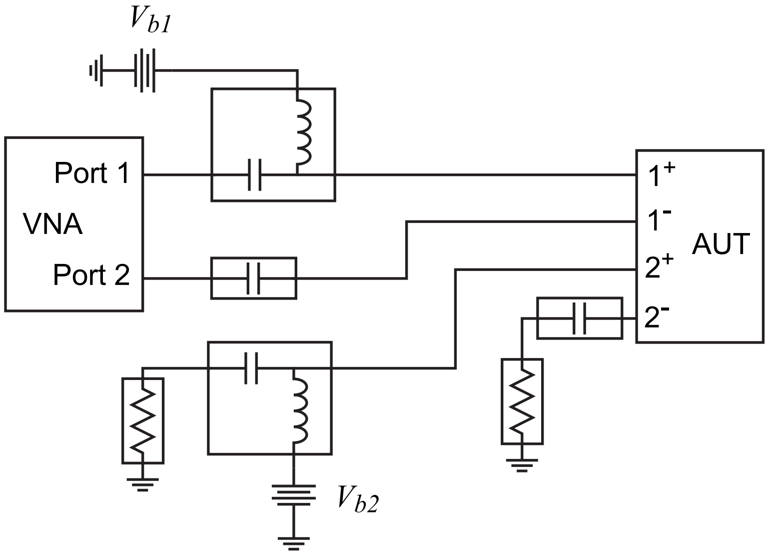

Figure 5.13: Setup to measure the S-parameters at ports 1^+ and 1^-. There are five more combinations necessary to measure the 4-port S-parameters.

- Three capacitors across each biasing gap.
- Three capacitors across each biasing gap with insulating-adhesive copper tape across the exposed gaps.
- Conductive-adhesive copper tape across the biasing gaps.

It can be seen from Fig. 5.14 that there is a significant difference between the cases of two capacitors and the case of conducting-adhesive copper tape. As the number of capacitors increases, the return loss response approaches the case of the antenna with conductive-adhesive copper tape. Three capacitors per arm were not sufficient to converge to the ideal case of RF-short-circuiting the biasing gaps.

The impedance of each varactor diode was measured before it was installed on the antenna. The simulated antenna structure was then loaded with the measured capacitance and resistance values, and the return loss of port 1 is compared with the measured values in Fig. 5.14. The two cases are also compared on the Smith Chart in Fig. 5.15. The two cases are very close on the Smith Chart, but the simulated structure predicts a slightly larger tuning range than the fabricated antenna. This

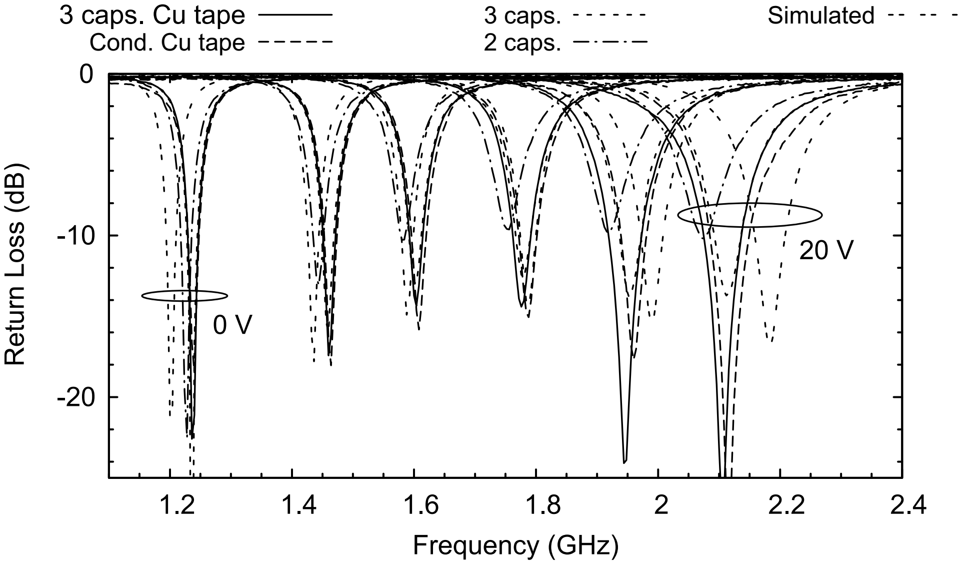

Figure 5.14: Return loss of the 5-cm antenna with different methods of RF-short-circuiting the biasing gaps when $V_{b1} = V_{b2} = \{0, 1, 2, 4, 8, 20\}$.

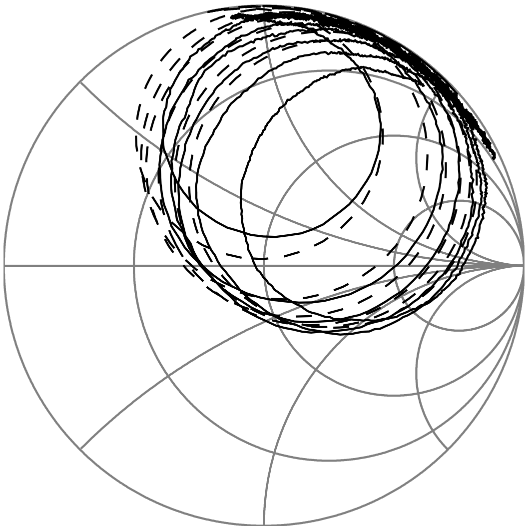

Figure 5.15: Differential input impedance at port 1 of the 5-cm cavity-backed patch when $V_{b1} = V_{b2} = \{0, 1, 2, 4, 8, 20\}$. Solid line: Measured with conductive-adhesive copper tape over the biasing gaps. Dashed line: Simulated with the measured varactor impedance values.

implies that the simulated conductance was sufficiently accurate, but there is a difference in the susceptance between measured and simulated cases. Still, the simulation is reasonably accurate.

The 4-port S-parameters of the antenna were measured for the case of 3 capacitors per biasing-slot and insulating-adhesive copper tape for all combinations of V_{b1} and V_{b2} in $\{0, 1, 2, 4, 8, 20\}$, and the differential-to-differential and differential-to-common mode S-parameters are shown in Figures 5.16 and 5.17, respectively, for $V_{b2} = 2$ V ($f_{02} = 1.6$ GHz). As V_{b1} varies from 0–20 V, f_{01} varies from 1.2–2.1 GHz while f_{02} remains constant and the isolation, S_{21d}, remains better than 20 dB. As expected, there is very little coupling between the differential and common modes.

Figures 5.18–5.21 summarize the 4-port S-parameters of the 5 cm antenna. f_{01} is independent of V_{b2}, and f_{02} is independent of V_{b1} over the entire tuning range. The 10-dB impedance bandwidth of both of the polarizations varies from 1.4% at 1.2 GHz to 2.8% at 2.1 GHz (Fig. 5.19). The in-band isolation is the lowest when $f_{01} = f_{02}$, but is better than 20 dB over the whole tuning range (Fig. 5.20), where the in-band isolation is defined as follows. For the self terms, S_{11cd} and S_{22cd}, it is the minimum isolation within the 10-dB impedance bandwidth centered about f_{01} and f_{02}, respectively. For the cross terms, it is defined as the minimum isolation within the 10-dB bandwidths centered about *both* f_{01} and f_{02}. The differential-to-common mode isolation isolation is better than 20 dB over the whole tuning range (Fig. 5.21). The high isolation over the entire tuning range implies that antenna is quite symmetric.

5.3.2 10-cm Antenna

S-parameters

The 4-port S-parameters of the 10-cm antenna were measured by the same method as for the 5-cm antenna: the two-port S-parameters of at all six combinations of ports

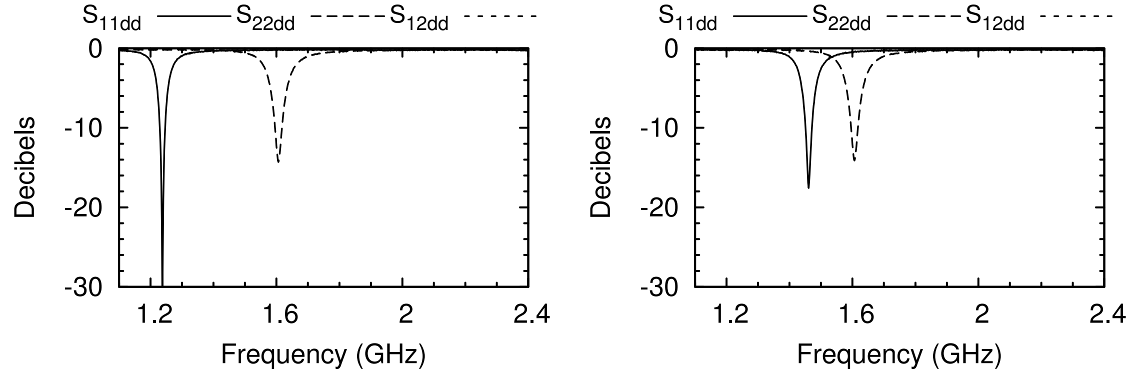

(a) $V_{b1} = 0$ V, $V_{b2} = 2$ V (b) $V_{b1} = 1$ V, $V_{b2} = 2$ V

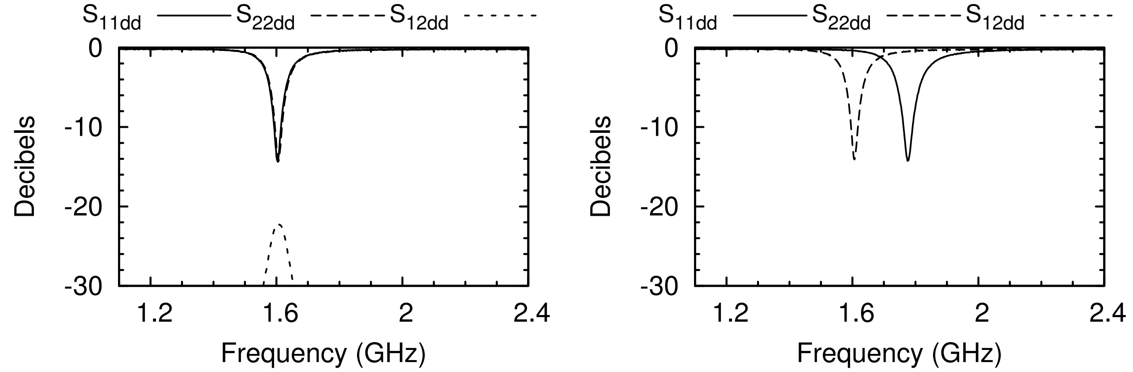

(c) $V_{b1} = 2$ V, $V_{b2} = 2$ V (d) $V_{b1} = 4$ V, $V_{b2} = 2$ V

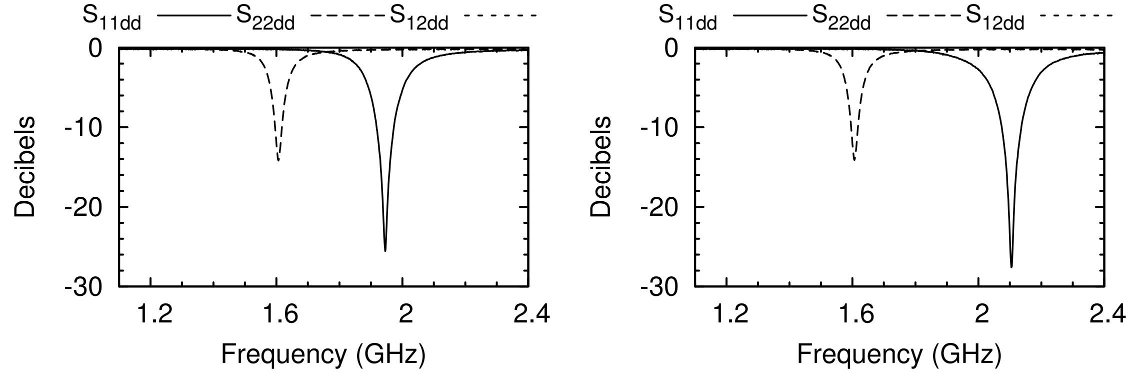

(e) $V_{b1} = 8$ V, $V_{b2} = 2$ V (f) $V_{b1} = 20$ V, $V_{b2} = 2$ V

Figure 5.16: Differential-to-differential S-parameters of the 5-cm antenna when $V_{b2} = 2$ V.

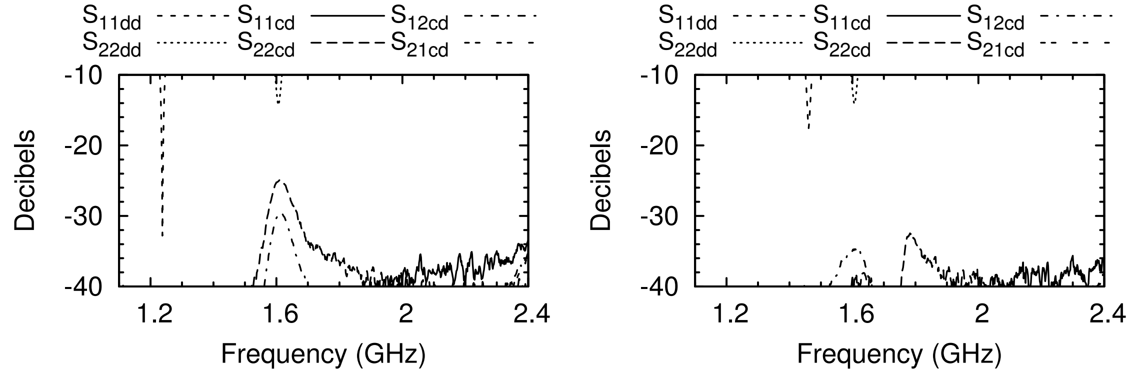

(a) $V_{b1} = 0$ V, $V_{b2} = 2$ V

(b) $V_{b1} = 1$ V, $V_{b2} = 2$ V

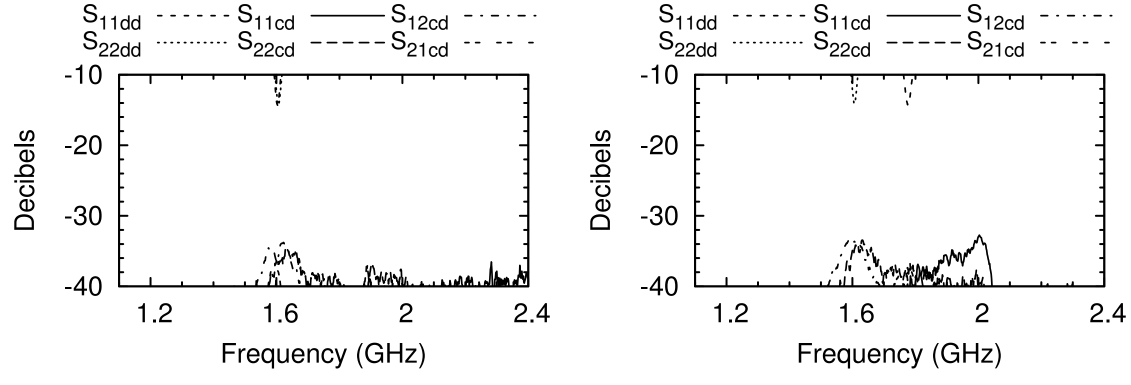

(c) $V_{b1} = 2$ V, $V_{b2} = 2$ V

(d) $V_{b1} = 4$ V, $V_{b2} = 2$ V

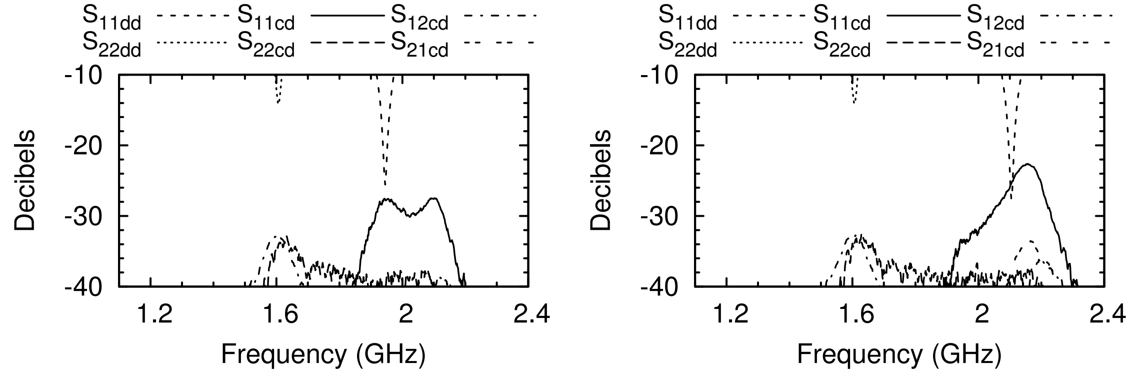

(e) $V_{b1} = 8$ V, $V_{b2} = 2$ V

(f) $V_{b1} = 20$ V, $V_{b2} = 2$ V

Figure 5.17: Differential-to-common mode S-parameters of the 5-cm antenna when $V_{b2} = 2$ V.

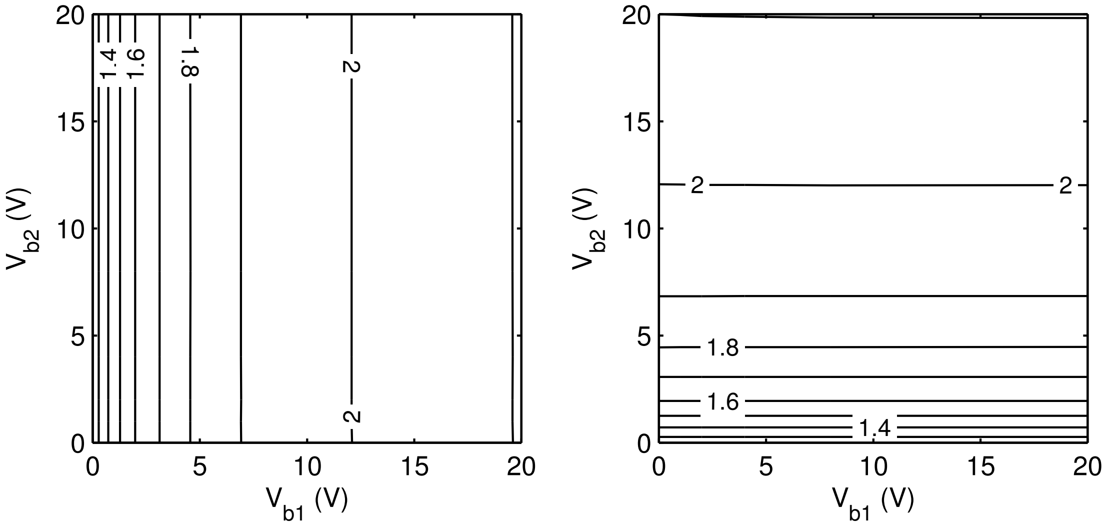

(a) f_{01}

(b) f_{02}

Figure 5.18: Center frequency of the 5-cm antenna as a function of V_{b1} and V_{b2}.

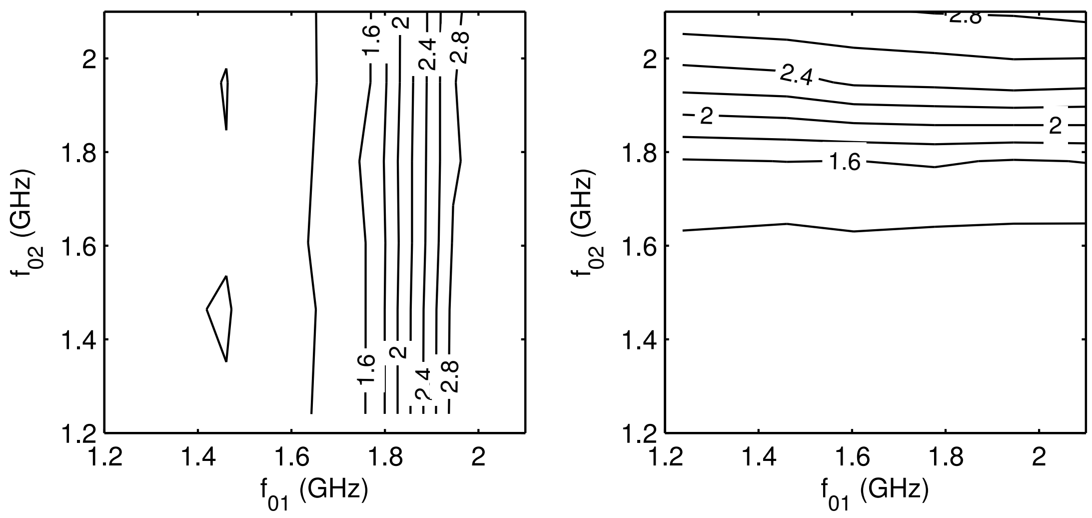

(a) Port 1

(b) Port 2

Figure 5.19: 10-dB impedance bandwidth of (a) polarization 1, and (b) polarization 2 of the 5-cm antenna in percent as a function of f_{01} and f_{02}.

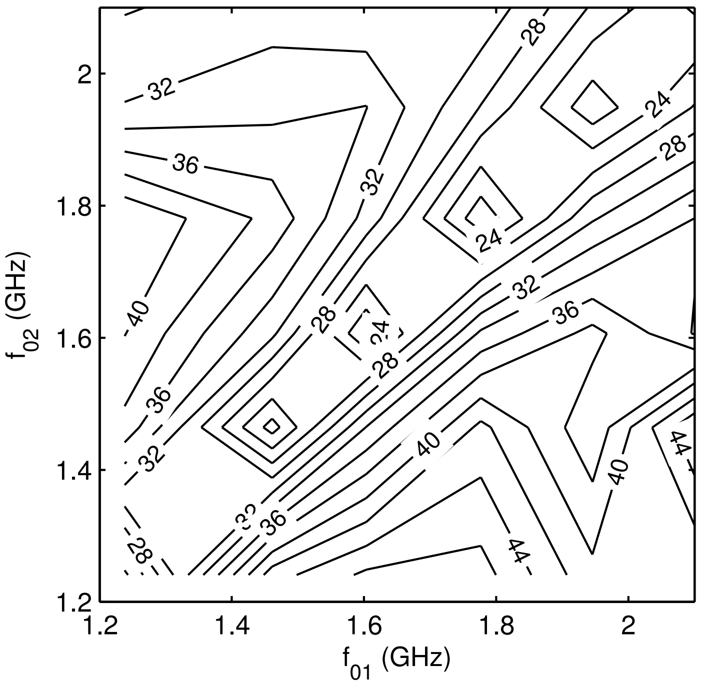

Figure 5.20: Minimum in-band differential-to-differential isolation in decibels between ports 1 and 2 of the 5-cm antenna.

$\{1^+, 1^-, 2^+, 2^-\}$ were measured with the unused ports terminated in 50 Ω, as shown in Fig. 5.13. The source power was set to -30 dBm in order to ensure that the diodes were in the small signal region, and the antenna was placed on a foam block about 1 m from any scatterers. Assuming that the antenna is connected to an ideal 180° hybrid, the differential and common mode S-parameters are found by (5.10) and (5.11), respectively.

It was found for the 5-cm antenna that placing 3 capacitors across each biasing gap is not sufficient to RF-short-circuit the biasing gaps. Therefore, three configurations were tested for the 10-cm antenna with $V_{b1} = V_{b2}$:

- 25-mm-wide insulating-adhesive copper tape was placed along the entire biasing gap, and then cut to the shape so that it did not cover any other gap/slot. The adhesive is acrylic and is 0.05 mm thick.
- Five capacitors across each biasing gap.

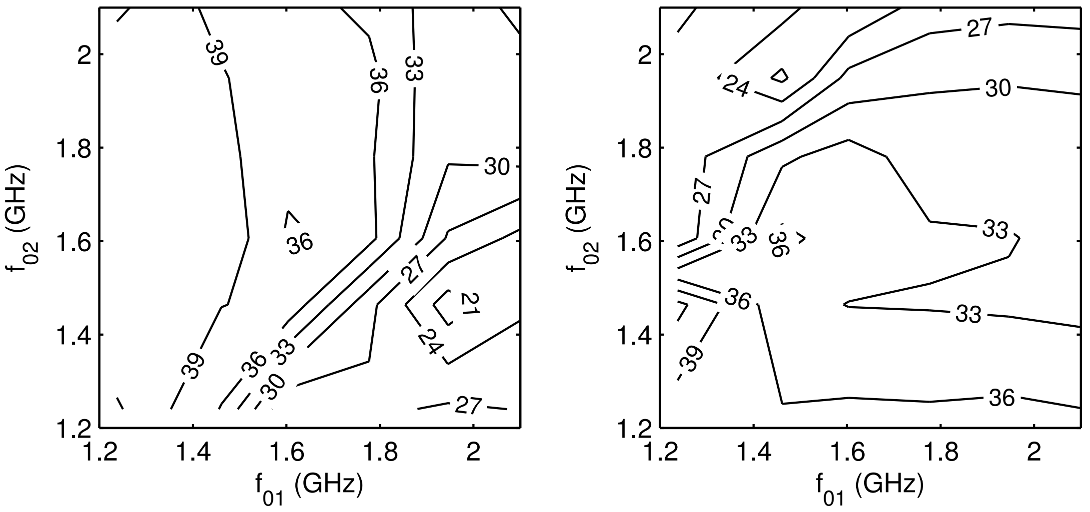

(a) S_{11cd} (b) S_{22cd}

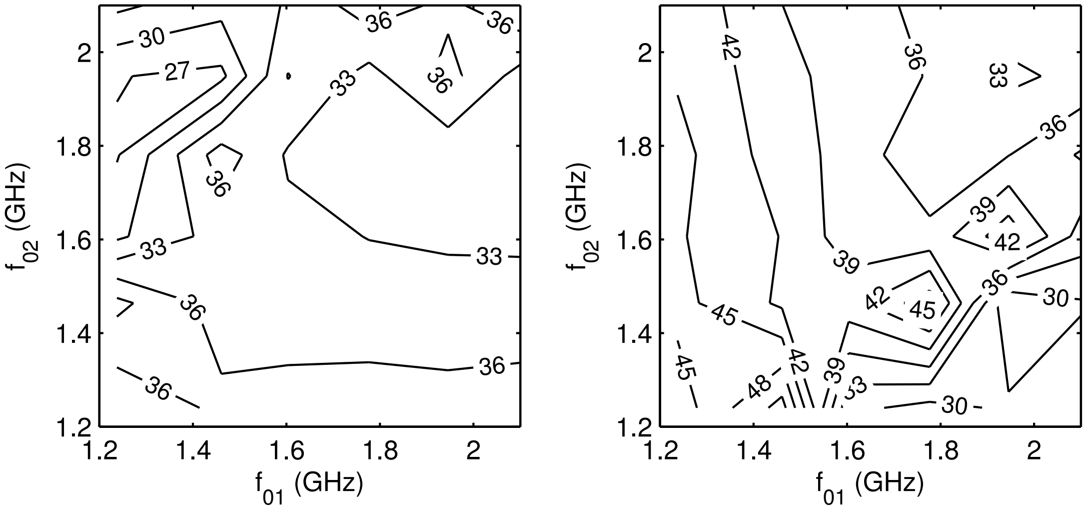

(c) S_{12cd} (d) S_{21cd}

Figure 5.21: Minimum in-band differential-to-common mode isolation of the 5-cm antenna.

- Conductive-adhesive copper tape across the biasing gaps.

It can be seen from Fig. 5.22 that the antenna tunes from <0.6 GHz to nearly 1 GHz with <-20 dB return loss when conductive-adhesive copper tape is covering the biasing gaps. The return loss is nearly the same with 5 capacitors across each gap. The impedance match is degraded, however, when insulating-adhesive copper tape is placed across the gap. Furthermore, the resonance frequency is slightly increased at all bias states, which is consistent with adding a series capacitance to the structure. All remaining measurements in this section are made with five 47-pF capacitors across each biasing gap unless otherwise noted.

S_{11dd} is compared with S_{22dd} in Fig. 5.23 for both the 5-capacitor case and the conductive-adhesive copper tape case when $V_{b1} = V_{b2} = \{0, 1, 2, 4, 8, 30\}$. $f_{01} < f_{02}$ for the lower bias voltages, but $f_{01} \approx f_{02}$ at the higher bias voltages. It is clear that there is some asymmetry in the antenna that is causing the difference in resonance frequency at the lower frequencies. The fact that this occurs identically for the 5-capacitor case and the conductive-adhesive copper tape case eliminates asymmetry in the bias capacitors as the cause. Furthermore, S_{11dd} and S_{22dd} follow nearly identical paths on the Smith Chart (Fig. 5.24). Therefore, the effects of inductance variations between the matching inductors (which shift the curves toward the top of the Smith Chart) are minor. The most likely reason for the asymmetry is varactor mismatch, which not only causes the two polarizations to resonate at different frequencies, but also couples the differential and common modes.

The 4-port S-parameters of the antenna were measured for all combinations of V_{b1} and V_{b2} in $\{0, 0.5, 1, 2, 4, 8, 16, 30\}$, and the differential-to-differential mode S-parameters are shown in Fig. 5.25 for $V_{b2} = 4$ V. As V_{b1} varies from 0–30 V, f_{01} varies from 0.6–1 GHz while f_{02} remains constant and the isolation, S_{21dd}, remains better than -30 dB. The differential-to-differential S-parameters of all tuning states are summarized in Fig. 5.26-5.28. f_{01} is independent of V_{b2}, and f_{02} is independent of

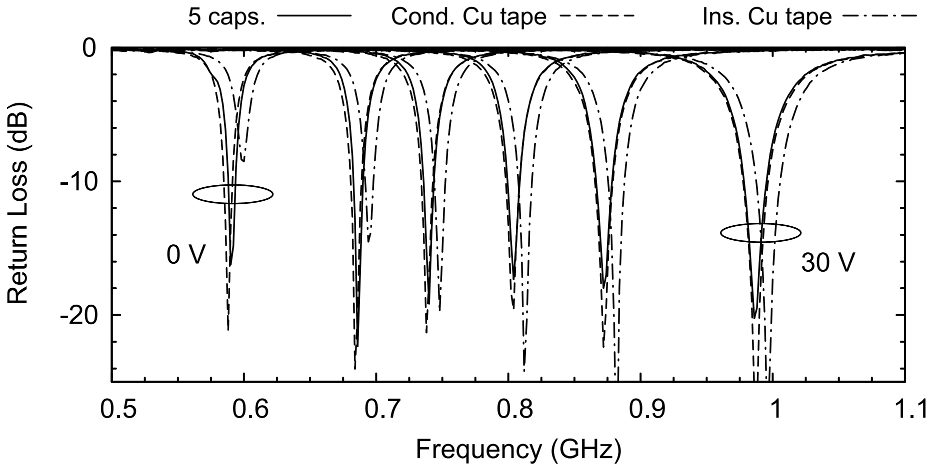

Figure 5.22: Return loss of the 10-cm antenna with different methods of RF-short-circuiting the biasing gaps for $V_{b1} = V_{b2} = \{0, 1, 2, 4, 8, 30\}$.

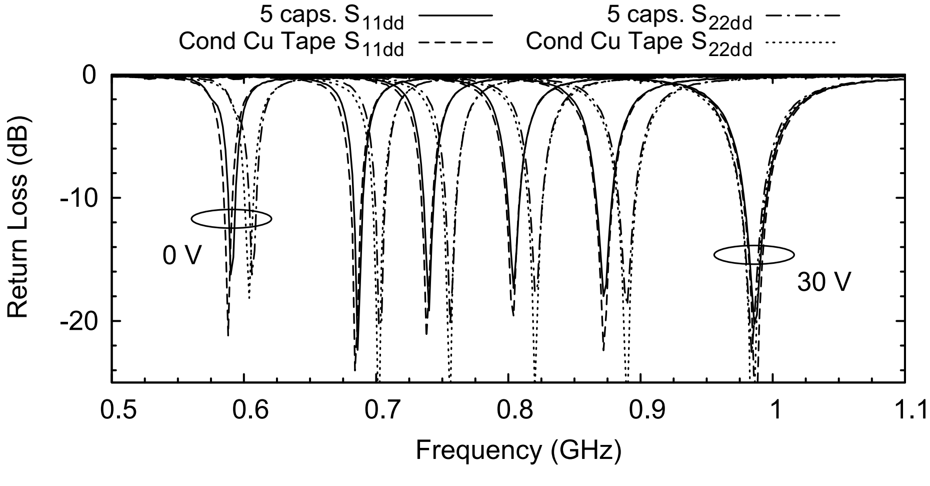

Figure 5.23: Comparison of S_{11dd} and S_{22dd} of the 10-cm antenna either capacitors or conductive-adhesive copper tape RF-short-circuiting the biasing gaps for $V_{b1} = V_{b2} = \{0, 1, 2, 4, 8, 30\}$.

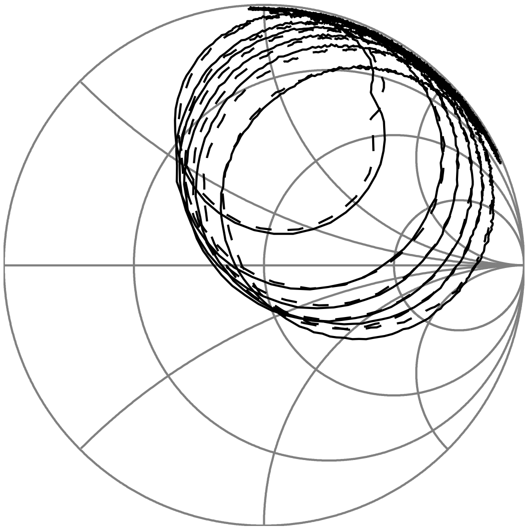

Figure 5.24: S_{11dd} and S_{22dd} of the 10-cm antenna for $V_{b1} = V_{b2} = \{0, 1, 2, 4, 8, 30\}$.

V_{b1} over the entire tuning range (Fig. 5.26). The 10-dB impedance bandwidths show little variation with the cross-polarized bias voltage, and vary from $\approx 0.9\%$ at 0.6 GHz 1.8% at 1 GHz (Fig. 5.27). The variations that are present are caused by coupling to the common modes, as shown below. The in-band differential-to-differential mode isolation—defined as the reciprocal of the maximum value of S_{21dd} within the 10-dB impedance bandwidths of both polarizations—is > 28 dB over the entire tuning range (Fig 5.28). For the 5-cm antenna, the highest S_{21dd} values occur when $f_{01} = f_{02}$, and because this does not occur at the same bias voltage for the 10-cm prototype (due to varactor mismatch), the antenna was re-measured with both polarizations tuned to the same frequency over the 650–980 MHz range. In this case, the differential-to-differential and differential-to-common mode isolations are still higher than 29 dB and 22 dB, respectively.

The differential-to-common mode S-parameters are shown in Fig. 5.29 for $V_{b2} =$ 4 V. The differential-to-common mode reflection terms, S_{11cd} and S_{22cd}, and transmission terms, S_{12cd} and S_{21cd}, are below -20 dB for most tuning states, but S_{22cd} is as high as -16 dB when $V_{b1} = 0$ V. The frequency responses of the terms originating

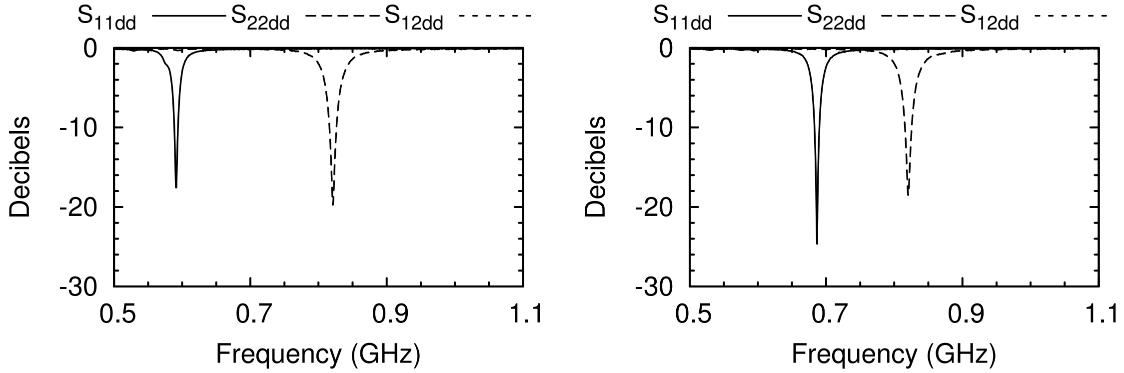

(a) $V_{b1} = 0$ V, $V_{b2} = 4$ V (b) $V_{b1} = 1$ V, $V_{b2} = 4$ V

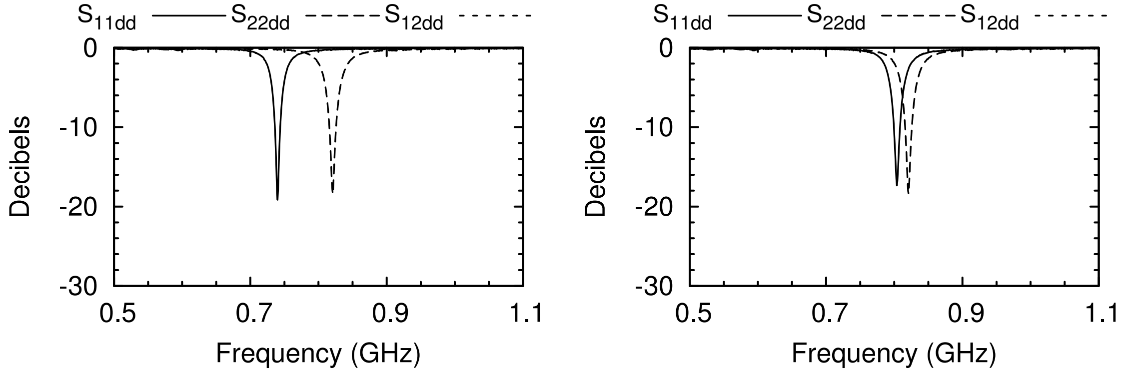

(c) $V_{b1} = 2$ V, $V_{b2} = 4$ V (d) $V_{b1} = 4$ V, $V_{b2} = 4$ V

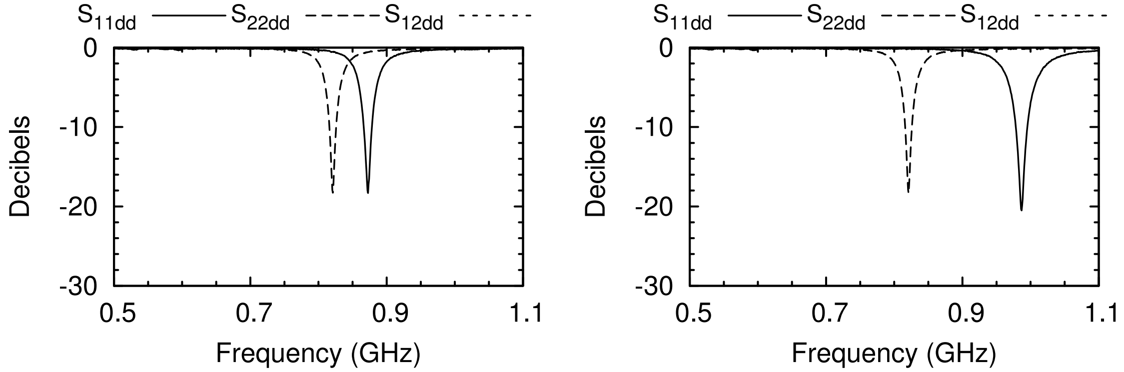

(e) $V_{b1} = 8$ V, $V_{b2} = 4$ V (f) $V_{b1} = 30$ V, $V_{b2} = 4$ V

Figure 5.25: Differential-to-differential mode S-parameters of the 10-cm antenna when $V_{b2} = 4$ V.

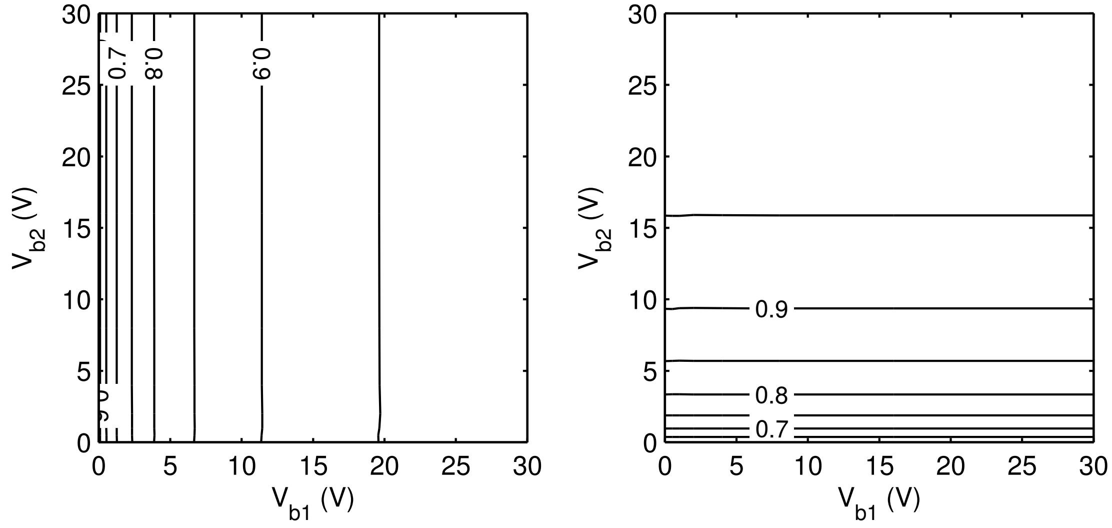

(a) f_{01} (b) f_{02}

Figure 5.26: Center frequency as a function of V_{b1} and V_{b2}.

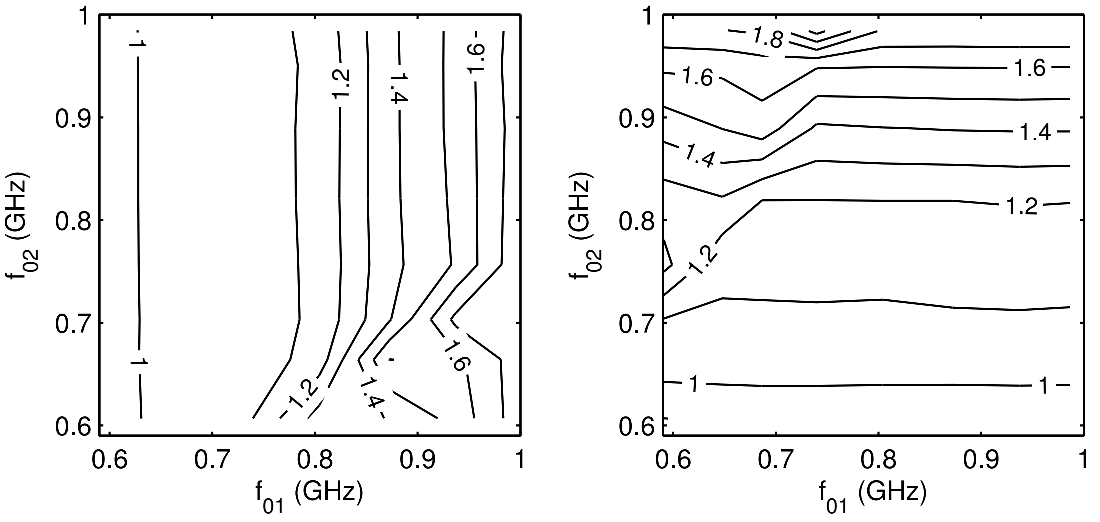

(a) Port 1 (b) Port 2

Figure 5.27: 10-dB impedance bandwidth of (a) polarization 1, and (b) polarization 2 in percent as a function of f_{01} and f_{02}.

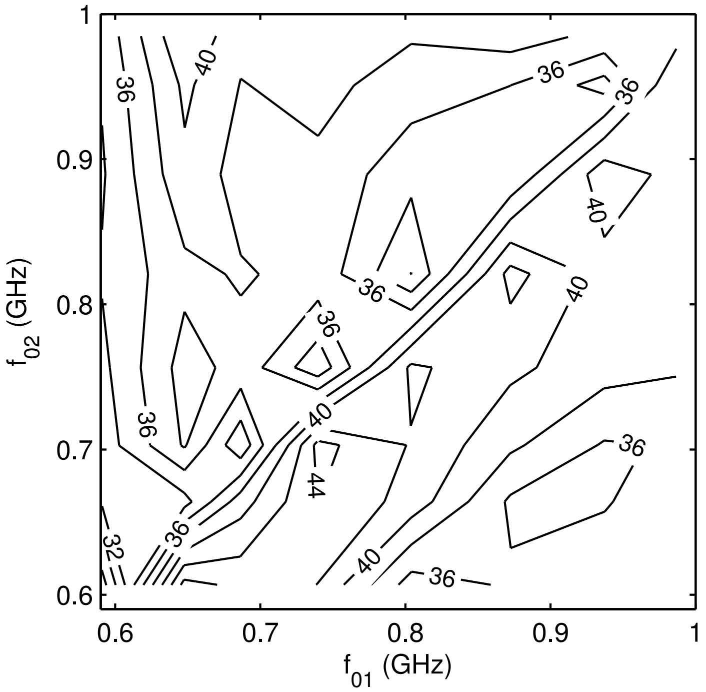

Figure 5.28: Minimum in-band differential-to-differential isolation in decibels between ports 1 and 2 of the 10-cm antenna.

from the same port are very similar; S_{11cd} and S_{21cd} have maxima in nearly the same location, and likewise, S_{22cd} and S_{12cd} have co-located maxima. This occurs because the common modes are coupled. If port 1 couples to the common mode due to some varactor mismatch, a common mode voltage appears at port 2, but no differential mode. The common-mode is affected by all capacitors for the same reason that it couples to both ports; it is non-zero along both the x and y axes.

Radiation Pattern

The 4-port S-parameters of the 10-cm cavity-backed patch antenna were measured in order to characterize both the differential and common modes. For the radiation pattern, however, differential signals were created using a 180° hybrid coupler and applied to Port 1 (Fig. 5.31). The hybrid coupler that was used cannot support a DC voltage (it is DC-short-circuited to ground), and therefore, bias tees were placed

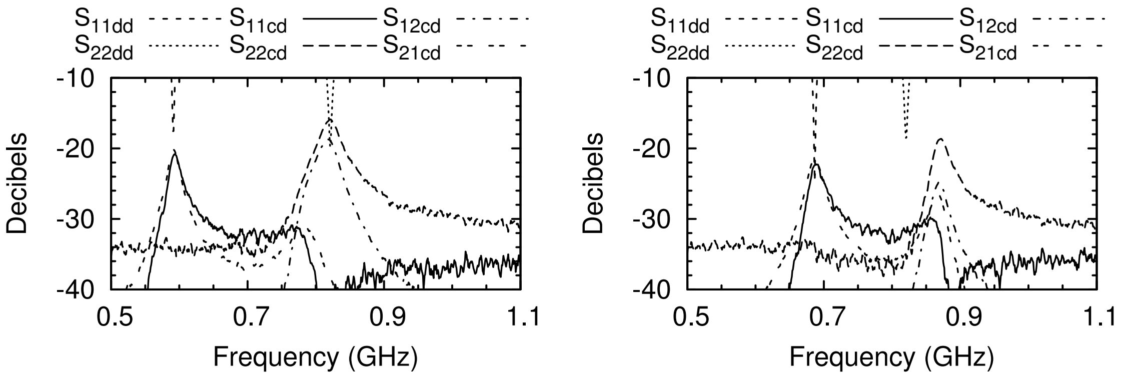

(a) $V_{b1} = 0$ V, $V_{b2} = 4$ V (b) $V_{b1} = 1$ V, $V_{b2} = 4$ V

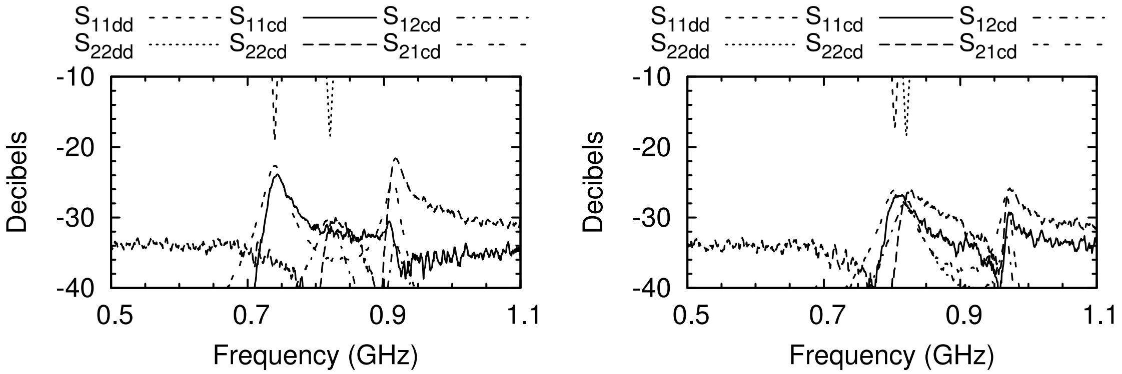

(c) $V_{b1} = 2$ V, $V_{b2} = 4$ V (d) $V_{b1} = 4$ V, $V_{b2} = 4$ V

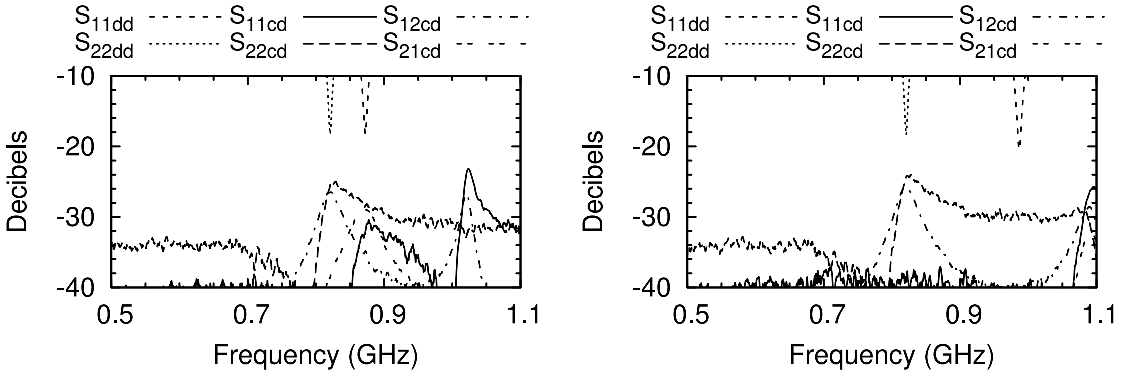

(e) $V_{b1} = 8$ V, $V_{b2} = 4$ V (f) $V_{b1} = 30$ V, $V_{b2} = 4$ V

Figure 5.29: Differential-to-common mode S-parameters of the 10-cm antenna when $V_{b2} = 4$ V.

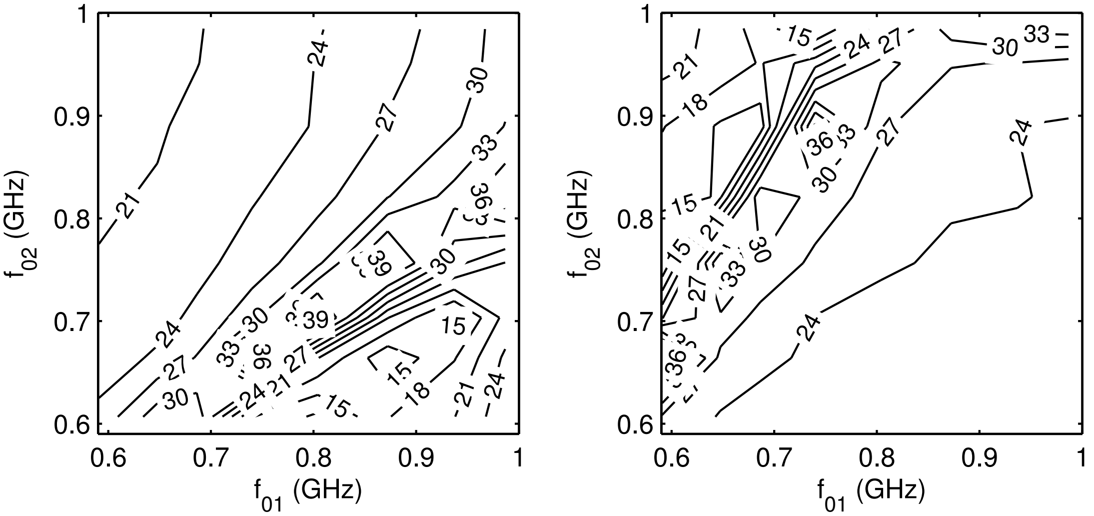

(a) S_{11cd}

(b) S_{22cd}

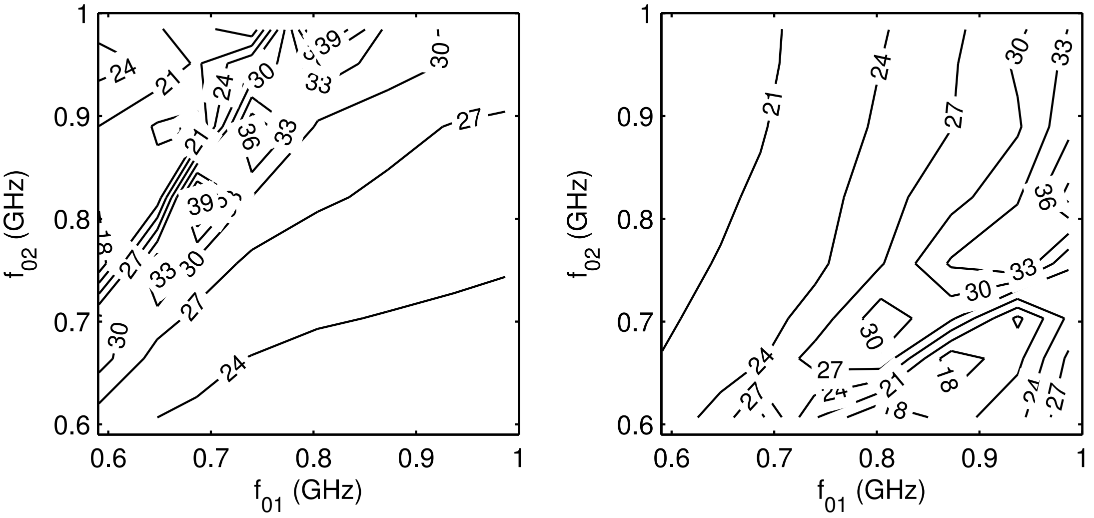

(c) S_{12cd}

(d) S_{21cd}

Figure 5.30: Minimum in-band differential-to-common mode isolation of the 10-cm antenna.

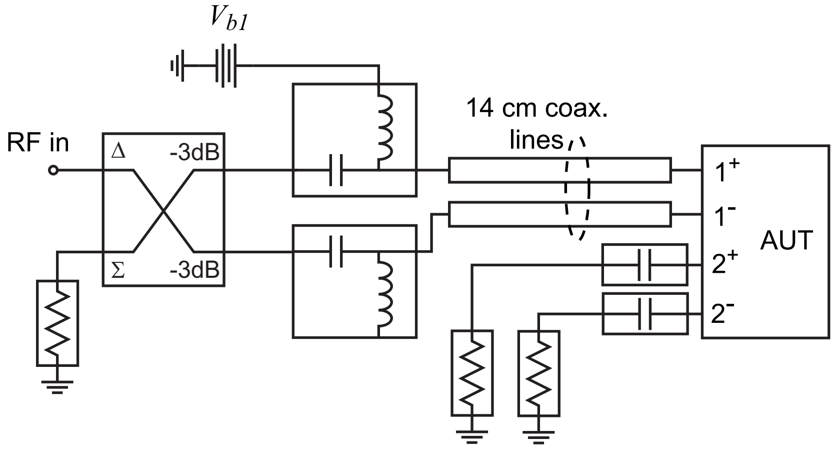

Figure 5.31: Schematic of the configuration used to measure the radiation pattern when the 10-cm antenna is fed with differential signals at Port 1.

between the coupler and the antenna. Although only one bias tee is necessary to place V_{b1} on the antenna, the second is added for phase balance. The bias tees and hybrid coupler were separated from the antenna by 14 cm with identical SMA cables. The combined amplitude and phase balance of the coupler, bias tees, and cables are within 0.1 dB and 0.5°, respectively, and the insertion loss (which was accounted for in the measured gain) varies from 1.1 dB at 0.6 Ghz to 1.4 dB at 1 GHz. V_{b2} was set to be equal to V_{b1} by soldering a wire across one of the biasing gaps at the center of the antenna, and terminated DC blocks were placed on ports 2^+ and 2^-.

The radiation patterns were measured with a Satimo Stargate32 spherical near-field system [27] for f_{01} = 650, 800, and 950 MHz ($V_{b1} = V_{b2} = 0.5$, 3.8, and 18.5). The Stargate32 measurement system measures the near fields on a spherical surface by rotating the antenna in azimuth as a circular array of field probes—centered about the antenna—measures the near fields in elevation. The spherical far field pattern is calculated by transforming the near fields to the far field. The antenna was placed on a piece of expanded polystyrene foam facing in the $\hat{z}$ direction, with the feed lines coming from the $-\hat{z}$ direction. The balun and bias tees were 14 cm below the antenna, and were surrounded by absorber in order to reduce scattering (Fig. 5.32).

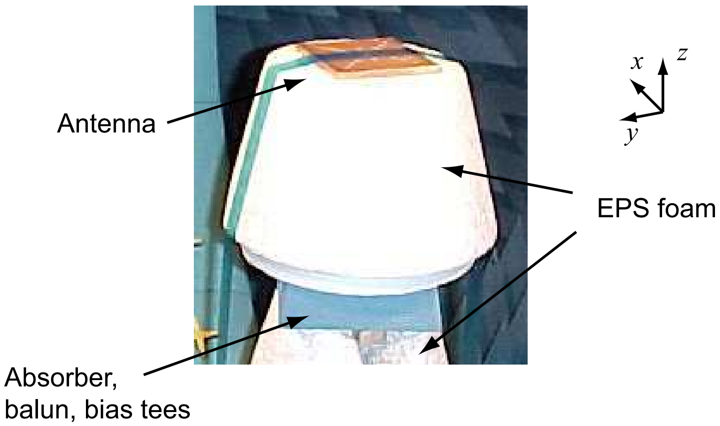

Figure 5.32: Antenna configuration during pattern measurement.

The antenna was fed by an absorber-coated coaxial cable, and the DC voltage was applied to one of the bias tees with another coaxial cable (without an absorptive coating).

The measured and simulated radiation patterns are compared in Fig. 5.33, and agree quite well—with the exception of the E-plane pattern in the lower half-space at 950 MHz (Fig. 5.33(c)). The measured patterns are slightly more directive than the simulated patterns, although the gain agrees quite well. Therefore, the measured efficiency is slightly lower than simulated (Fig. 5.34). The gain and efficiency vary from -2.2 dB to 4.5 dB and 21 to 72%, respectively, from 650 to 950 MHz. The difference between the measured and simulated patterns is likely due to scattering from and absorbtion by the absorber around the hybrid coupler and bias tees.

When operated with no ground plane extending beyond the antenna (as in Fig. 5.32), the antenna radiates a significant amount of power to the back side; the front to back ratio at 650 MHz is <1.5 dB. This is because the radiating slots are only 2 mm away from the edge of the antenna, and fringing fields and currents can easily radiate to the backside. If the antenna is placed in a large ground plane, it is expected that there will be little radiation to the back side. Therefore, the gain will be higher, but there will be ripple in the radiation pattern caused diffraction at the ground-plane edges [12].

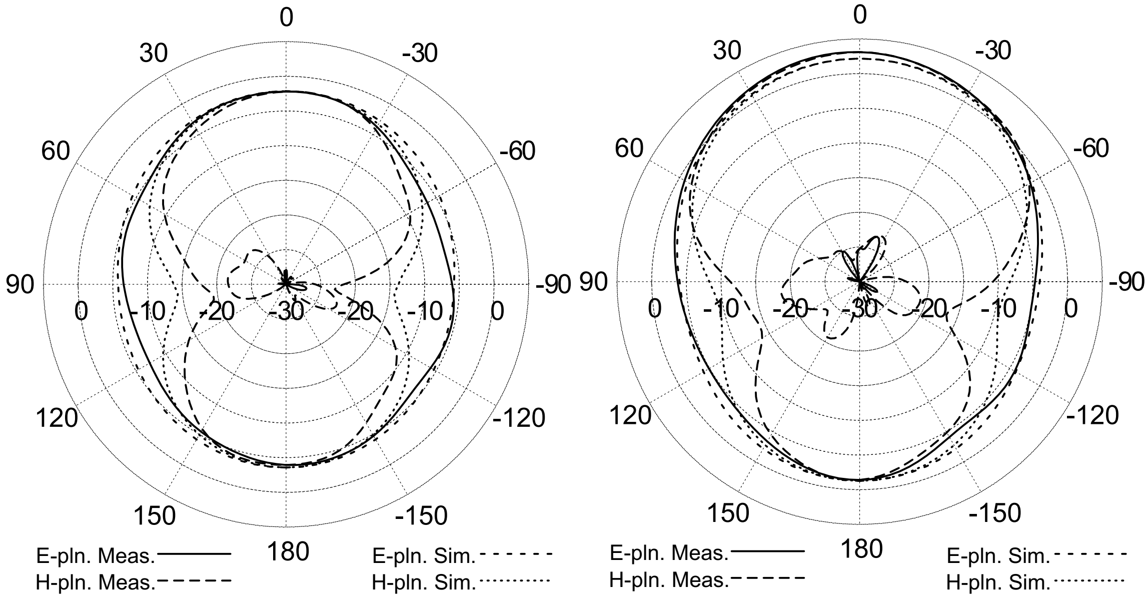

(a) 650 MHz, $V_{b1} = V_{b2} = 0.5$V (b) 800 MHz, $V_{b1} = V_{b2} = 3.8$V

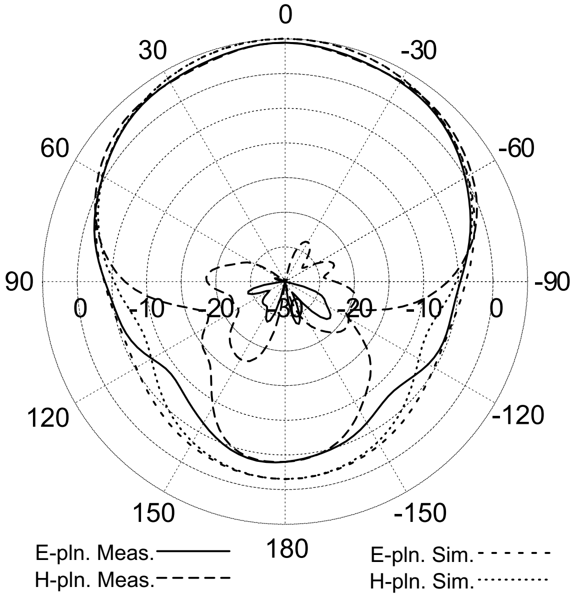

(c) 950 MHz, $V_{b1} = V_{b2} = 18.5$V

Figure 5.33: Measured and simulated co- and cross-polarized antenna gain patterns in dBi at f_{01} . The antenna is fed at Port 1 with a 180° hybrid coupler and Ports 2^+ and 2^- are terminated with 50 Ω.

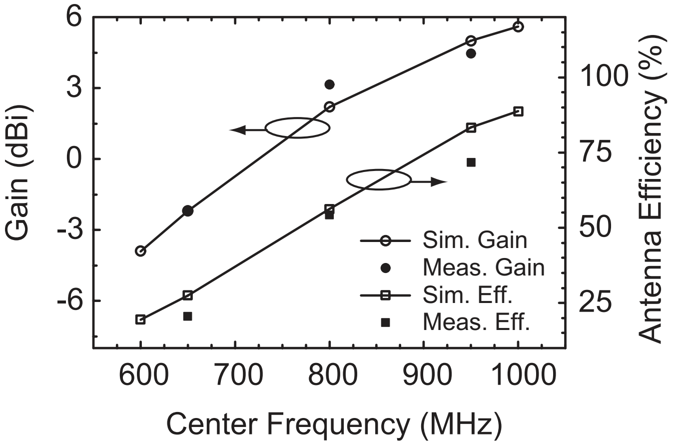

Figure 5.34: Measured and simulated antenna gain and efficiency of the 10-cm cavity-backed patch antenna.

Chapter 6

Conclusion

6.1 Summary of Work

The tunable antennas presented in this work find applications in frequency reconfigurable systems with small instantaneous bandwidths where small light-weight efficient antennas are required. Tunability of single- and dual-polarized antennas has been demonstrated over more than one octave using variable capacitors, and tuning ranges of 1.7:1 to 1.9:1 have been realized using standard varactor diodes.

The orthogonal polarizations of the dual-polarized antennas are independently-tunable over a 1.7:1 frequency range while remaining impedance matched and isolated from each other; they can either be tuned together, operating as a frequency and polarization agile antenna, or to different frequencies, operating as a dual-band antenna where the two frequencies couple to different ports. To the author's knowledge, this is the first demonstration of this type of independent tuning over a 1.7:1 frequency range.

6.1.1 Single-Polarized Antennas

Tuning of the slot-ring antenna from 1.93 to 5 GHz has been demonstrated using chip capacitors from 0–1 pF. True tuning from 0.95–1.8 GHz has been demonstrated using varactor diodes (0.45–2.5 pF) and a simple biasing scheme that consists of only a resistor and a via hole. At every tuning state, antenna is matched to the characteristic impedance at a frequency below its natural resonance frequency, and the reactance at that frequency is canceled by the microstrip stub. This can also be accomplished by placing a chip capacitor in series with the feedline and directly connecting the feedline to the opposite side of the slot with a via hole. Both the finite Q of the varactors and the size of the finite substrate affect the impedance matching characteristics, but these effects oppose each other, allowing for a reasonable impedance match over the tuning range.

The measured radiation patterns and efficiencies of the slot-ring antenna were significantly affected by the measurement cable because it was placed in the E-plane and the substrate is small ($< \lambda/2$). In future designs, the feed point should either be placed in the H-plane, or the substrate should be much larger.

Single-sided radiation is desirable for many applications, and the tunable shallow cavity-backed slot antenna was developed for this reason. It is 3.175 mm deep and tunes from just above 1 GHz to 1.9 GHz with better than -20 dB return loss. The impedance characteristics depend on the location of both the varactor and the feed, and therefore, a computer program was written that successfully found a combination of feed and loading points where the antenna could be matched to 50 Ω over a 1.9:1 tuning range. The antenna has nearly the same input impedance both in a free-standing configuration and conformally mounted in a 1.2×1.2 m^2 ground plane, and therefore, does not seem to be very sensitive to its environment.

6.1.2 Dual-Polarized Antennas

The first demonstration of dual-polarized independent tuning in this work is a slot-ring whose resonance frequencies were changed from 0.92–4.4 GHz. Symmetry is essential to maintaining good port-to-port isolation, and microstrip reactive loads were introduced to successfully balance the asymmetry introduced by the microstrip feeds. A varactor-diode-tuned antenna was then demonstrated that tunes from 0.93–1.6 GHz with port-to-port isolation better than 20 dB over most of the tuning range, and better than 14 dB over the whole range.

The second demonstration of dual-polarized independent tuning in this work is a differentially-fed cavity-backed patch antenna. The differential feeds ensure a port-to-port isolation of >30 dB over the 0.6–1 GHz tuning range. Furthermore, the measured cross-polarization levels at 650, 800, and 950 MHz are all < -25 dB at broadside. Impedance matching is performed by a combination of offsetting the probe feeds and adding series inductance, and all varactor diodes can be biased independently to compensate for mismatch in their tuning characteristics. The differential feed can be advantageous in systems where integrated circuits are placed near the antenna, however, phase-matching may be a problem as the antenna is scaled to higher frequencies.

6.2 General Conclusions about Varactor Tuned Antennas

The antennas presented in this work are highly tunable; the varactor capacitance ratio is the limiting factor in the tuning range. They all suffer the same reduction in efficiency and bandwidth, however, as they are tuned to the lower end of their respective tuning ranges. This is consistent with the literature, and may limit the useful tuning ranges of these antennas. The main contribution to the loss is the resistance of the varactor diodes. This efficiency can be improved if tuning elements with higher Q are used—the chip-capacitor-loaded slot-ring antenna has an efficiency of -2.4 dB when tuned to 40% of its unloaded resonance frequency—but this is expected to reduce the bandwidth further at the low end of the tuning range. Although these antennas are not considered “electrically small,”their radiation Q still rises sharply as they are loaded with capacitance because their susceptance slope increases. Larger bandwidth and higher efficiency will occur if the susceptance slope of the antenna can be reduced without simultaneously reducing the radiation conductance.

The impedance match over the tuning range has been studied, and it was found that a single non-tunable reactive element in series with the tunable antenna is capable of matching several different capacitively tuned antennas over one octave or more. This element behaves like an admittance inverter and matches the antenna slightly above or below its tuned resonance frequency. Whether this element is capacitive (e.g. a lumped element capacitor or an open-circuited stub feed to a slot antenna), inductive (e.g. a lumped element inductor or long probe feed to a patch), or not needed at all depends on the varactor efficiency and the location of the feed with respect to the voltage maximum.

6.3 Future Work

Perhaps the most relevant area of future research is conformally mounted tunable antennas. Single-sided radiation is often preferred, and therefore, it will be useful to develop the tunable cavity-backed slot antenna further. Limited investigation into the performance of varactor-tuned miniaturized CBS has been performed, and the results have not yet been experimentally verified. Furthermore, if a wide-band low-loss high impedance material becomes known, it should be used in the miniaturized tunable CBS antenna.

Many author have written about how to calculate the admittance and bandwidth of the cavity-backed slot antenna, but there is a need to extend the theory to tunable cavity-backed slot antennas. Most interesting would be to investigate the relationship between the radiation conductance and the susceptances due to the slot, tuning varactor, and the cavity in order to give design equations for the total Q (and therefore, bandwidth). The first step in this process will involve solving for the coupling to each mode in a closed form. If this cannot be done, then numerical calculations can be performed to produce design equations. Configurations with more than one varactor diode should also be investigated, as well as cavities which are not shallow.

The low directivity of slot apertures is advantageous for planar arrays. Varactor diode loading has been shown to eliminate scan blindness in infinite microstrip patch arrays [75], and a study of this phenomenon in cavity-backed slot arrays would be interesting. The performance of tunable phased arrays of cavity-backed slots can be investigated. In light of this, the tuning performance when the cavity is fed away from the slot can also be investigated.

Another extension to this work is to place the tunable slot-ring antenna on both a cavity [76], and above a high-impedance surface [33]. These will be slightly different problems to solve than the cavity-backed linear slot because the feed and varactor positions cannot be placed arbitrarily along the ring, but there may be enough freedom in the design of the backing and the matching network to achieve a good tuning range. These results should then be compared with the dual-polarized tunable cavity-backed patch antenna. Furthermore, a dual-polarized microstrip patch antenna can be demonstrated, although it is expected to have nearly identical results to the ones presented here.

The slot-ring can also be made to radiate to a single side by placing it on a hemispherical lens. Whereas this lens is very large for 1–2 GHz, it is much smaller for 10–20 GHz. Varactor diodes with practical values for the slot-ring antenna at these frequencies in air are not readily available. However, placing the slot on a dielectric reduces its characteristic impedance, and therefore increases the capacitance needed to tune the antenna.

Finally, tuning elements such as MEMS varactors should improve both the efficiency and the power handling of the antennas presented in this work, especially at the low frequencies. The antennas should be tested using MEMS tuning elements to see what kind of performance is possible.

Appendices

Appendix A

A Wide-Scan Millimeter-Wave Printed Planar Lens

A.1 Introduction and Background

Beam-scanning is an essential function in most radar systems, where a highly directive antenna scans a scene to record an image. Electronic scanning—as opposed to mechanical scanning, where the antenna physically moves—is attractive due to its speed and lack of moving parts. The ideal electronically-scanning antenna is the phased array, but its complexity and cost limit its use in commercial applications. A switched-beam system is a low-cost alternative in which the antenna switches between a finite number of beams in fixed directions. The Butler Matrix [77] and Rotman Lens [78, 79] are two switched beam systems in which the beam-forming is achieved in the substrate. Another approach is to use a lens or a reflectarray.

Lenses are an attractive option for switched beam antenna systems because the beam-forming is performed in free-space, and is mostly geometrical. Therefore, if the directivity of the antenna is increased by scaling the aperture size, the efficiency is not greatly affected. Printed planar-lenses are of particular interest due to their light weight, low volume, and ease of fabrication.

Planar lenses are made by coupling antenna array elements on one side of the lens to array elements on the other side of the lens with the appropriate phase response, synthesizing the phase response of a dielectric lens (Fig. A.1). Several groups have

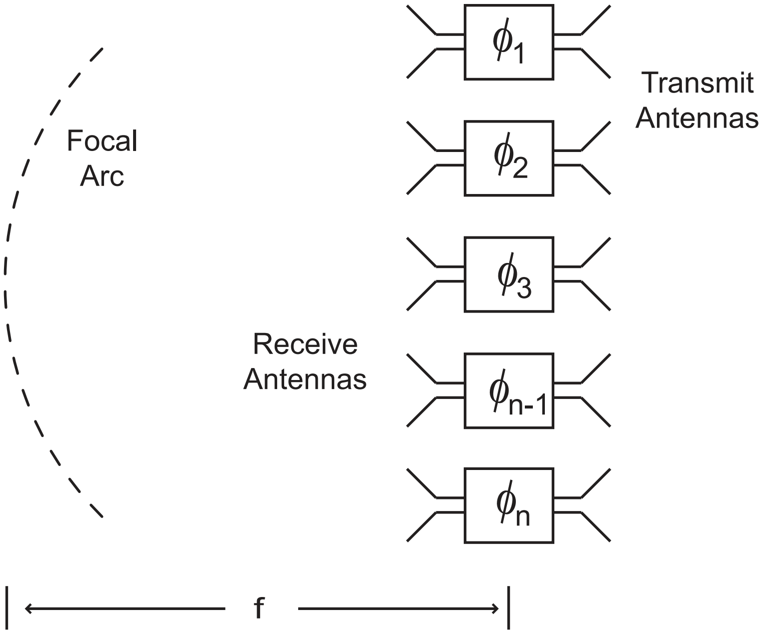

Figure A.1: Planar lens array. Focusing is achieved by synthesizing the phase response through the array.

developed such lenses using two different methods. The first method is to connect the antennas on the transmit and receive side with delay lines to obtain the appropriate phase response [80–82]. The second, the Antenna-Filter-Antenna (AFA) method, is to resonantly couple the antennas on the transmit and receive side forming a bandpass filter response and to scale the unit cells to obtain the desired phase response [83].

It is often desired to have a wide scan angle in a switched-beam system. Schoenlinner et al. demonstrated 180° scanning with a spherical dielectric lens [84], and reflectarrays have been shown to scan to 25° at 28 GHz [85] and 30° at 76 GHz [86]. However, a literature review shows little work in the area of wide-scan planar lenses. Popovic demonstrated an X-band lens which scans to ±45° in one plane using delay lines and via-holes [81]. In this work, a K-band lens is presented with at least ±56° scanning in both the E-plane and the H-plane and no grating lobes using the AFA concept (previously presented in [87]). The application of this unit-cell is limited because the phase range of the unit-cells is only about 200°. A 5-pole unit cell is proposed that may enable arbitrary lenses to be made with this method.

A.2 The 3-Pole–Unit-Cell Lens

A.2.1 Lens Design

A planar lens synthesizes the phase response of a dielectric lens—which change the wave fronts of waves that pass through—by coupling antennas on one side to antennas on the other side as shown in Fig. A.1. In a switched-beam system, the lens should focus plane waves from different angles at different points so that they can be received by different feed antennas. It is therefore desirable to design a lens with multiple focal-points. Constrained lenses with multiple focal-points are discussed in [80]; two focal points can be synthesized if the lens is planar and there is freedom to have the front-side and back-side antennas at different locations. In this work, however, the element spacing is too small to allow this degree of freedom. Therefore, the front- and back-side antennas are at the same location and only one focal point can be synthesized.

The element phases, ϕ_n, are chosen as follows. Referring to Fig. A.2, if a plane-wave illuminates the right side of lens, perfect focus (if it exists) occurs at the point where the radiation from the left side of the lens adds in phase. The focal point for this lens is on the optical axis, and therefore, the phases are the difference in electrical length from the focal point to the surface, and are normalized to the electrical length at the center:

$$\phi_n = k_0(r - f). \tag{A.1}$$

A geometry similar to [83] was used as the unit cell of the lens (Fig. A.3). Each cell consists of two microstrip patch antennas: one on the receive side and one on the transmit side. The two antennas are coupled with a quarter-wave CPW resonator

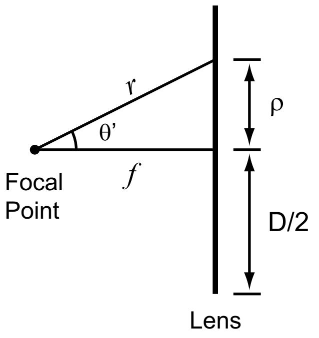

Figure A.2: Side view of a planar lens with a single focal point along the optical axis.

Table A.1: Nominal dimensions of the unit cell in millimeters. W_p and L_{cpw} are scaled to change the resonance frequency.

	size (mm)	scaled
d	5.5	no
W_p	3.7	yes
L_{cpw}	1.9	yes
CPW center cond.	0.23	no
CPW gap	0.2	no
h	0.5	no

forming a 3-pole bandpass filter. An equivalent circuit model is shown in Fig. A.3(c) where $\mathrm{L_a}$, $\mathrm{C_a}$, and the real part of $\mathrm{Z_L}$ are due to the patch antennas. The CPW resonator is modeled by $\mathrm{L_s}$ and $\mathrm{C_s}$. The imaginary part of $\mathrm{Z_L}$ is due to mutual coupling between unit cells.

It was shown in [88] that in order for $\mathrm{Z_L}$ to be real, the unit cell size should be the same as the effective area of the antennas. For a microstrip patch antenna, this spacing led to scan blindness at angles within the desired scan range. Since scan blindness can be avoided by placing the elements close together [58], a spacing of $0.44\lambda_0$ was chosen, where λ_0 is the free-space wavelength. The microstrip antenna dimensions and transformer ratio were tuned in order to absorb the imaginary part of $\mathrm{Z_L}$, and the dimensions are summarized in Table A.1.

The unit cell was simulated with the Finite Element Method [89] assuming an infinite periodic structure, and the frequency response is shown in Fig. A.4(a). Although

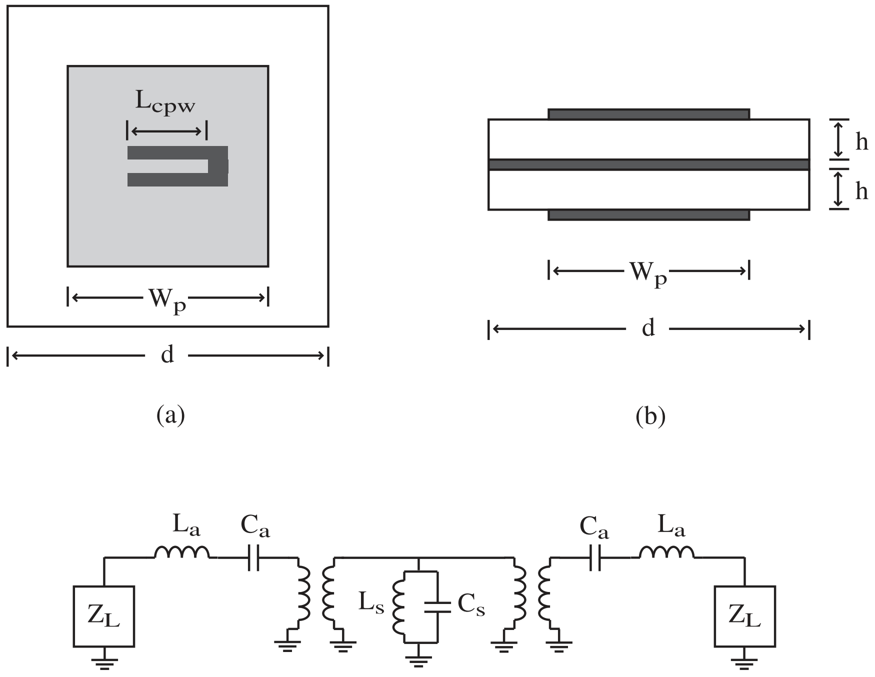

(a)

(b)

(c)

Figure A.3: Top (a) and side (b) views of the lens element. (c) Lumped model of the unit cell.

the lens is not an infinite periodic structure, this approach is justified by the size of the array as well as the fact that a unit cell's nearest neighbors vary only slightly from the unit cell. The pass-band of the unit-cell is from 22.6 to 25 GHz, and in this range, the phase changes over a range of about 180°. The required phase response of each unit cell was achieved by scaling the patch size and the length of the CPW resonator as in [83]. As the *center frequency* of the unit cell is shifted over a finite range, the phase of S_{21} *at 24 GHz* changes while the amplitude remains constant (Fig. A.4(b)). This method was able to provide 208° of phase shift allowing a maximum of 1 dB loss due to scaling. Due to the limited available phase values, the phase response at the center and edge of the lens was truncated, causing some phase errors.

Fig. A.5 shows the layout of the lens. It has a diameter D of 68.6 mm and a focal length f of 44.6 mm, and therefore $f/D = 0.65$. The center frequency is 24 GHz, and the elements are inscribed in a circle of diameter D on a square grid with period d, where d is $0.44\lambda_0$, or 5.5 mm.

Estimated antenna gain patterns of the lens were calculated in the transmit mode as follows. The measured E- and H-plane patterns of a 10-dB horn antenna were used to calculate the power and phase of the signal received by each unit cell. The power was then converted into a voltage, and the phase and amplitude were adjusted according to the simulated S_{21} of the unit cells. The antenna pattern was calculated as the array factor multiplied by the element factor. Finally, the radiated power was calculated by integration over the sphere and the gain was calculated. The calculations predict more than 10 dB less gain at 60° than at broadside (Fig. A.6). Spillover, which is significant because the edge-illumination level is -5 dB, was neglected.

The lens was fabricated by patterning the copper cladding on two 20-mil Taconic TLY5 substrates ($\epsilon_\mathrm{r} = 2.2$), and then bonding them together (Fig. A.7). The copper thickness is 17 μm.

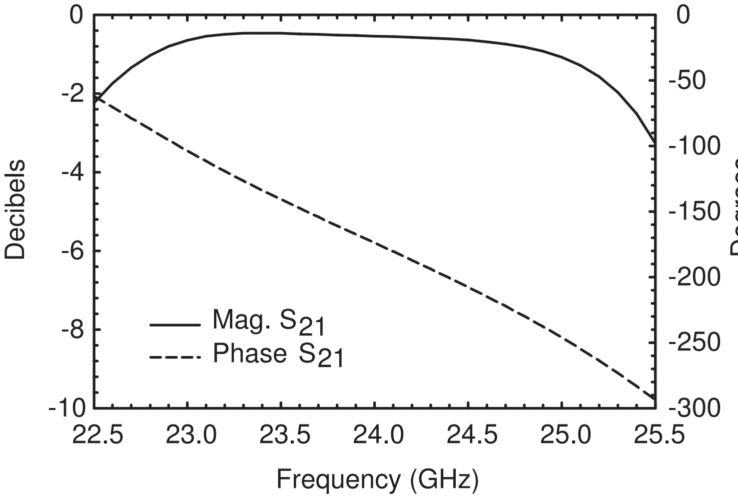

(a) Frequency response

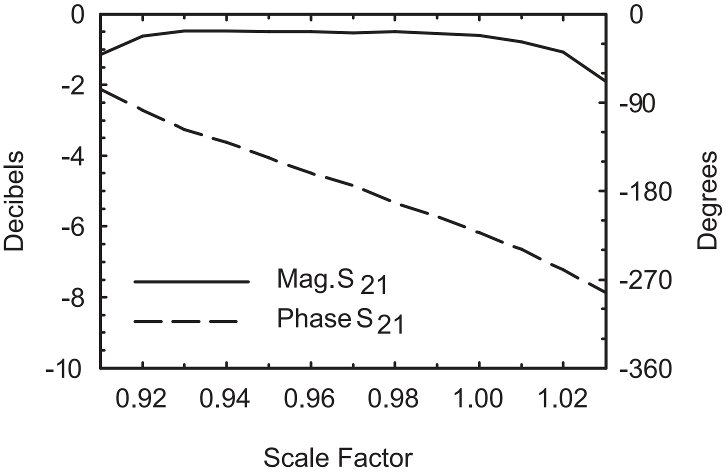

(b) Scale factor response

Figure A.4: Simulated magnitude and phase of S_{21} of the unit cell assuming an infinite array at normal incidence.

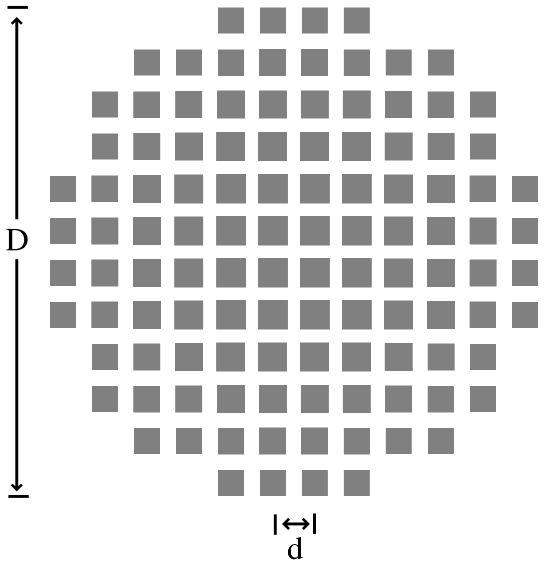

Figure A.5: Top view of the 24 GHz microstrip lens with 112 elements.

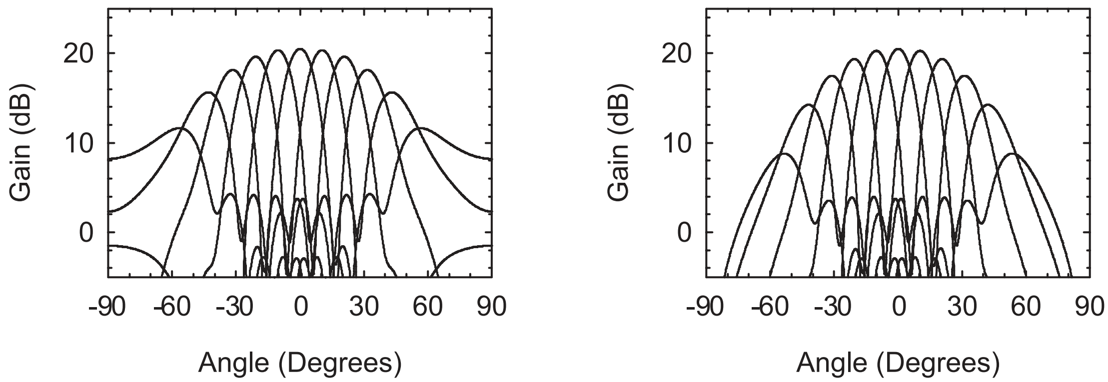

(a) E-plane

(b) H-plane

Figure A.6: Calculated antenna gain patterns in dBi of the lens fed by a 10-dB gain horn antenna along the focal arc.

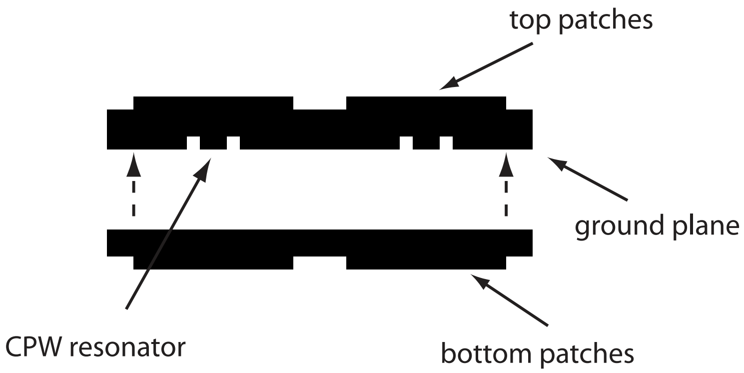

Figure A.7: Construction of the lens using two copper-clad substrates.

A.2.2 Results and Discussion

The lens was tested in an anechoic chamber at the University of Michigan. It was held by a mount which allowed the lens to be rotated about its center, as shown in Fig. A.8. The feed antenna was a 10 dB standard gain horn, and was placed at the focal distance. Rotating the lens, while keeping the feed-horn fixed, is equivalent to moving the feed-horn along the focal arc. The lens was placed in a cutout in a sheet of absorber to ensure that spillover did not interfere with the measurements. Fig. A.9 shows the measured radiation patterns for scan angles to ±60°. The lens scans to ±56° in both the E- and H-planes with less than 6 dB degradation in the gain. The side-lobe levels in the E- and H-planes are -13 dB and -14 dB, respectively, and are -7 dB at -60° in both planes (Fig. A.10). The predicted side-lobe level at broadside is -22 dB due to the tapering effect of the space-feed. The increased side-lobe levels are most likely due to phase errors, perhaps caused by both the non-ideal phase center of the horn antenna and edge effects. Whereas the infinite periodic structure assumption is valid at the center of the array, it is not valid for the outermost row of elements. The measured 3-dB beamwidths at broadside are 14° and 12.5° in the E- and H-planes, respectively (Fig. A.11). This is within 1.5° of the calculated values of 12.5°. The higher beamwidth in the E-plane, and not the H-plane, may be caused by edge effects because the mutual coupling is stronger in the E-plane. Therefore,

Figure A.8: The lens was fed by a 10-dB gain horn antenna. Scanning was simulated by rotating the lens relative to the feed-horn.

it is likely that the truncation of the lens creates a poor impedance for these edge elements, and increases the amplitude taper.

It is interesting to note that as the angle increased, the beams became skewed toward broadside from the angle of the feed. This was effect expected due to the element patterns of the patch antennas, but was actually weaker than predicted, suggesting that the scanning performance benefits from the strong mutual coupling between unit cells.

The antenna gain of the lens-horn combination was measured using the 3-antenna method, and is shown in Fig. A.12. It is 20 dBi at 24 GHz, and the 1-dB bandwidth is about 1 GHz. The directivity of a uniformly-illuminated aperture of the same physical size of the lens is 24.4 dB, and Table A.2 shows the estimated loss budget for the lens antenna system. The main source of loss is spillover; beamwidth was a more important criterion in the design than gain. This loss can be reduced at the expense of taper loss. Other main contributions to the loss are ohmic loss and edge effects.

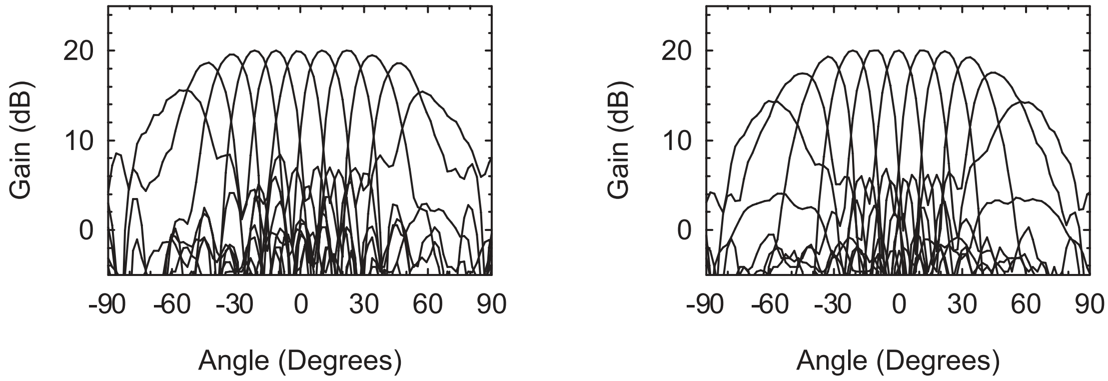

(a) E-plane

(b) H-plane

Figure A.9: Measured antenna gain patterns in dBi of the lens fed by a 10-dB gain horn antenna along the focal arc.

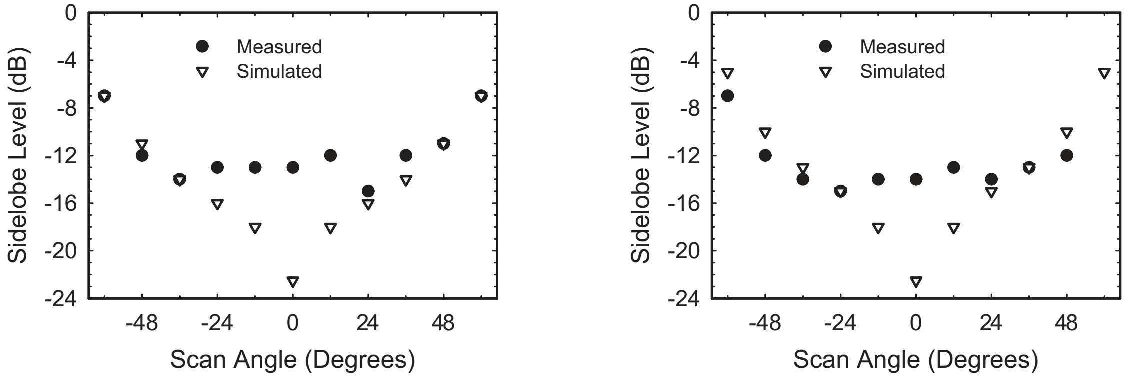

(a) E-plane

(b) H-plane

Figure A.10: Measured side-lobe levels in the principle planes.

Table A.2: Estimated Loss Budget (all values in dB)

Uniform Aperture Directivity	24.4
Spillover Loss	1.7
Taper Loss	0.5
Ohmic Loss	0.5
Phase Truncation Loss	0.3
Feed Reflection Loss	0.4
Edge Effects, other	0.9
Gain	20

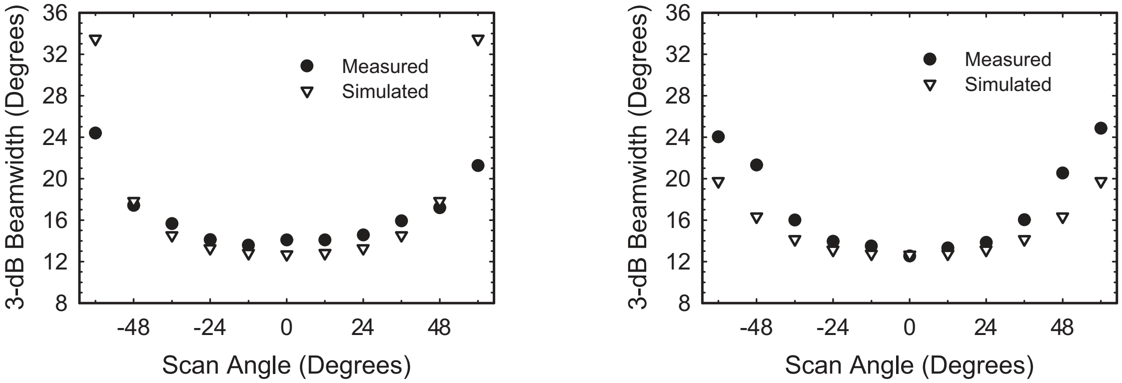

(a) E-plane

(b) H-plane

Figure A.11: Measured 3-dB beam-width of the lens fed by a 10-dB gain horn antenna along the focal arc.

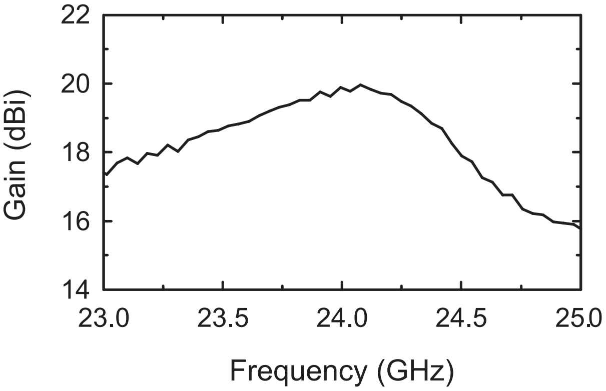

Figure A.12: Measured antenna gain of the lens fed by a 10-dB gain horn.

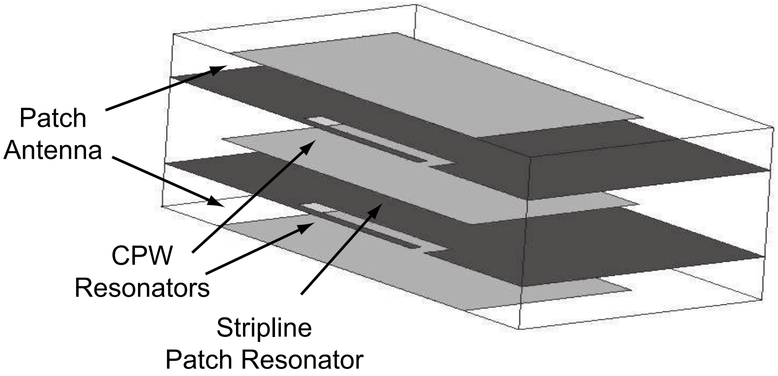

Figure A.13: Cross-sectional view of the 5-pole unit-cell.

A.3 Proposed 5-Pole Unit-Cell

The 3-pole unit-cell demonstrated in the previous section is a low-loss unit cell providing 208° range phase in which to design a lens. Therefore, its use is limited to lenses with limited phase requirements, i.e. small lenses, moderately sized lenses with large f/D, or large binary-phased lenses. As the number for poles in a filter response increases, the transmission phase in the pass-band increases. A 4-bit tunable AFA unit-cell has been demonstrated where the radiating elements are orthogonal slots coupled by striplines [90]. This unit cell rotates the polarization by 90°, however, which may or may not be desired.

A 5-pole unit-cell that does not change the polarization is made by adding an extra CPW and patch layer on top of the 3-pole unit-cell in Fig. A.3. The resulting in a 5-layer structure (Fig. A.13) can be fabricated by patterning the copper cladding on four substrates and bonding them together. The 5-pole unit cell was simulated in an infinite periodic structure at normal incidence with the finite element method [89] with the dimensions in Table A.1, and the results for the nominal unit-cell are shown in Fig. A.14. The phase varies by more than 400° between 22 and 25 GHz, and the magnitude is nearly constant in this range. It is quite convenient that the dimensions that are used in the 3-pole design can almost be directly applied to the 5-pole design.

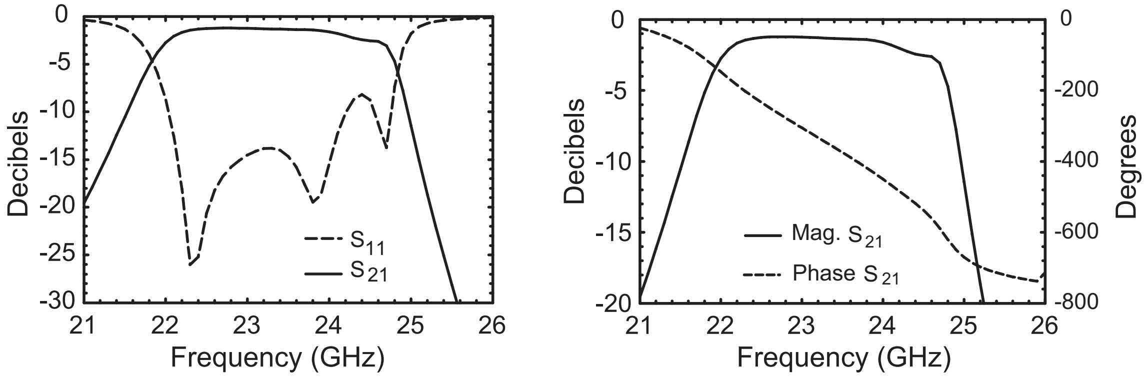

(a)

(b)

Figure A.14: Simulated frequency response of the nominal 5-pole unit-cell.

The proposed 5-pole unit-cell shows promise to enable arbitrary lens designs, but further analysis and measured data are necessary. Of particular concern is the existence of a dielectric-filled parallel-plate structure in the 5-pole unit-cell that did not exist in the 3-pole unit-cell design. One condition for scan blindness is [58]:

$$(\beta_{sw}/k_0)^2 = \left(\frac{m}{d/\lambda_0} + \sin\theta\right)^2, \tag{A.2}$$

where m is an integer, θ is the scan angle, and β_{sw} is the surface wave propagation constant. Equivalently:

$$\sin\theta = \frac{\pm d/\lambda_0\sqrt{\epsilon_{sw}} - m}{d/\lambda_0}, \tag{A.3}$$

where ϵ_{sw} is the effective dielectric constant of the surface-wave mode. For the microstrip case, $\epsilon_{sw} \approx 1$, and there is no scan blindness for a $0.44\lambda_0$ spacing. For the parallel-plate case, however, $\epsilon_{sw} = \epsilon_r$, and (A.3) is satisfied at $\theta = \pm 52^\circ$ when $\epsilon_r = 2.2$. Therefore, if there is any coupling, the performance will be degraded at nearby scan angles.

Finally, the beam-width must be considered in evaluating the scanning performance. It is well known that a lens with a single focus can be scanned a limited number of beamwidths before abberations (sidelobes) become an issue [91]. The wide-scan lens demonstrated here has 13° beams, and therefore, the importance of the scanning performance demonstrated in this work is due to the lack of scan-blindness. In a lens-antenna system with very narrow beams, the presence of abberations may limit the performance before scan-blindness becomes an issue.

Appendix B

Calculation of Circuit Parameters for the Microstrip Patch Transmission-Line Model

This appendix provides the equations necessary to use the accurate transmission line model for microstrip presented by Pues et al. [2].

The differentially-fed varactor-tuned microstrip patch antenna with width W and length $L = 2\ell_1 + 2\ell_2$ can be modelled as in Fig. 5.4(a), where $Y_s = G_s + jB_s$ is admittance of a single slot radiating slot and $Y_m = G_m + jB_m$ is the mutual coupling admittance between the two slots. The inductance due to the probe feed is [54]

$$L_{probe} = 60k_0h\left[\ln\left(\frac{2}{k_0p}\right) - C^e\right], \tag{B.1}$$

Where p is the radius of the probe and C^e is Euler's constant. The transmission-line characteristic admittance, Y_c, is given by [12]

$$Y_c = \frac{\sqrt{\epsilon_{eff}}\left[\frac{W}{h} + 1.393 + 0.677\ln\left(\frac{W}{h} + 1.444\right)\right]}{120\pi}, \tag{B.2}$$

where W is the width of the patch, h is the substrate thickness,

$$\epsilon_{eff} = \frac{\epsilon_r + 1}{2} + \frac{\epsilon_r - 1}{2}\left[1 + 12\frac{h}{W}\right]^{-1/2}, \tag{B.3}$$

is the effective dielectric constant, and ϵ_r is the dielectric constant of the substrate.

The slot susceptance is calculated as

$$B_s = Y_c \tan(\beta \Delta \ell), \tag{B.4}$$

where $\beta = k_0\sqrt{\epsilon_{eff}}$, k_0 is the free-space wave number, and the *effective* extension, $\Delta\ell$ of the transmission line due to fringing is calculated as in [92]. The slot conductance is for a finite length slot with uniform excitation is approximated as

$$G_s \approx \frac{1}{120\pi^2}\left\{\left(wSi(w) + \frac{\sin w}{w} + \cos w - 2\right)\left(1 - \frac{s^2}{24}\right) + \right. \\ \left. \frac{s^2}{12}\left(\frac{1}{3} + \frac{\cos w}{w} - \frac{\sin w}{w^3}\right)\right\}, \tag{B.5}$$

where $w = k_0 W$ and $s = k_0 \Delta\ell$ are the normalized slot dimensions, and Si is the Sine Integral.

The mutual admittance is calculated calculated as follows:

$$G_m = G_s F_g \tag{B.6a}$$

$$B_m = B_s F_b K_b, \tag{B.6b}$$

where

$$F_g = J_0(l) + \frac{s^2}{24 - s^2} J_2(l) \tag{B.7a}$$

$$F_b = \frac{\pi}{2} \frac{Y_0(l) + \frac{s^2}{24 - s^2} Y_2(l)}{\ln\left(\frac{s}{2}\right) + C^e - \frac{3}{2} + \frac{s^2/12}{24 - s^2}}, \tag{B.7b}$$

$l = k_0(L + \Delta\ell)$, J_n and Y_n are the nth order Bessel functions of the first and second kind, respectively, and

$$K_b = 1 - e^{-0.21w}. \tag{B.8}$$

Appendix C

Calculation of the Loaded S-parameters of a Multi-Port Antenna

Full-wave simulation of loaded antennas in this work involved placing ports at the locations of the loading elements, saving the N-port S-parameters, and then performing a circuit simulation by connecting the loading elements to the correct ports. This loading can be performed in nearly any circuit simulator, but it is not convenient in all cases. For example, if the antenna is to be loaded with the measured varactor impedance values, or if non-standard processing is to be performed on the data. In these cases, it was more convenient to load the full-wave simulated S-parameters manually in MATLAB [43]. The method is described here for loading ports 3 and 4 of a 4-port S-matrix—resulting in a 2-port S-matrix—but the method can be used for any number of ports.

The 4-port S-matrix relates all of the incoming and outgoing waves, a_n and b_n, respectively, at all four ports as shown in Fig. C.1. The system of equations is:

$$\begin{bmatrix} S_{11} & S_{12} & S_{13} & S_{14} \\ S_{21} & S_{22} & S_{23} & S_{24} \\ S_{31} & S_{32} & S_{33} & S_{34} \\ S_{41} & S_{42} & S_{43} & S_{44} \end{bmatrix} \begin{bmatrix} a_1 \\ a_2 \\ a_3 \\ a_4 \end{bmatrix} = \begin{bmatrix} b_1 \\ b_2 \\ b_3 \\ b_4 \end{bmatrix}. \tag{C.1}$$

When passive loads are placed on ports 3 and 4,

$$\frac{a_3}{b_3} = \Gamma_3 \quad \text{and} \quad \frac{a_4}{b_4} = \Gamma_4, \tag{C.2}$$

where

$$\Gamma_n = \frac{Z_n - Z_0}{Z_n + Z_0} \tag{C.3}$$

is the reflection coefficient at port n with respect to the characteristic impedance Z_0. A new matrix, M, now relates the the incoming and outgoing waves:

$$\begin{bmatrix} S_{11} & S_{12} & S_{13}\Gamma_3 & S_{14}\Gamma_4 \\ S_{21} & S_{22} & S_{23}\Gamma_3 & S_{24}\Gamma_4 \\ S_{31} & S_{32} & S_{33}\Gamma_3 - 1 & S_{34}\Gamma_4 \\ S_{41} & S_{42} & S_{43}\Gamma_3 & S_{44}\Gamma_4 - 1 \end{bmatrix} \begin{bmatrix} a_1 \\ a_2 \\ b_3 \\ b_4 \end{bmatrix} = \begin{bmatrix} b_1 \\ b_2 \\ 0 \\ 0 \end{bmatrix}, \tag{C.4}$$

and therefore,

$$M^{-1} \begin{bmatrix} b_1 \\ b_2 \\ 0 \\ 0 \end{bmatrix} = \begin{bmatrix} a_1 \\ a_2 \\ b_3 \\ b_4 \end{bmatrix}. \tag{C.5}$$

The upper left block of M^{-1} relates a_1 and a_2 to b_1 and b_2, and therefore, the loaded 2-port S-matrix is

$$S_2 = \begin{bmatrix} m'_{11} & m'_{12} \\ m'_{21} & m'_{22} \end{bmatrix}, \tag{C.6}$$

where m'_{ij} is the ijth element of M^{-1}.

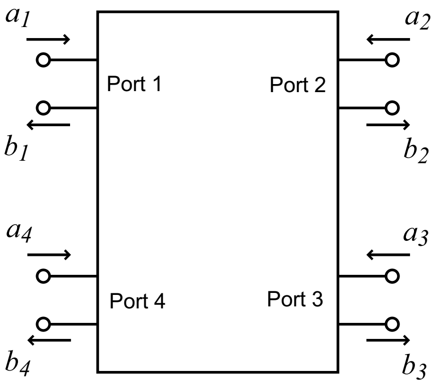

Figure C.1: A 4-port device with incoming waves, a_n, and outgoing waves, b_n.

Bibliography

[1] P. Bhartia and I. J. Bahl, "A frequency agile microstrip antenna," in *Proc. IEEE Ant. Prop. Symp.*, vol. 20, May 1982, pp. 304–307.

[2] H. Pues and A. Van de Capelle, "Accurate transmission-line model for the rectangular microstrip antenna," *IEE Proceedings*, vol. 131, no. 6, pp. 334–340, Dec. 1984.

[3] V. W. A. Mbarika and I. Mbarika, "Africa calling," *IEEE Spectr.*, vol. 53, no. 5, pp. 56–60, May 2006.

[4] B. Sklar, *Digital Communications: Fundamentals and Applications*, 2nd ed. New Jersey: Prentice Hall, 2001.

[5] R. C. Hansen, "Fundamental limitations in antennas," *Proc. IEEE*, vol. 69, no. 2, pp. 170–182, Feb. 1981.

[6] D. Peroulis, K. Sarabandi, and L. P. B. Katehi, "Design of reconfigurable slot antennas," *IEEE Trans. Antennas Propagat.*, vol. 53, no. 2, pp. 645–654, Feb. 2005.

[7] N. Behdad and K. Sarabandi, "A varactor-tuned dual-band slot antenna," *IEEE Trans. Antennas Propagat.*, vol. 54, no. 2, pp. 401–408, Feb. 2006.

[8] ——, "Dual-band reconfigurable antenna with a very wide tunability range," *IEEE Trans. Antennas Propagat.*, vol. 54, no. 2, pp. 409–416, Feb. 2006.

[9] S. H. Al-Charchafchi and M. Frances, "Electronically tunable microstrip patch antennas," in *Proc. IEEE Ant. Prop. Symp.*, vol. 1, June 1998, pp. 304–307.

[10] G. Le Ray, M. Himdi, and J. P. Daniel, "Frequency agild slot-fed patch antenna," *Electronics Letters*, vol. 32, no. 1, pp. 2–3, Jan. 1996.

[11] R. B. Waterhouse and N. V. Shuley, "Frequency agile microstrip rectangular patches using varactor diodes," in *Proc. IEEE Ant. Prop. Symp.*, vol. 4, July 1992, pp. 2188–2191.

[12] C. A. Balanis, *Antenna Theory: Analysis and Design*, 2nd ed. New York: Wiley, 1997, ch. 2.

[13] D. Gesbert, M. Shafi, D. shan Shui, P. J. Smith, and A. Naguib, "From theory to practice: An overview of MIMO space-time coded wireless systems," *IEEE J. Select. Areas Commun.*, vol. 21, no. 3, pp. 281–302, Apr. 2003.

[14] J. Mitola and G. Q. Maguire, "Cognitive radio: Making software radios more personal," *IEEE Personal Commun. Mag.*, vol. 6, no. 4, pp. 13–18, Aug. 1999.

[15] S. Raman and G. M. Rebeiz, "Single- and dual-polarized millimeter-wave slot-ring antennas," *IEEE Trans. Antennas Propagat.*, vol. 44, no. 11, pp. 1438–1444, Nov. 1996.

[16] P. S. Hall, "Review of techniques for dual and circularly polarised microstrip antennas," in *Microstrip Antennas*, D. M. Pozar and D. H. Schaubert, Eds. New York: IEEE Press, 1995, ch. 3, pp. 107–116.

[17] C. Hong, "Small annular slot antenna with capacitor loading," *Electronics Letters*, vol. 36, no. 2, pp. 110–111, Jan. 2000.

[18] I. Carrasquillo-Rivera *et al.*, "Tunable and dual-band rectangular slot-ring antenna," in *Proc. IEEE Ant. Prop. Symp.*, vol. 4, June 2004, pp. 4308–4311.

[19] E. Erdil *et al.*, "Reconfigurable cpw-fed dual-frequency rectangular slot antenna using RF MEMS technology," in *Proc. IEEE Ant. Prop. Symp.*, vol. 2A, July 2005, pp. 392–395.

[20] S. Nikolaou *et al.*, "Pattern and frequency reconfigurable annular slot antenna using PIN diodes," *IEEE Trans. Antennas Propagat.*, vol. 54, no. 2, pp. 439–448, Feb. 2006.

[21] C. R. White and G. M. Rebeiz, "A slot-ring antenna with an octave of tunability," in *Proc. IEEE Ant. Prop. Symp.*, June 2007, pp. 5841–5844.

[22] ——, "A dual-polarized slot-ring antenna with independent tuning," in *Proc. IEEE Ant. Prop. Symp.*, June 2007, pp. 113–116.

[23] R. Garg *et al.*, *Microstrip Antenna Design Handbook*. Boston: Artech House, 2001, ch. 7.

[24] *IE3D 11*, Zeland Software Inc., Fremont, CA, USA.

[25] *MA46H071-1056*, M/A-Com, Lowell, MA, USA.

[26] *Microwave Bluetooth^{TM} Ferrites*, Ferrishield, Inc., Tampa, FL, USA.

[27] Satimo, Courtaboeuf, France.

[28] D. Sievenpiper, H.-P. Hsu, and R. M. Riley, "Low-profile cavity-backed crossed-slot antenna with a single-probe feed designed for 2.34-ghz satellite radio applications," *IEEE Trans. Antennas Propagat.*, vol. 52, no. 3, pp. 873–879, Mar. 2004.

[29] A. Vallecchi and G. B. Gentili, "Microstrip-fed slot antennas backed by a very thin cavity," *Microwave and Optical Tech. Letters*, vol. 49, no. 1, pp. 247–250, Jan. 2007.

[30] A. C. Polycarpou *et al.*, "Radiation and scattering from ferrite-tunied cavity-backed slot antennas: Theory and experiment," *IEEE Trans. Antennas Propagat.*, vol. 49, no. 9, pp. 1297–1306, Sept. 1998.

[31] Y. Yoshimura, "Microstripline slot antenna," *IEEE Trans. Microwave Theory Tech.*, vol. 20, pp. 760–762, Nov. 1972.

[32] F. Yang, Y. Qian, and T. Itoh, “Low-provile cavity-backed slot antenna using UC-PBG substrate,” in *Proc. IEEE Ant. Prop. Symp.*, vol. 3, July 2000, pp. 1796–1799.

[33] D. Sievenpiper *et al.*, “High-impedance electromagnetic surfaces with a forbidden frequency band,” *IEEE Trans. Microwave Theory Tech.*, vol. 47, no. 11, pp. 2059–2074, Nov. 1999.

[34] J. L. Volakis, M. W. Nurnberger, and D. S. Filipovic, “Slot spiral antenna,” *IEEE Antennas Propagat. Mag.*, vol. 43, no. 6, pp. 15–26, Dec. 2001.

[35] M. Qiu, M. Simcoe, and G. V. Eleftheriades, “Radiation efficiency of printed slot antennas backed by a ground reflector,” in *Proc. IEEE Ant. Prop. Symp.*, vol. 3, July 2000, pp. 1612–1615.

[36] G. M. Rebeiz, “Millimeter-wave and terahertz integrated circuit antennas,” *Proc. IEEE*, vol. 80, no. 11, pp. 1748–1770, Nov. 1992.

[37] A. T. Adams, “Flush-mounted rectangular cavity slot antennas—theory and design,” *IEEE Trans. Antennas Propagat.*, vol. 15, no. 3, pp. 342–351, May 1967.

[38] T. Lertwtriyaprapa *et al.*, “Analysis of impedance characteristics of a probe fed rectangular cavity-backed slot antenna,” in *Proc. IEEE Ant. Prop. Symp.*, vol. 1, July 2001, pp. 576–579.

[39] C. R. Cockrell, “The input admittance of the rectangular cavity-backed slot antenna,” *IEEE Trans. Antennas Propagat.*, vol. 24, no. 3, pp. 288–294, May 1976.

[40] J. Galejs, “Admittance of a rectangular slot which is backed by a rectangular cavity,” *IEEE Trans. Antennas Propagat.*, vol. 11, no. 2, pp. 119–126, Mar. 1963.

[41] A. Hadidi and M. Hamid, “Aperture field and circuit parameters of cavity-backed slot radiator,” *IEE Proceedings*, vol. 136, no. 2, pp. 139–146, Apr. 1989.

[42] C.-H. Liang and D. K. Cheng, “Electromagnetic fields coupled into a cavity with a slot-aperture under resonant conditions,” *IEEE Trans. Antennas Propagat.*, vol. 30, no. 4, pp. 664–672, July 1982.

[43] *MATLAB 7.0*, The MathWorks, Inc., Natick, MA, USA.

[44] M. E. Goldfarb and R. A. Pucel, “Modeling via hole grounds in microstrip,” *IEEE Microwave Guided Wave Lett.*, vol. 1, no. 6, pp. 135–137, June 1991.

[45] Coilcraft, Inc., Cary, IL, USA.

[46] AVX Corporation, Myrtle Beach, SC, USA.

[47] B. Zheng and Z. Shen, "Effect of a finite ground plane on microstrip-fed cavity-backed slot antennas," *IEEE Trans. Antennas Propagat.*, vol. 53, no. 2, pp. 862–865, Feb. 2005.

[48] M. H. Cohen, "On the band width of cavity antennas," *Journal Appl. Phys.*, vol. 25, no. 5, pp. 582–587, May 1954.

[49] W. Hong, N. Behdad, and K. Sarabandi, "Size reduction of cavity-backed slot antennas," *IEEE Trans. Antennas Propagat.*, vol. 54, no. 5, pp. 1461–1466, May 2006.

[50] Rogers Corporation, Rogers, CT, USA.

[51] G. L. Matthaei, L. Young, and E. M. T. Jones, *Microwave Filters, Impedance-Matching Networks, and Coupling Structures.* Norwood, MA: Artech House, 1980, ch. 8.

[52] D. H. Schaubert, F. G. Farrar, A. Sindoris, and S. T. Hayes, "Microstrip antennas with frequency agility and polarization diversity," *IEEE Trans. Antennas Propagat.*, vol. 29, no. 1, pp. 118–123, Jan. 1981.

[53] N. Fayyaz, S. Safavi-Naeini, E. Shin, and N. Hodjat, "A novel electronically tunable rectangular patch antenna with one octave bandwidth," in *IEEE Canadian Conf. Elect. and Comp. Eng.*, vol. 1, May 1998, pp. 25–28.

[54] R. Garg *et al.*, *Microstrip Antenna Design Handbook.* Boston: Artech House, 2001.

[55] D. M. Pozar and D. H. Schaubert, Eds., *Microstrip Antennas.* New York: IEEE Press, 1995.

[56] K. R. Carver and J. W. Mink, "Microstrip antenna technology," *IEEE Trans. Antennas Propagat.*, vol. 29, no. 1, pp. 2–24, Jan. 1981.

[57] W. L. Stutzman and G. A. Thiele, *Antenna Theory and Design*, 2nd ed. New York: Wiley, 1998.

[58] D. M. Pozar and D. H. Schaubert, "Scan blindness in infinite phased arrays of printed dipoles," *IEEE Trans. Antennas Propagat.*, vol. AP-32, no. 6, pp. 602–610, June 1984.

[59] F. Zavosh and J. T. Aberle, "Improving the performance of microstrip-patch antennas," *IEEE Antennas Propagat. Mag.*, vol. 38, no. 4, pp. 7–12, Aug. 1996.

[60] G. G. Gentili, F. Perez-Martinez, M. Salazar-Palma, and L. Garcia-Castillo, "Analysis of single and stacked microstrip patch antennas residing in a cavity by a green's function technique," in *Proc. IEEE Ant. Prop. Symp.*, vol. 2, June 1994, pp. 944–947.

[61] J. L. Volakis and J.-M. Jin, “A scheme to lower the resonance frequency of the microstrip patch antenna,” *IEEE Microwave Guided Wave Lett.*, vol. 2, no. 7, pp. 292–293, July 1992.

[62] D. H. Schaubert, “A review of some microstrip antenna characteristics,” in *Microstrip Antennas*, D. M. Pozar and D. H. Schaubert, Eds. New York: IEEE Press, 1995, ch. 2, pp. 59–67.

[63] A.-F. Sheta and S. F. Mahmoud, “A widely tunable compact patch antenna,” *IEEE Antennas Wireless Propagat. Lett.*, vol. 7, pp. 40–42, 2008.

[64] F. Yang and Y. Rahmat-Samii, “Patch antennas with switchable slots (pass) in wireless communications: Concepts, designs, and applications,” *IEEE Antennas Propagat. Mag.*, vol. 47, no. 2, pp. 13–29, Apr. 2005.

[65] L. Le Garrec, R. Sauleau, and M. Himdi, “A 2:1 frequency-agile active microstrip patch antenna,” in *European Conf. on Anten. and Propagat., MONTH = nov, YEAR = 2007.*

[66] W. H. Weedon, W. J. Payne, and G. M. Rebeiz, “MEMS-switched reconfigurable antennas,” in *Proc. IEEE Ant. Prop. Symp.*, vol. 3, July 2001, pp. 654–657.

[67] J. T. Aberle, M. Chu, and C. R. Birtcher, “Scattering and radiation properties of varactor-tuned microstrip antennas,” in *Proc. IEEE Ant. Prop. Symp.*, vol. 4, June 1992, pp. 2229–2232.

[68] Z. Jin and A. Mortazawi, “An L-band tunable microstrip antenna using multiple varactors,” in *Proc. IEEE Ant. Prop. Symp.*, vol. 4, June 2003, pp. 524–527.

[69] T. Chiba, Y. Suzuki, and N. Miyano, “Supression of higher modes and cross polarized component for microstrip antennas,” in *Proc. IEEE Ant. Prop. Symp.*, vol. 20, May 1982, pp. 285–288.

[70] J. D. Hanfling, J. J. Schuss, and R. E. Morrow, “A dual polarized patch radiator for phased arrays,” in *Proc. IEEE Ant. Prop. Symp.*, vol. 3, June 1989, pp. 1216–1219.

[71] P. S. Hall, “Probe compensation in thick microstrip patches,” *Electronics Letters*, vol. 23, no. 11, pp. 606–607, May 1987.

[72] Skyworks Solutions Inc., Woburn, MA, USA.

[73] R. E. Munson, “Conformal microstrip antennas and microstrip phased arrays,” *IEEE Trans. Antennas Propagat.*, vol. 22, no. 1, pp. 74–78, Jan. 1974.

[74] A. G. Derneryd, “A theoretical investigation of the rectangular microstrip antenna element,” *IEEE Trans. Antennas Propagat.*, vol. 26, no. 4, pp. 532–535, July 1978.

[75] R. B. Waterhouse and N. V. Shuley, "Scan performance of infinite arrays of microstrip patch elements loaded with varactor diodes," *IEEE Trans. Antennas Propagat.*, vol. 41, no. 9, pp. 1273–1280, Sept. 1993.

[76] J. Galejs, "Admittance of a cavity-backed annular slot antenna," *IEEE Trans. Antennas Propagat.*, vol. 10, no. 6, pp. 671–678, Nov. 1962.

[77] J. P. Shelton, "Multibeam planar arrays," *Proc. IEEE*, vol. 56, no. 11, pp. 1818–1821, Nov. 1968.

[78] W. Rotman and R. Turner, "Wide-angle microwave lens for line source applications," *IEEE Trans. Antennas Propagat.*, vol. 11, no. 6, pp. 623–632, Nov. 1963.

[79] L. Schulwitz and A. Mortazawi, "A compact dual-polarized multibeam phased-array architecture for millimeter-wave radar," *IEEE Trans. Microwave Theory Tech.*, vol. 53, no. 11, pp. 3588–3594, Nov. 2005.

[80] D. T. McGrath, "Planar three-dimensional constrained lenses," *IEEE Trans. Antennas Propagat.*, vol. AP-34, no. 1, pp. 46–50, Jan. 1986.

[81] D. Popovic and Z. Popovic, "Multibeam antennas with polarization and angle diversity," *IEEE Trans. Antennas Propagat.*, vol. 50, no. 5, pp. 651–657, May 2002.

[82] D. M. Pozar, "Flat lens antenna concept using aperture coupled microstrip patches," *Electronics Letters*, vol. 32, pp. 2109–2111, Nov. 1996.

[83] A. Abbaspour-Tamijani, K. Sarabandi, and G. M. Rebeiz, "A planar filter-lens array for millimeter-wave applications," in *Proc. IEEE Ant. Prop. Symp.*, June 2004, pp. 675–678.

[84] B. Schoenlinner, X. Wu, J. P. Ebling, G. V. Eleftheriades, and G. M. Rebeiz, "Wide-scan spherical-lens antennas for automotive radars," *IEEE Trans. Microwave Theory Tech.*, vol. 50, no. 9, pp. 2166–2175, Sept. 2002.

[85] D. M. Pozar, S. D. Tardonski, and H. D. Syrigos, "Design of millimeter wave microstrip reflectarrays," *IEEE Trans. Antennas Propagat.*, vol. 45, no. 2, pp. 287–296, Feb. 1997.

[86] W. Menzel, M. Al-Tikriti, and R. Leberer, "A 76 ghz multiple-beam planar reflector antenna," in *Proc. of European Microwave Conference*, Sep. 2002, pp. 977–980.

[87] C. R. White, J. P. Ebling, and G. M. Rebeiz, "A wide-scan printed planar k-band microwave lens," in *Proc. IEEE Ant. Prop. Symp.*, July 2005, pp. 313–316.

[88] A. Abbaspour-Tamijani, K. Sarabandi, and G. M. Rebeiz, "Antennafilterantenna arrays as a class of bandpass frequency-selective surfaces," *IEEE Trans. Microwave Theory Tech.*, vol. 52, no. 8, pp. 1781–1789, Aug. 2004.

[89] *HFSS 9.2*, Ansoft Corporation, Pittsburg, PA, USA.

[90] C.-C. Cheng and A. Abbaspour-Tamijani, “Study of 2-bit antenna-filter-antenna elements for reconfigurable millimeter-wave lens arrays,” *IEEE Trans. Microwave Theory Tech.*, vol. 54, no. 12, pp. 4498–4506, Dec. 2006.

[91] J. J. Lee, “Lens antennas,” in *Antenna Handbook: Theory Applications and Design*, Y. T. Lo and S. W. Lee, Eds., ch. 16.

[92] M. Kirschning, R. H. Jansen, and N. H. L. Koster, “Accurate model for open end effect of microstrip lines,” *Electronics Letters*, vol. 17, no. 3, pp. 123–125, Feb. 1981.